

**SYNTHESIS AND CHARACTERIZATION OF  $MgFe_2O_4$  FERRITE  
NANOENSEMBLE FOR BIOMEDICAL APPLICATION**

**M. Phil. Thesis**

**BY**

**NIPA DEBNATH**



**DEPARTMENT OF PHYSICS  
KHULNA UNIVERSITY OF ENGINEERING & TECHNOLOGY  
KHULNA - 9203, BANGLADESH**

**SEPTEMBER - 2015**

**SYNTHESIS AND CHARACTERIZATION OF  $MgFe_2O_4$  FERRITE  
NANOENSEMBLE FOR BIOMEDICAL APPLICATION**

**BY**

**NIPA DEBNATH  
ROLL NO: 1155504  
SESSION: JANUARY - 2011**

A THESIS SUBMITTED TO THE DEPARTMENT OF PHYSICS,  
KHULNA UNIVERSITY OF ENGINEERING & TECHNOLOGY,  
KHULNA - 9203 IN PARTIAL FULFILMENT OF THE  
REQUIRMENT FOR THE DEGREE OF MASTER OF PHILOSOPHY



DEPARTMENT OF PHYSICS  
KHULNA UNIVERSITY OF ENGINEERING & TECHNOLOGY  
KHULNA - 9203, BANGLADESH

SEPTEMBER - 2015

**KHULNA UNIVERSITY OF ENGINEERING & TECHNOLOGY  
DEPARTMENT OF PHYSICS**

Approval

This is to certify that the thesis work submitted by Nipa Debnath entitled “*Synthesis and Characterization of  $MgFe_2O_4$  Ferrite Nanoensemble for Biomedical Application*” has been accepted by the Board of Examiners for the partial fulfillment of the requirements for the degree of Master of Philosophy in the Department of Physics, Khulna University of Engineering & Technology, Khulna, Bangladesh on 17 September, 2015.

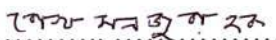
**Board of Examiners**

**Sl. No. Name, Designation & Address**

1. Prof. Dr. Shibendra Shekher Sikder  
Department of Physics  
Khulna University of Engineering & Technology  
Khulna-9203, Bangladesh

  
.....  
Chairman & Supervisor

2. Dr. Sheikh Manjura Hoque  
Head, Materials Science Division  
Atomic Energy Center  
Dhaka-1000, Bangladesh

  
.....  
Co- Supervisor


3. Prof. Dr. Jolly Sultana  
Head  
Department of Physics  
Khulna University of Engineering & Technology  
Khulna-9203, Bangladesh

  
.....  
Member

4. Prof. Dr. Md. Mahbub Alam  
Department of Physics  
Khulna University of Engineering & Technology  
Khulna-9203, Bangladesh

  
.....  
Member


5. Dr. A. K. M. Abdul Hakim  
Individual Consultant  
Department of Glass and Ceramic Engineering  
Bangladesh University of Engineering and Technology  
Dhaka-1000, Bangladesh

  
.....  
Member (External)

## DECLARATION

This is to certify that the thesis work entitled as “**Synthesis and Characterization of MgFe<sub>2</sub>O<sub>4</sub> Ferrite Nanoensemble for Biomedical Application**” has been carried out in partial fulfillment of the requirement for M. Phil degree in the department of Physics, Khulna University of Engineering & Technology, Khulna - 9203, Bangladesh. The above research work or any part of this work has not been submitted anywhere for the award of any degree or diploma. No other person’s work has been used without due acknowledgement.

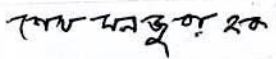
1. Supervisor

  
-----  
(Prof. Dr. S. S. Sikder)

Candidate

  
-----  
(Nipa Debnath)

2. Co-Supervisor

  
-----  
(Dr. Sheikh Manjura Hoque )



**TO**

**MY PARENTS AND MY HUSBAND**

## **Acknowledgements**

It gives me immense and satisfaction to acknowledge the blessings of the Lord Krishna creator of the universe who is the most gracious compassionate and beneficent to its creature, who beloved me with knowledge and potential to implement my research work.

I express with due respect my deep sense of gratitude and indebtedness to my Supervisor Professor Dr. Shibendra Shekher Sikder, Department of Physics, Khulna University of Engineering & Technology, Khulna for his indispensable guidance, keen interest, constructive and constant inspiration throughout suggestions close supervision and fruitful discussion during the research work.

I am very much indebted to my Co-supervisor Dr. Sk. Manjura Hoque, Head and Principal Scientific Officer, Materials Science Division, Atomic Energy Centre, Dhaka (AECD) for introducing the present research topic and for inspiring guidance and valuable suggestions throughout this research work. It would have not been possible for me to bring out this thesis without her help and constant encouragement.

I am indebted to Professor Dr. Jolly Sultana, Head, Department of Physics, Khulna University of Engineering & Technology for her strong support in various ways during the entire period of my study in this department.

I gratefully acknowledge Professor Dr. Md. Mahbub Alam, Department of Physics, Khulna University of Engineering & Technology, for his co-operation and inspiration during this work. My thanks are also for Md. Kamrul Hasan Reza, Md. Asaduzzaman, Mr. Sujit Kumar Shil, Assistant Professor and Mr. Alamgir Hossain & Suman Kumar Halder, Lecturer, KUET, for their moral support.

I would like to extend my special thanks to Professor Dr. Parimal Bala, chairman, Department of Physics, Jagannath University for his kindness and support whenever I needed. Also, I am grateful to all of my colleagues for their assistance and encouragement lightened the heavy load of postgraduate study.

My thanks due to Dr. Shireen Akhter, Director, Atomic Energy Centre, Dhaka, for her kind permission to use the laboratory of Materials Science Division, AECD.

I am deeply grateful to Dr. Dilip Kumar Saha, Director, Planning and Development Division, Bangladesh Atomic Energy Commission, for his generous help during XRD measurement and analysis. I wish to thank all the scientists of Materials Science Division, especially to Dr. Md. Mahbubul Haque, Dr. Nazrul Islam Khan, Mr. Fazul Kamal, Mrs. Samia Islam Liba for their support and scientific discussion to do this research work.

My special thanks to all the staff members of Materials Science Division, AECD, particularly Mrs. Alhamra Parveen, Mrs. Anjuman Ara Begum, Mr. Kamrul Islam, Mr. Anwar Hossain, Mr. Nurul Islam, Mrs. Nazmunnaahar Begum, Mrs. Zarna Begum and Mr. Kaiyoum for their sincere help during the preparation of the sample and experimental measurements.

I would like to express my heart full obligation thanks to my parents, sister, parents-in-laws and all other family members for their multifaceted support and love no matter distance. Words are not enough to express my feelings and sincere thanks to my loving husband Harinarayan Das, Senior Scientific Officer, Materials Science Division, AECD, for his understanding and being there always.

I also wish to thank to authority of Khulna University of Engineering & Technology for providing me with the necessary permission and financial assistance for conducting their thesis work.

Nipa Debnath



## ABSTRACT

Magnetic nanoparticles have drawn tremendous attraction from both fundamental aspect as well as applications in biomedicine such as magnetic bio-separation, detection of biological entities, magnetic resonance imaging, magnetic fluid hyperthermia and targeted drug delivery due to their fascinating magnetic properties. Superparamagnetic nanoparticles have become the focus of this study because their superparamagnetic, biocompatible and hydrophilic properties would be revealed after modifying the particle surface by suitable surfactants. Considerable research in this area has provided valuable in sites; however, suitable magnetic materials that can be fulfill all the requirements of MRI and hyperthermia applications are still under investigation.

This thesis reports on an investigation into the synthesis, control, and stabilization of high quality magnesium ferrite nanoparticles for biomedical application. A new understanding of the factors effecting nanoparticle growth in a co-precipitation methodology has been determined. Then the ferrimagnetic  $\text{MgFe}_2\text{O}_4$  nanoparticles were modified by annealed temperature from 200 to 1400°C using box furnace. The crystal structural, mean particle size and magnetic properties of the modified ferrimagnetic  $\text{MgFe}_2\text{O}_4$  nanoparticles were measured to investigate the effect of each process on the synthesized nanoparticles. The structural, morphological, magnetic properties of these synthesized products were characterized by using X-ray diffraction (XRD), Vibrating sample magnetometer (VSM), Mössbauer spectroscopy and NMR analysis.

XRD patterns of as-dried powder yielded single phase. No impurity peaks were detected. With the increase of annealing temperature, the width of peaks decreases which reflects the coarsening of particles. The smallest crystallite size about 3 nm was obtained for as-dried sample while the largest value 71.86 nm was obtained from the highest studied temperature 1400°C. The crystallite size of the nanoparticles abruptly increased with the annealing temperature. Magnetization measurements have been accomplished by VSM. It was found that saturation magnetization increases with the increase particle size. The small particles first exhibit superparamagnetic behavior at the early stage and then transform to ferromagnetic behavior when particle size passes the superparamagnetic limit. Interesting experimental results on the size dependent

magnetic properties at different temperatures have been found. Other structural and magnetic properties such as chemical isomer shift, quadruple splitting and hyperfine field were determined by Mössbauer spectroscopy. Superparamagnetic/ferromagnetic transition with the increase of particle size has also confirmed by this analysis. Mössbauer spectroscopy measurements are shown to evidence collective inter-particle correlations between the nanoparticles. The magnesium ferrite nanoparticles were then coated with biocompatible Chitosan (CS) and Polyethylene glycol (PEG). NMR spectroscopy was studied to investigate the spin-spin or  $T_2$  relaxivity values to determine its applicability in magnetic resonance images as MRI contrast agents.



## CONTENTS

	Page No.
Title Page	
Declaration Page	i
Acknowledgement	ii
Abstract	iv
Contents	vi
List of Figures	x
List of Tables	xiii
List of Symbols	xiv

## CHAPTER - I INDRUCTION

1.1	Nanotechnology	1
1.2	Nanomaterials	2
1.3	Magnetic Nanoparticles	4
1.4	Biomedical Applications of Nanoscale Magnetic Matreial	4
	1.4.1 Biosensor Applications	5
	1.4.2 Drug Delivery System	7
	1.4.3 Magnetic Resonance Imagaing	8
	1.4.4 Hyperthermia	10
	1.4.5 Bio-manipulation	11
	1.4.6 Multifunctional Nanoparticles in Biomedicine	12
1.5	Spinel Magnesium Ferrite	13
	1.5.1 Properties of Magnesium Ferrite	14
	1.5.2 Review of Researches on Synthesis and Characterization of Magnesium Ferrite	15
1.6	The Aims and Objectives of the Present Work	22
1.7	Outline of the Thesis	23

## CHAPTER - II

### THEORY OF NANOMAGNETISM

2.1	General Changes as a Function of Scaling	25
2.1.1	Surface to Volume Increases	25
2.1.2	Particles Size Approaching Characteristics Length Scales	26
2.2	Magnetism in Nanoparticles	26
2.2.1	Origins of Magnetic Domains	26
2.2.2	Anisotropic Effect of Single Domain Particles	27
2.2.3	Single Domain Limit	28
2.2.4	Magnetization Processes and Thermal Energy Effect	28
2.2.5	Superparamagnetism	29
2.2.6	Superparamagnetic Limit	32
2.3	Basic Concept of Nanoparticles Synthesis	34
2.3.1	Nucleation and Growth	34
2.3.2	Aggregation Phenomena	36
2.4	Synthesis Methods of the Nanocrystalline Ferrite	37
2.4.1	Preparation of Nanostructured Ferrites by Physical Method	37
2.4.2	Preparation of Nanocrystalline Ferrites by Wet Chemical Method	39
2.4.2.1	Synthesis of Nanocrystalline Ferrites in Aqueous Solution	40
2.4.2.1.1	The Co-precipitation Method	41
2.4.2.1.2	The Sol-gel Method	42
2.4.2.1.3	The Hydrothermal / Solvothermal Method	45
2.4.2.1.4	The Microemulsion Method	46
2.4.2.2	Synthesis of Nanocrystalline Ferrite in Non-Aqueous Method	49
2.4.2.2.1	The Polyol Method	50
2.4.2.2.2	Thermal Decomposition of Single Molecular Precursors	51

## CHAPTER-III

### SYNTHESIS AND CHARACTERIZATION TECHNIQUES

3.1	Synthesis of $\text{MgFe}_2\text{O}_4$ Nanoparticles	53
3.1.1	Materials	53
3.1.2	Experimental Procedure	53
3.2	X-Ray Diffraction	54
3.2.2	Determination of Nanocrystalline Grain Size by X-ray Diffraction	58
3.3	Vibration Sample Magnetometer	61
3.4	SQUID Magnetometer	63
3.5	Mössbauer Spectroscopy	67
3.5.1	Mössbauer Effect	68
3.5.1.1	Isomer Shift	69
3.5.1.2	Electric Quadrupole Splitting	71
3.5.1.3	Magnetic Splitting	74
3.5.1.4	Magnetic Hyperfine Interaction	76
3.6	Experimental Procedure for Mössbauer Spectrometer	77
3.7	Nuclear Magnetic Resonance Spectroscopy	81
3.7.1	Basic Principle of NMR	82
3.7.2	NMR Signal Processing	84
3.7.3	Relaxation Mode	85
3.7.3.1	Longitudinal Relaxation or $T_1$ -recovery	85
3.7.3.2	Transverse Relaxation or $T_2$ -recovery	86
3.7.4	NMR Instrumentation	87

## CHAPTER-IV

### RESULTS AND DISCUSSION

4.1	Structural Analysis	89
4.2	Magnetic Properties	97
4.2.1	Effects of Annealing Temperature on the Magnetic Properties	98
4.3	Mössbauer Study	108

4.4	NMR Study of Coated Magnesium Ferrite	115
-----	---------------------------------------	-----

**CHAPTER-V**  
**CONCLUSION**

5.1	Conclusion	120
-----	------------	-----

5.2	Suggestions for Future Work	121
-----	-----------------------------	-----

	<b>Reference</b>	132
--	------------------	-----

	<b>Conference Publications</b>	136
--	--------------------------------	-----

## List of Figures

<b>Fig.no</b>	<b>Description</b>	<b>Page</b>
Fig.2.1	Evolution of the magnetic energy with the tilt angle between the easy axis and the magnetization direction	27
Fig.2.2	Time constant vs. particles size for magnetite particles	31
Fig.2.3	Particle sizes vs. coercivity showing onset of superparamagnetism	33
Fig.2.4	Comparison of the M-H curves of (a) ferromagnetic and (b) superparamagnetic particles	33
Fig.2.5	LaMer's diagram describing the formation mechanism for monodisperse colloidal particles	34
Fig.3.1	Flow chart of MgFe <sub>2</sub> O <sub>4</sub> nanoparticles synthesis by chemical co-precipitation method	54
Fig.3.2	Bragg's diffraction patterns	56
Fig.3.3	Schematic diagram of X-ray diffraction	57
Fig.3.4	A PHILIPS PW3040 X'Pert PRO X-ray diffractometer	57
Fig.3.5	Effect of fine particle broadening in XRD (a) fine particles and (b) perfect crystal	59
Fig.3.6	Vibrating Sample Magnetometer- sample holder and detection mechanism	61
Fig.3.7	Vibrating Sample Magnetometer at materials Science Division, AECD	62
Fig.3.8	MPMS XL SQUID Magnetometer	64
Fig.3.9	Simple spectrum showing the velocity scale and motion of source relative to the absorber	69
Fig.3.10	Hyperfine splitting scheme for the <sup>57</sup> Fe Mössbauer transition induced by (a) Coulomb interaction (Isomer Shift), (b) Quadrupole interaction and (c) Hyperfine Splitting interaction between the nucleus and the electrons	70



Fig.3.11	Quadrupole splitting for $\frac{3}{2}$ to $\frac{1}{2}$ transition, The magnitude of quadrupole splitting, $\Delta$ , is shown	73
Fig.3.12	Magnetic splitting of the nuclear energy levels	75
Fig.3.13	Energy level scheme of $^{57}\text{Fe}$ Mössbauer spectroscopy involves the 14.4keV transition, intensities are given in % of decays	78
Fig.3.14	Scheme of Mössbauer Spectroscopy	79
Fig.3.15	Sample preparation for Mössbauer measurement	80
Fig.3.16	SEE Co. MS4 Spectrometer recording a Mossbauer spectrum	80
Fig.3.17	Velocity Transducer with the sample at room temperature	81
Fig.3.18	Energy splitting diagram for spin $I = \frac{1}{2}$ nuclei	82
Fig.3.19	Energy splitting diagram for spin $I - 1$ nuclei, there are $(2I + 1)$ possible orientations for each nucleus when external electromagnetic field is applied	83
Fig.3.20	$T_1$ relaxation	85
Fig.3.21	$T_2$ relaxation	86
Fig.3.22	$T_1(A)$ and $T_2(B)$ weighted images of human brain	86
Fig.3.23	The diagram of a typical NMR spectrometer	88
Fig.4.1(a)	XRD spectra of $\text{MgFe}_2\text{O}_4$ nanoparticles annealed at 200°C	90
Fig.4.1(b)	XRD spectra of $\text{MgFe}_2\text{O}_4$ nanoparticles annealed at 400°C	90
Fig.4.1(c)	XRD spectra of $\text{MgFe}_2\text{O}_4$ nanoparticles annealed at 600 °C	91
Fig.4.1(d)	XRD spectra of $\text{MgFe}_2\text{O}_4$ nanoparticles annealed at 800°C	91
Fig.4.1(e)	XRD spectra of $\text{MgFe}_2\text{O}_4$ nanoparticles annealed at 1000°C	92
Fig.4.1(f)	XRD spectra of $\text{MgFe}_2\text{O}_4$ nanoparticles annealed at 1200°C	92
Fig.4.1(g)	XRD spectra of $\text{MgFe}_2\text{O}_4$ nanoparticles annealed at 1400°C	93
Fig.4.2	Compare the X-ray diffraction patterns of the $\text{MgFe}_2\text{O}_4$ nanoparticles annealed at different temperatures	93
Fig.4.3	Variation of crystallite size with different annealing temperature for $\text{MgFe}_2\text{O}_4$ nanoparticles	94
Fig.4.4	Variation of lattice parameter with annealing temperature for $\text{MgFe}_2\text{O}_4$ nanoparticles	95
Fig.4.5	M (H) loops of $\text{MgFe}_2\text{O}_4$ nanoparticles for as dried sample taken at 300 K and 5 K up to maximum field of $\pm 60$ kOe. The inset of the figure	

	shows the magnified region around the origin to make the coercivity visible for the readers	98
Fig.4.6(a)	M-H loop of MgFe <sub>2</sub> O <sub>4</sub> nanoparticles annealed at 200°C	99
Fig.4.6(b)	M-H loop of MgFe <sub>2</sub> O <sub>4</sub> nanoparticles annealed at 400°C	99
Fig.4.6(c)	M-H loop of MgFe <sub>2</sub> O <sub>4</sub> nanoparticles annealed at 600°C	100
Fig.4.6(d)	M-H loop of MgFe <sub>2</sub> O <sub>4</sub> nanoparticles annealed at 800°C	100
Fig.4.6(e)	M-H loop of MgFe <sub>2</sub> O <sub>4</sub> nanoparticles annealed at 1000°C	101
Fig.4.6(f)	M-H loop of MgFe <sub>2</sub> O <sub>4</sub> nanoparticles annealed at 1200°C	101
Fig.4.6(g)	M-H loop of MgFe <sub>2</sub> O <sub>4</sub> nanoparticles annealed at 1400°C	102
Fig.4.7	Compare of M-H loops of MgFe <sub>2</sub> O <sub>4</sub> nanoparticles annealed at 200°C to 1400°C at room temperature	102
Fig.4.8	The expand graphs of origin region of hysteresis curve in the range of approximately -1000 to +1000 Oe	103
Fig.4.9	Variation of saturation magnetization with annealing temperature of MgFe <sub>2</sub> O <sub>4</sub> nanoparticles	104
Fig.4.10	The correlation between the coercivity and the annealing temperature of MgFe <sub>2</sub> O <sub>4</sub> nanoparticles	105
Fig.4.11(a)	Mössbauer spectra of as-dried MgFe <sub>2</sub> O <sub>4</sub> nanoparticles	108
Fig.4.11(b)	Mössbauer spectra of MgFe <sub>2</sub> O <sub>4</sub> nanoparticles annealed at 200°C	109
Fig.4.11(c)	Mössbauer spectra of MgFe <sub>2</sub> O <sub>4</sub> nanoparticles annealed at 400°C	110
Fig.4.11(d)	Mössbauer spectra of MgFe <sub>2</sub> O <sub>4</sub> nanoparticles annealed at 600°C	110
Fig.4.11(e)	Mössbauer spectra of MgFe <sub>2</sub> O <sub>4</sub> nanoparticles annealed at 800°C	111
Fig.4.11(f)	Mössbauer spectra of MgFe <sub>2</sub> O <sub>4</sub> nanoparticles annealed at 1000°C	111
Fig.4.11(g)	Mössbauer spectra of MgFe <sub>2</sub> O <sub>4</sub> nanoparticles annealed at 1200°C	112
Fig.4.11(h)	Mössbauer spectra of MgFe <sub>2</sub> O <sub>4</sub> nanoparticles annealed at 1400°C	112
Fig.4.12(a)	T <sub>2</sub> relaxivity by NMR spectroscopy MgFe <sub>2</sub> O <sub>4</sub> coated with Chitosan	116
Fig.4.12(b)	T <sub>2</sub> relaxivity by NMR spectroscopy MgFe <sub>2</sub> O <sub>4</sub> coated with PEG	116
Fig.4.13	MRI contrast agent MgFe <sub>2</sub> O <sub>4</sub> (a) coated with chitosan with respect to water (b) respective relaxation measured from these images are quoted in the figure	118

## List of Tables

<b>Table</b>		<b>Page</b>
Table 4.1	Average crystallite size and Lattice parameter of $\text{MgFe}_2\text{O}_4$ nanoparticles annealed at different temperatures	96
Table 4.2	Saturation magnetization $M_s$ , Coercivity $H_c$ , measured by VSM technique at room temperature for $\text{MgFe}_2\text{O}_4$ nanoparticles produced at different annealing temperatures	107
Table 4.3	Numerical values of Isomer Shift (IS), Quadrupole Splitting ( $\Delta E_q$ ) and Position of $\text{Fe}^{3+}$ , Hyperfine field ( $H_{hf}$ ) of $\text{MgFe}_2\text{O}_4$ nanoparticles annealed at different temperatures	114
Table 4.4	Relaxivity by NMR spectroscopy $\text{MgFe}_2\text{O}_4$ with the coating of Chitosan (CS) and PEG	119



## List of Symbols

XRD	=	X-Ray Diffraction
VSM	=	Vibrating Sample Magnetometer
FWHM	=	Full Width at Half Maximum
$T_m$	=	Melting temperature
$K_1$	=	Anisotropy constant
$H_c$	=	Coercive force
$\mu$	=	Permeability
$\mu_m$	=	Maximum permeability
$\mu_i$	=	Initial permeability
$\mu'$	=	Real part of the complex permeability
$\mu''$	=	imaginary part of the complex permeability
$D_g$	=	Grain size
B	=	Magnetic induction
H	=	Magnetic field
$\chi$	=	Susceptibility
$a_0$	=	Lattice parameter
Tan $\delta$	=	loss factor or loss tangent.
$M_s$	=	Saturation magnetization
$T_c$	=	Curie temperature
$T_a$	=	Annealing temperature
$\lambda$	=	Wave length of the X-ray
[hkl]	=	Index of the peak
I	=	X-ray beam of intensity
SPM	=	Superparamagnetic

**CHAPTER I**

**INTRODUCTION**



# INTRODUCTION

## 1.1 Nanotechnology

Nanotechnology controls the structure of matter at the nanoscale to produce new materials and devices with unique properties. However, some of these technologies have limited control over structure at the nanoscale, but these are being used to produce useful products. These are also being further developed to produce more sophisticated products with structure in controlled manners. Nanotechnology is very diverse field, ranging from extensions of conventional device physics to completely new approaches based upon molecular self-assembly and development of new materials with nanoscale dimensions to investigate the direct control on the atomic level. Nanotechnology involves application of several scientific fields comprises biomedical sciences, surface science, electronics, semiconductor physics, optics, magnetism, energy storage and electro chemistry [1.1]. There are many debates on the future implications of nanotechnology.

Nanotechnology may be able to produce many novel materials and devices with a vast range of applications in medicine, biomaterials, electronics and energy production. On the contrary, nanotechnology raises many questions like any advance technology regarding toxicity and environmental impact of nano materials [1.2], their potential effects on the global economy, and speculation about the several doomsday scenarios. Although, nanotechnology is recent advances in scientific research, however the development of its main concepts existed for a long period of time. The nanotechnology emergence in 1980s was due to convergence of advanced experiments like the invention of the scanning tunneling microscope in 1981 and fullerenes in 1985.

A nanometer (nm) is one billionth, or  $10^{-9}$  of a meter. In comparison, the typical length of carbon-carbon bond is in the range of 0.12 to 0.15 nm and the DNA double helix has a diameter of about 2 nm. By convention, nanotechnology is considered in the scale range of 1 to 100 nm according to the definition used by the National Nanotechnology Initiative United States. The lower limit is determined by the size of atoms (hydrogen has the smallest atoms, which are approximately one

quarter of nm in diameter). The upper limit is more or less arbitrary, but is approximately the size of the phenomena not observed in larger structures start to become apparent and can be used for nano-devices [1.3].

Nanotechnology not only created many high quality products at very low cost, but also allows producing nano-factories in the same low cost and at very fast speed. At the nano scale, electrical and magnetic properties are not the same as those of their bulk counterparts. For example, opaque substances turn into transparent (copper); stable materials turn combustible (aluminum); insoluble materials become soluble (gold). In general a chemically inert material such as gold can be tuned as a potent chemical catalyst at nanoscale.

There are many ways used to create nano structured materials, which are usually divided into two main strategies, top-down approach and bottom-up approach. The traditional top-down approach is limited by the miniaturization and precise manufacturing of semiconductor products at a smaller scale. Alternatively, in bottom-up approaches, nano structured materials are created from building blocks of atoms, molecules, clusters or nanoparticles in a controlled manner, governed by thermodynamic methods or new concepts such as self-assembly. Therefore, the idea of creating artificial substances and materials with unique features by using the bottom-up approach is increasingly encouraged for the development of new and multi-functional materials.

## **1.2 Nanomaterials**

Over the past two decades, a class of materials with a nano sized microstructure were prepared and studied. Nanomaterials have grain sizes on the order of a billionth of a meter. All materials are composed of grains, which in turn comprised many atoms. These grains are usually invisible to the naked eye, depending on their size. Conventional materials have grains varying in size from 100's of microns ( $\mu\text{m}$ ) to millimeters (mm). An average human hair is about 100 microns in diameter. The average size of an atom is on the order of 1 to 2Å in radius. 1 nanometer comprises 10Å, and hence in one nm, there may be 3-5 atoms, depending on the atomic radii. The nanomaterials are assembled from nanoscale building blocks, mostly crystallites. The building blocks can be different in their atomic structure,



chemical composition and crystallographic orientation. In cases, where the building blocks are crystallites, incoherent or coherent interfaces can be formed between them, depending on the atomic structure, the crystallographic orientation and the chemical composition of adjacent crystallites.

Recently, the synthesis of nanoscale magnetic materials has been an area of intense study, due to new microscopic properties shown by quantum-sized particles located in the transition region between atoms and bulk solids [1.4]. Quantum size effects and the large surface area of magnetic nanoparticles dramatically change some of the magnetic properties and present superparamagnetic phenomena and quantum tunneling of magnetization. Several research groups are engaged in investigations of the metal oxide nanoparticles because of their technological applications in magnetic and microwave devices, magnetic recording media, etc. Several types of nanomaterials such as metal (Fe, Co, Ni), metallic alloys (Fe-Cu) and metallic oxides ( $\text{MgFe}_2\text{O}_4$ ,  $\text{CoFe}_2\text{O}_4$ ,  $\text{MnFe}_2\text{O}_4$  and  $\text{ZnFe}_2\text{O}_4$ ) are under recent research activity, while metal nanoparticles have stability problems in atmospheric conditions. However, metal oxides are stable under ambient conditions.

Nanocrystalline materials are exceptionally strong, hard and ductile at high temperature, wear-resistant, erosion-resistant, corrosion-resistant, and chemically very active. Nanomaterials are also much more malleable than their conventional counterparts commercially available. The deviation of properties of the nano sized materials from those of bulk material is due to surface effects that depend primarily on the ratio of surface area to volume and particle size, together with the chemical composition and interaction between the particles.

The nanomaterials are classified into seven main categories [1.5].

- Carbon based nanomaterial
- Nanocomposites
- Metals and alloys
- Biological nanomaterial
- Nano-polymers
- Nano-glasses
- Nano-ceramics

### **1.3 Magnetic Nanoparticles**

In the past decade, the synthesis and use of magnetic nanoparticles has been intensively studied not only for its fundamental scientific interest but also for many technological applications. For example, magnetic nanoparticles were applied in different research fields, such as sensor developments, magnetic resonance imaging in medicine, drug delivery systems, hyperthermia, and magnetic separation [1.6]. The vast interest in nano structured particles mainly arises from the fact that these structures possess novel physical and magnetic properties that differ from the one of bulk materials. This is significant in the case of nanoparticles that have a large surface to volume ratio and the percentage of surface atoms is large, resulting in characteristic and distinct physical properties [1.7].

Magnetic nanoparticles are currently under consideration for possible application in magnetic particle hyperthermia (MPH) which is carried out by the rise of temperature of the malignant tissues under the exposure of rf current which excites superparamagnetic ferrite nanoparticles absorbed in the discard cells by Brownian and Neel relaxation. This leads to the destruction of malignant cells by the magnetic particle hyperthermia treatment while the healthy cells remain unchanged. Heat treatment or thermal therapy is potentially potent against cancer. The effects of heat on cancer cells are well-known. Cell depth from exposure to heat using MPH is a function of both the intensity of the applied heat controlled by the concentration of the absorbed ferrite nanoparticles and other magnetic properties. As a promising candidate for biomedical application the superparamagnetic nano ferrite are to be standard with biocompatible coating of chitosan and polyethylene glycol (PEG) as MRI contrast agent and hyperthermia treatment of cancer.

### **1.4 Biomedical Applications of Nanoscale Magnetic Materials**

Over time, the focus of nanotechnology research has gradually shifted from nanomaterials and investigation of their physicochemical properties to the use of these properties in several applications. One of the fields that can enormously benefit from the advancement in nanotechnology is biomedical research. In particular, highly specific medical interventions at the nano scale for curing disease and repairing



damaged tissues such as bones, muscles or nerves are emerging as nano medicine area [1.8].

Nanomaterials have a great impact on biomedical research especially in the last few years: superparamagnetic iron oxide nanoparticles as MRI contrast agent were studied and today these are commercial products [1.9]. Quantum Dots were also developed recently and are currently use in biology and medicine [1.10]. The great advantages of nanomaterials in the biomedical research field lies in its ability to operate on the same small scale as all the intimate biochemical functions involved in the growth, development and ageing of the human body [1.11]. Only in a few cases a particular nano structured material was developed completely for a specific biomedical application. More frequently, nanomaterials discovered in the past are now further developed and applied in different biomedical fields [1.8].

Still there are a lot of challenges for the use of nanoparticles in medical applications [1.12]. One of the main issues is certainly related to long-term safety of nanomaterials, both developed for *in vitro* and *in vivo* applications. Not only toxicology tests have to be developed specifically for nanomaterials, but also risk assessment and management have to be defined [1.13].

#### **1.4.1 Biosensor Applications**

In the last few years huge efforts were directed towards the development of diagnostic tools in order to improve the sensitivity of existing diagnostic techniques and to considerably reduce the time and labor required for analysis. Many biosensors take hours or even days and several successive steps and procedures are required to produce results, so there is a clear need for devices that operate on a short timescale [1.14]. Such devices could have a major impact on the diagnosis of several diseases by allowing at-risk patients to check tell-tale signs of proteins or other biomolecules by simply testing a small droplet of blood or serum [1.15].

A combination of magnetic nanoparticles and ultrasensitive magnetic field sensors is now a day's showing a great potential as a perfect team to achieve these goals. In these biosensors, the nanoparticles are coated or functionalized with chemical groups or entities that will bind to the biomolecule that need to be detected [1.16]. In the case of sensors on a substrate, these nanoparticle-biomolecule



complexes then react with “probes” molecules that are fixed onto the surface of the magnetic sensor. The presence of the magnetic nanoparticles on the surface produces an output signal. In the case of label-free biosensors, the nanoparticle - biomolecule complexes are directly detected by probing changes in magnetic properties of the nanoparticles after the binding events. These kind of label-free biosensors are extremely promising, especially for point of care applications, where the assay should be simple, requiring no or minimum preparation. The possibility of analyses detection directly in biological samples will lead to more economic, simple to use, versatile and flexible sensors [1.17].

A variety of diagnostic tests have been developed for the detection and quantification of biological molecules, e.g. antibodies, in different biological fluids. Traditional immune assays depend on the use of radioactive, fluorescent or enzyme labeled-antibodies as analytical tools to monitor biomolecular event [1.18]. The enzyme-linked immune sorbent assay (ELISA) is the most widely used for the detection of antibody-antigen interactions both in routine diagnostics and research. These kinds of assays have a main limitation due to the need of time consuming pre-treatment required for biological samples preparation prior to analyses [1.19-1.20].

Superparamagnetic iron oxide nanoparticles are used in several biomedical applications, including the quantification of biomolecular targets in cell and tissue extracts [1.21]. They have also been used to detect larger biological entities, such as bacteria, in solutions [1.22]. In most cases, commercial beads containing magnetic multi cores with different surface layers have been used but these detection systems have poor sensitivity and limited detection range due to a wide bead and magnetic domain size distribution.

To overcome these limitations, we applied a different strategy for sensitive detection of biomolecules in biological fluids. The sensing principle is based on susceptibility measurements in an alternating current (AC) magnetic field of the Brownian relaxation of functionalized magnetic nanoparticles [1.23]. AC susceptibility is an excellent detection technique, since it is simple, direct, and can be carried out in a compact device equipped with a simplified read out system. Recently, the detection of specific DNA strands after rolling circle amplification with commercial magnetic beads has been carried out measuring large changes in Brownian relaxation [1.24].

## 1.4.2 Drug Delivery Systems

Recent research on biocompatible materials has led to a great development of a specific field of medical devices engineering: the controlled drug delivery systems (DDS). DDS can be specifically designed to control the release rate and /or amount of therapeutic agents that will allow desired effects on target sites. Controlled drug release can be achieved by combination of carrier materials and active agents. There are a few classes of biocompatible materials used as carrier matrix for DDS, and these include solid lipid nanoparticles, [1.25] inorganic materials [1.26] spheres [1.27] and hydrogel systems [1.28] fabricated from biodegradable polymers.

Drug delivery systems can improve several crucial properties of “free” drugs, such as solubility, *in vivo* stability, pharmacokinetics, and bio-distribution, enhancing their efficacy and reducing side effects of the therapeutic compounds [1.29]. Thus, engineered DDS can prevent and considerably reduce risks related to under dosing and overdosing of therapeutic drugs in patients as well as decrease the risks of side effects [1.30].

There are several mechanisms used in the recent years to control the release rate of a drug. Most commonly, controlled DDS is generally the diffusion- and dissolution-based release system applicable to the release of drugs intended for the circulation or the localization on the site [1.31]. Recently, other mechanisms were also studied and developed in order to have a detailed and tuned release of active compound within specific tissues and cells, leading to so-called stimuli responsive DDS. Cationic lipids are used to cover the surface of nanoparticles and promote cellular uptake and thus drug delivery inside specific cells [1.32].

Mesoporous silica pores can also act as stimuli responsive DDS when the caps of the pore are removed by thiols compounds [1.33]. PH-responsive nanomaterials provide an alternate mechanism for release, relying on the acidic conditions inside tumor and inflamed tissues, cellular compartments including endosomes and lysosomes [1.34]. Towards this scope, magnetic nanoparticles were encapsulated in thermo sensitive polymers for controlled triggering of drug release [1.35]. Other thermo sensitive DDS were recently developed as thermo sensitive nanoparticles based on PNIPAAAN, a polymer which undergoes structural changes at a certain



temperature corresponding to the LCST [1.36]. Nanoparticles can also provide effective carriers for large biomolecules such as DNA, RNA, or proteins, protecting these biological entities from degradation and transporting them across the cell-membrane barrier. The success of “safe” delivery of these biomolecules provides access to gene therapy as well as protein-based therapeutic approaches.

Another strategy recently developed in the field of DDS is to engineer nano structured materials so that the release of drug would be triggered by the chemical environment [1.37]. For example, microgel responsive to the concentration of glucose has been developed for glucose-sensitive DDS [1.38]. Hydrogel based on poly (aspartic acid) and poly (acrylic acid) are demonstrated to be able to swell and shrink due to the change of salt concentration [1.39].

Magnetic stimulation has also been used as activating mechanism for the release of dopamine from nucleus accumbens shell of morphine-sensitized rats during abstinence [1.40]. DC magnetic field has also been used to control the release of drug from a hydrogel matrix in a “on-off” manner [1.41]. More recently, hydrogel constructed with thermo sensitive polymer and magnetic NPs has been prepared and such system is of great promise in drug delivery applications due to the dual stimuli-sensitivity [1.42]. Hydrogel materials were also reduced to nano scale, developing “nano hydrogels” for drug delivery that can easily evade the macrophage clearance with no opsonization or toxic effects [1.43].

Still there is a need to improve the hydrogel systems to be able to have inject able materials carrying a drug directly in the body without the need of surgical implantations. It is advantageous to have a drug delivery system responsive to external signals, such as magnetic field, so that the release rate could be carefully controlled to avoid under dosing and overdosing of the therapeutic compounds. Part of this thesis deals with the development of such novel ferro-gel systems combing external stimuli response with the possibility of injecting ferro-gel in a liquid state. There are no reports in to-date literature on such a system before.

### **1.4.3 Magnetic Resonance Imaging**

Among a number of imaging techniques, such as optical imaging, ultrasound imaging, positron emission tomography and X-ray tomography, Magnetic Resonance Imaging (MRI) is one of the most powerful non-invasive imaging modalities utilized

both in biomedical research and clinical medicine today [1.45-1.46]. The current development of magnetic nanomaterials, in particular nanoparticles, advances bio-imaging technologies in terms of sensitivity, special resolution and other critical parameters. MRI imaging is based on the property that hydrogen protons will align and process around an applied magnetic field,  $B_0$ . Upon application of a transverse radiofrequency (rf) pulse, these protons are perturbed from  $B_0$ . Then a relaxation phenomenon takes place where these protons return to their original state from the perturbed state. Two independent processes, called longitudinal relaxation ( $T_1$ -recovery) and transverse relaxation ( $T_2$ -decay), can be monitored to generate an MRI image. Local variation in relaxation, corresponding to image contrast, arises from proton density as well as the chemical and physical nature of the tissue under investigation [1.47].

To obtain better images with well-defined mapping, contrast agents are utilized during the imaging recording procedure. The main effect is to decrease relaxation times, either  $T_1$  and /or  $T_2$ , depending on the nature of the contrast agent used [1.48]. Normally, gadolinium and manganese chelates are clinically used to modify  $T_1$  relaxation [1.49], producing brighter images, while superparamagnetic iron oxide nanoparticles are used as  $T_2$  contrast agent, giving a darker contrast in the tissue where they are accumulated [1.50].

The effectiveness of a contrast agent can be described by its relaxivity, which is the proportionality constant of the measured rate of relaxation, or  $R_1$  ( $\frac{1}{T_1}$ ) and  $R_2$  ( $\frac{1}{T_2}$ ), over a range of contrast agent concentrations [1.47].

In the recent years, a lot of effort has been directed towards the development of magnetic nanoparticles as MRI contrast agents. The most common strategy consist of having iron oxide nanoparticles as magnetic core with tailored magnetic properties and size distribution, and different surface fictionalization to increase the stability of the suspension in biological fluids and to target specific tissues of the body [1.48]. Biocompatible polymers, inorganic materials such as silica and gold, small pharmaco pores such as peptides, small organic ligands and proteins are the main classes of compounds used to coat and functionalize the magnetic core of MRI contrast agent nanoparticles.



To illustrate the wide interest of iron oxide nanoparticles in MRI imaging, a few examples are reported here. Cancer research has received great benefits from MRI techniques and magnetic nanoparticles have been extensively developed to improve the detection, diagnosis and therapeutic management of solid tumors. Superparamagnetic iron oxide nanoparticles (SPION) are currently used for clinical imaging of liver tumors and prostate, breast and colon cancers as well as for the delineation of brain tumor volumes and boundaries [1.51]. Next generation of active targeting based on nanoparticles has a potential to offer significantly improved tumor detection and localization by exploiting the unique molecular signatures of these diseases [1.52]. Other applications of magnetic nanoparticles enhanced MRI are in the field of cardiovascular medicine, including myocardial injury, atherosclerosis and other vascular diseases [1.53].

Molecular imaging, defines as the non-invasive *in vivo* visual representation, characterization, and quantification of biological processes at the cellular and molecular levels, has also been greatly affected by nanoparticles development. For instance, molecular imaging allows sensitive and specific monitoring of key molecular targets and host responses associated with early events in carcinogenesis and other diseases [1.54].

Targeting of the inflammatory endothelial tissues was successfully performed with superparamagnetic contrast agent both *in vitro* and *in vivo* models of inflammation [1.55]. Another successful application is specific tracking of cells *in vivo* after loading them with magnetic nanoparticles functionalized with peptides and transfect ion agents [1.56]. Novel applications of nanoparticles and MRI in molecular imaging are related to studies of cell migration and trafficking, apoptosis detection and imaging of enzyme activities [1.57].

#### **1.4.4 Hyperthermia**

In the numerous applications of nanomaterials in medicine, cancer treatments with nanoparticles have received great attention instead of traditional chemical therapy [1.58]. In the last few years, a lot of studies have been conducted on magnetic nanoparticles that generate heat when an alternating magnetic field is applied. This phenomenon is called hyperthermia and it is extremely dependent on the size distribution of nanoparticles as well as their magnetic properties [1.59]. In most

studies, superparamagnetic nanocrystals suspensions are tested in order to check the ability of energy absorption from an oscillating magnetic field and its conversion into heat. This property can be used *in vivo* to increase the temperature of tumor tissue and to destroy the pathological cells by hyperthermia, since tumor cells are more sensitive to temperature increase than healthy ones. The main parameter determining the heating of the tissue is the specific absorption rate (SAR), defined as the rate at which electromagnetic energy is absorbed by a unit mass of a biological material. For magnetic nanoparticles with superparamagnetic properties, the SAR is precisely determined by the volume ratio of nanoparticles in the tissue and was theoretically explained [1.60].

Recent strategies for hyperthermia treatment are focusing in delivering and accumulating magnetic nanoparticles in specific tissue. This has been proved *in vitro* by selective remote inactivation of cancer cells by an AC magnetic field and evaluation of the feasibility and survival benefit of this new hyperthermia approach is in progress on animals, and first clinical trials have been started recently [1.61]. Superparamagnetic nanoparticles are seen as a very promising agent for hyperthermia treatments, especially in the form of multifunctional drug delivery system, but this new field of application requires great reproducibility, control of size and magnetic properties during the synthesis of nanomaterials.

#### **1.4.5 Bio-manipulation**

In the recent years, a lot of effort has been put in the field of manipulation and remote control of specific cellular components *in vitro*, and more importantly, *in vivo*, giving clinicians and scientists a powerful tool for investigating cell function and molecular signaling pathways [1.62]. Furthermore, micro particles and nanoparticles have been used in the field of biotechnology for different applications, including protein separation and purification, protein detection and analysis, DNA extraction and bio-catalytic transformations [1.63-1.65].

Magnetic separation techniques have several advantages in comparison to traditional separation procedures: the process is very simple and all steps of the purification can take place in one test tube without expensive liquid chromatography systems [1.66]. Magnetic materials in nanoscale dimensions have been widely used



for affinity isolation of proteins for capture and detection of bacteria at low concentration and for separation of proteins from biological samples [1.67].

Magnetic nanomaterials are useful tools for investigation of cell functions and molecular signaling pathways, giving the possibility of probing ion channel activity, apoptosis mechanisms, protein production and stress response. The actuation of magnetic particles provides several advantages over other techniques for remote cell manipulation, such as optical tweezers, nano indentation and nano patterned arrays. The main advantage is that the process allows remote control of the nanoparticles at a distance, giving the possibility of using this technique for future in-vivo applications. Magnetic nanomaterials, in particular nanoparticles attached to membrane receptors, have been used since more than a decade to investigate properties of the cytoplasm under an applied stress [1.68]. Recently, by using magnetic actuation to apply controlled forces on the cell membrane, in combination with nanoparticles with different binding capabilities, biochemical pathways and ion channel kinetics have been studied [1.69].

Tissue engineering and regenerative medicine are two main fields of research where the magnetic manipulation of cells with nanomaterials is exploring new horizons. In addition to biochemical signaling, mechanical cues provide important stimuli that promote the production of functional tissue matrix from stem cells [1.70].

Magnetic support-based separation and responsive hydrogel-based separation have also been exploited in the bio-separation field, including applications as cell separation enzyme immobilization, and protein purification [1.71]. The magnetic separation approach has several advantages compared with conventional separation methods; it can be performed directly in crude samples containing suspended solid materials without pretreatment, and can easily isolate some biomolecules from aqueous systems in the presence of magnetic gradient fields. The latter separation approach utilizes the unique swelling properties of stimuli-responsive hydrogels to concentrate or separate dilute biomolecule solutions [1.72].

Recently, gene delivery and transfection were achieved both *in vitro* and *in vivo* with the use of magnetic nanoparticles, opening the field of magneto-faction: development of non viral transfection agents for gene delivery [1.73].

### **1.4.6 Multifunctional Nanoparticles in Biomedicine**

A common trend in the nano medicine research field is to combine different functionalities within a single nanoscale device, capable to achieve different tasks simultaneously, such as targeting specific cells or compartments, drug delivery and imaging.

The attachment of targeting agents to magnetic nanoparticles is used to increase the specific accumulation of multifunctional nanoparticles within pathogenic tissues. These structures not only deliver a drug, but also have a large surface area-to-volume ratios allowing for a large number of therapeutic molecules to be incorporated or attached to individual nanoparticles [1.47].

In addition, the magnetic properties of the nanoparticles may be used for specific targeting of these systems by external magnetic fields, to provide imaging modality for monitoring therapeutic effects through MRI and /or to have alternative source of treatment through magnetic fluid hyperthermia therapy [1.59].

Multifunctional nanoparticles consisting of polymeric micelles encapsulating iron oxide nanoparticles and fluorescent quantum dots are recently reported as MRI-fluorescent ultra sensitive markers. Mesoporous silica coated magnetic particles are also being prepared and studied for drug delivery and simultaneous MRI imaging [1.74]. Several other types of multifunctional nanoparticles with the potential to integrate therapeutics and diagnostics functions into a single nano-system have been recently developed, both for in-vitro studies and for in-vivo use [1.75].

Multifunctional nanoparticles are being developed more frequently for different purposes, with the final goal of greatly improving diagnostics capabilities of several diseases and developing specifically controlled in-situ therapy, personalized for particular sickness and patient. The design of such multifunctional nanoparticles is the key issue in order to achieve these goals, allowing nano-systems to be targeted to specific tissues, cells and even intracellular compartment [1.76].

### **1.5 Spinel Magnesium Ferrite**

Magnesium ferrite belongs to a class of soft ferrites having the general formula  $MFe_2O_4$  with spinel cubic structure.  $Mg^{2+}$  is a non-magnetic ion and has no



contribution in the magnetic moment of  $\text{MgFe}_2\text{O}_4$ , which is thus entirely due to the uncompensated spins of the un-evenly distributed iron ions at two (A & B) sites. Magnesium ferrite is a typical spinel in which the cation distribution in the crystal lattice site is very much sensitive to heat treatment due to high diffusibility of  $\text{Mg}^{2+}$  ions [1.77]. The interesting physical and chemical properties of ferrosinels arise from their ability to distribute the cations among the tetrahedral (A) and octahedral (B) sites [1.78]. Further, various studies have shown that magnetic and electrical properties are strongly linked to the structural properties, which are controlled by the synthesis method. It also shows that substitution of different metal cations has different effects on the distribution of cations within the spinel lattice. As a result, a cation adjustment in spinel ferrites is a suitable approach for tuning magnetic and electrical properties to suit intended applications. The change in magnetization and conduction due to change in composition depends on the site occupancy and magnetic moment contribution and electron hopping of the cations, its analysis can be used to deduce trends in site occupancy with substitution.

In nano crystalline magnesium ferrite, many of the useful properties of its crystalline counterpart, such as magnetization, are enhanced. Further, magnesium ferrite belongs to class of soft magnetic materials which is easy to magnetize and demagnetize, so are used in electromagnets. Owing to its nano crystalline nature and useful properties, the material shows a good potential for novel applications in humidity, gas sensing [1.79] and drug delivery [1.80].  $\text{MgFe}_2\text{O}_4$  is also known for its good photoelectric effect [1.81-1.82]. Apart from its magnetic and electronic applications,  $\text{MgFe}_2\text{O}_4$  finds a number of applications in heterogeneous catalysis [1.83-1.85]. Moreover, magnesium ferrite and its allied compounds have wide spread applications in microwave devices such as circulators, insulator, phase shifters and multifunctional devices because of their low magnetic and dielectric losses and high resistivity [1.86-1.89].

### **1.5.1 Properties of Magnesium Ferrite**

The magnesium ferrites have attracted the attention of researchers since past few decades. One reason for this is the great potential of this material for applications, which are based on higher values of saturation magnetization, Curie temperature and electrical resistivity together with low dielectric losses and moderate coercive field.

The ordering of the magnetic moments of ferric ions and the strong exchange interactions explain the excellent magnetic behavior of this material [1.90].

The trouble with the other electro-magnetic materials is their low electrical resistivity which offers the induced currents (called eddy currents) to flow within the materials, thus producing heat. This generated heat is often a serious problem and become a cause for wastage of energy. Thus, the materials become inefficient due to wastage of energy, especially as the frequency is high enough. However, the performance of soft magnetic materials like  $\text{MgFe}_2\text{O}_4$  is much better at high frequencies due to their high electrical resistivity [1.91]. Moreover, high permeability and time/temperature stability are some additional important features that have expanded the usage of soft ferrites in high frequency and delay lines, broadband transformers, adjustable inductors, quality filter circuits and other high-frequency circuit's electronics. At high frequencies, the use of soft ferrites is relatively more systematic with respect to that of the other circuit components whose performance must be improved. An important factor in the choice of soft ferrites is that they are generally less expensive than magnetic metals and alloys. Soft ferrites are the best option of the core material for operating frequencies from 10 kHz to a few hundred MHz with proper combination of low cost, high inductor quality, high stability and low volume. In addition, no other magnetic material possesses magnetic and mechanical parameters as flexible as those of soft ferrites.

### **1.5.2 Review of Researches on Synthesis and Characterization of Magnesium Ferrite**

Oliver et al. [1.92] used the sol-gel supercritical drying method to synthesize the fine powder of  $\text{MgFe}_2\text{O}_4$ , which was calcined at two different temperatures i.e. 773 K and 1073 K. The powder structure was matched with the spinel phase of  $\text{MgFe}_2\text{O}_4$  and  $\text{Fe}_2\text{O}_3$ , as an impurity been observed in samples. Superparamagnetic nature was observed in as-produced powders at room temperature, having single magnetic domain particle with size of 11 nm. The particle size distribution was evaluated by fitting the magnetization data to a Langevin function, and confirmed by Mossbauer spectra measured at temperature range 25 - 298 K. Very similar particle size distributions were observed for all three methods. The saturation magnetization



and magneto-crystalline anisotropy values were observed to be same for both bulk and nanoparticle and did not change with the size of particles.

Zimnol et al. [1.93] prepared the epitaxial thin films of  $\text{MgFe}_2\text{O}_4$  by solid state reactions between MgO substrates and FeO vapors. The different compositions of epitaxial spinel films were obtained having wide range of magnetic properties. The deposited films were characterized by using X-ray diffraction (XRD), Rutherford back scattering spectroscopy (RBS), Energy dispersive X-ray spectroscopy (EDX), Transmission electron microscopy (TEM) and Selected area electron diffraction (SAED). Magnetic hysteresis loops were measured using the magneto-optical Faraday Effect.

Chen et al. [1.94] prepared  $\text{MFe}_2\text{O}_4$  ( $\text{M} = \text{Cu}, \text{Zn}, \text{Cd}$  and  $\text{Mg}$ ), with a large specific surface area of  $40 - 80 \text{ m}^2\text{g}^{-1}$  by a co-precipitation method and tested for sensing there duping gases like  $\text{CO}$ ,  $\text{H}_2$ , LPG,  $\text{C}_2\text{H}_5\text{OH}$  and  $\text{C}_2\text{H}_2$ . The gas sensitivity of ferrites varied in the order  $\text{MgFe}_2\text{O}_4 \sim \text{CdFe}_2\text{O}_4 > \text{CuFe}_2\text{O}_4 > \text{ZnFe}_2\text{O}_4$  due to varying the specific surface area or grain size. It was observed that  $\text{MgFe}_2\text{O}_4$  and  $\text{CdFe}_2\text{O}_4$  were the most sensitive and selective to LPG and  $\text{C}_2\text{H}_2$ , respectively, among the ferrites tested.

Liu et al. [1.95] studied a correlation between the electron spin-orbital angular momentum coupling and the superparamagnetism in  $\text{MgFe}_2\text{O}_4$  and  $\text{CoFe}_2\text{O}_4$  nanoparticles. The neutron diffraction studies have shown that the cation distribution and contribution to the magnetic anisotropy from the  $\text{Fe}^{3+}$  lattice sites is almost the same in both nano-crystallites. The blocking temperature of  $\text{CoFe}_2\text{O}_4$  nanoparticles is  $150^\circ\text{C}$  higher than that of the same sized  $\text{MgFe}_2\text{O}_4$  nanoparticles due to more anisotropic nature of  $\text{Co}^{2+}$  ions and confirmed by Mössbauer spectroscopic studies which demonstrate that the magnetic anisotropy of  $\text{CoFe}_2\text{O}_4$  nanoparticles is higher than that of the same size  $\text{MgFe}_2\text{O}_4$  nanoparticles, which can be controlled by adjusting the magnetic anisotropy energy of nanoparticles.

Sepelak et al. [1.96] investigated the effects of high energy milling on  $\text{MgFe}_2\text{O}_4$ . The crystallite size of  $\text{MgFe}_2\text{O}_4$  can be reduced to nanometer range by mechanical treatment and also control the redistribution of cations between tetrahedral and octahedral sites. The thermal stability range of mechanically induced metastable states is studied by the change in temperature.

Sepelak et al. [1.97] investigated the changes in  $\text{MgFe}_2\text{O}_4$  caused by high-energy milling, using Mössbauer spectroscopy, magnetization measurements, and electron microscopy. The observed enhancement of the magnetization in nanoscale milled  $\text{MgFe}_2\text{O}_4$  is discussed on the base of cation redistribution and spin canting.

Rabanal et al. [1.98] studied the magnetic properties of powdered  $\text{MgFe}_2\text{O}_4$  processed with a centrifugal mill. The starting ferrite powder was prepared by solid-state reaction occurred at 1400 °C for 48 h. The crystalline size and internal strain were evaluated by XRD data using Williamson-Hall and Debye-Scherrer methods. The nanoparticles were obtained for low milling time. The X-ray analysis indicates that the 17h of milling caused the appearance of two  $\alpha\text{-Fe}_2\text{O}_3$  peak. The saturation magnetization remains nearly constant at 39.2 emu/g indicates the lack of inversion degree even for longer milling times, while coercivity increase up 576.7 Oe due to internal stresses caused by the mechanical grinding.

Chhaya et al. [1.99] investigated the  $\text{Ca}^{2+}$  doped  $\text{MgFe}_2\text{O}_4$  without altering the cubic symmetry and affecting the structural, magnetic and electrical properties of  $\text{Mg}_{1-x}\text{Ca}_x\text{Fe}_2\text{O}_4$  ( $x = 0.0\text{-}0.35$ ) spinel ferrite system studied by means of X-ray diffraction(XRD), magnetization, AC susceptibility and DC resistivity measurements. The variation of magneton number with  $\text{Ca}^{2+}$  content can be explained on the basis of Néel's collinear spin model. The Néel temperature determined through AC susceptibility and DC resistivity measurements is in close agreement with theoretical values. The variation in electrical resistivity coincides with the change in activation energy.

Turkin et al. [1.100] synthesized  $\text{MgFe}_2\text{O}_4$  annealed at 1373 K using silica-tube technique. The product is homogeneous and fine grained with the inversion parameter of 0.75. The calorimetric measurements indicate the second-order phase transition of antiferromagnetic to paramagnetic materials at 597 K. This silica-tube technique of the synthesis prevents the escape of oxygen at long heating.

Verma et al. [1.101] synthesized nanosized magnesium ferrite using mild microwave hydrothermal (MH) conditions. The average particle size of the ferrite is found to be  $\sim 3\text{nm}$  calculated from X-ray diffraction and transmission electron microscopic analyses. Vibrating sample magnetometric studies indicate the superparamagnetic nature of ferrite particles.



Liu et al. [1.102] synthesized n-type nanomaterials ( $\text{MgFe}_2\text{O}_4$ ) by convenient, environment friendly, inexpensive solid-state reaction method. The material structure and crystallite microstructure of samples have been evaluated by X-ray diffraction (XRD), Transmission electron microscopy (TEM) and High-resolution transmission electron microscopy (HRTEM). Conductance responses of the  $\text{MgFe}_2\text{O}_4$  were measured by exposing the thick film to reducing gases like methane ( $\text{CH}_4$ ), hydrogen sulfide ( $\text{H}_2\text{S}$ ), liquefied petroleum gas (LPG) and ethanol gas ( $\text{C}_2\text{H}_5\text{OH}$ ) and observed various sensing responses to these gases at different operating temperature. Successive on and off responses have been repeated and no major changes in the response signal were seen.

Bergmann et al. [1.103] reported the single-step synthesis of nano sized  $\text{MgFe}_2\text{O}_4$  via mechano-chemical processing of oxide precursors. The synthesized materials were subjected for X-ray diffraction and  $^{57}\text{Fe}$  Mössbauer spectroscopic analyses. The transmission electron microscopy assured the nanoscale nature of the mechano synthesized material.

Sepelak et al. [1.104] reported the magnetization enhancement in nano-sized mechano-synthesized  $\text{MgFe}_2\text{O}_4$  and discussed on the basis of a modified core-shell model. Due to random distribution of cations, the surface shell of nanoparticles exhibits an effective magnetic moment 2 times greater than that of the particle core. The thickness of surface shell is calculated from the size-dependent magnetization measurements.

Ichiyangi et al. [1.105] prepared the  $\text{MgFe}_2\text{O}_4$  nanoparticles by using wet chemical method. The particle size estimated from X-ray diffraction patterns were in the range of 3 to 8 nm. Magnetization measurements were performed under an applied field of 750 kOe. Both the field-cooled (FC) and the zero-field-cooled (ZFC) magnetization dependent blocking temperature,  $T_b$ , were observed to be around 30 K. A high coercivity of  $\sim 1000\text{Oe}$  was observed at 5 K. A big difference in magnetization was observed between the quenched samples and annealed samples.

Deng et al. [1.106] developed a low-temperature solvothermal synthetic route for synthesis of uniform-sized  $\text{MFe}_2\text{O}_4$  ( $M = \text{Mg, Cu, Ni}$ ) ferrite. The size of the as-prepared ferrite microspheres could be controlled in the range of 300–800 nm by adjusting some growth parameters. The X-ray powder diffraction (XRD),

Transmission electron microscopy (TEM), Scanning electron microscopy (SEM) and Energy-dispersive X-ray analysis (EDAX) were employed for structural investigation of the as-prepared ferrite microspheres. The magnetic properties measurements were also carried out for as prepared materials.

Shah et al. [1.107] reported the addition of 2 wt%, 4 wt% and 6 wt% cerium oxide to  $\text{MgFe}_2\text{O}_4$  prepared by a ceramic method. They observed the decrease in resistance from 52M to 2M with the addition of 6 wt% cerium oxide. The humidity generated is in the range of 10% RH to 90% RH at 25 °C. The addition of cerium oxide increases the inter granular porosity, distribution of pore size and open pores in the system. The addition of cerium oxide improves the sensitivity and shows a better linearity than that of pure magnesium ferrite. XRD analysis confirms the spinel phase formation of the samples and the calculated value of porosity is confirmed by the scanning electron micrographs of the samples.

Pradeep et al. [1.108] synthesized  $\text{MgFe}_2\text{O}_4$  nanomaterials using sol-gel auto-combustion method and performed the XRD analysis for structural studies of the as-synthesized materials. The particle size and lattice constant are obtained using XRD data. The site preference of cations in nano-  $\text{MgFe}_2\text{O}_4$  is compared with its bulk counterpart. The Scanning Electron Microscopy (SEM) was utilized for morphological features of the prepared nanoparticles. Fourier transform infrared spectroscopy (FTIR) assures the formation of spinel structure and revealed the effect of nanosized synthesis on various parameters such as bond length, vibration frequency and force constant. The M-H loops of specimens have been measured using vibrating sample magnetometer (VSM) and magnetic parameters such as saturation magnetization ( $M_s$ ), coercivity ( $H_c$ ) and retentivity ( $M_r$ ) are determined from VSM data.

Sasaki et al. [1.109] synthesized magnesium ferrite ( $\text{MgFe}_2\text{O}_4$ ) by hydro thermal route for which suspensions of  $\text{Mg}(\text{OH})_2$  and  $\text{Fe}(\text{OH})_3$  in appropriate ratio was prepared and pressurized to 30 MPa by high-pressure pump followed by rapid heating to the reaction temperature. The Mg/Fe molar ratio varied from 0.5 to 1.5 to obtain single-phase  $\text{MgFe}_2\text{O}_4$ . The stoichiometric ratio of Mg/Fe = 0.5 contains both  $\text{MgFe}_2\text{O}_4$  and  $\alpha\text{-Fe}_2\text{O}_3$  while, at Mg/Fe = 1.0 and 1.5, the single-phase  $\text{MgFe}_2\text{O}_4$  is obtained.  $\text{MgFe}_2\text{O}_4$  synthesized in the present study with particle size of 20 nm, exhibits superparamagnetic behavior.



Ahmed et al. [1.110] synthesis magnesium ferrite compacts by using a mixture of magnetite ore and waste iron oxide (mill scale). They investigated the effect of different mixture composition and sintering conditions on the phase change, and then evaluated the compressive strength, physical and magnetic properties of sintered compacts. A single phase ferrite obtained from a mixture of 40 weight% magnesium ore and 60 weight% mill scale possessed low porosity and high saturation magnetization

Burianova et al. [1.111] presented a comparative study of magneto caloric effect (MCE) in superparamagnetic (SPM) regime in two different types of magnesium viz;  $\text{MgFe}_2\text{O}_4$  encapsulated in amorphous  $\text{SiO}_2$ , or as matrix-less nanoparticles synthesized in supercritical water conditions. XRD and TEM analyses were employed to assess the particle diameter of all prepared samples. The entropy change,  $S$  was derived from the magnetization,  $M(H,T)$  curves measured at specific temperature intervals. They observed a broad peak of  $S$  for all the samples in the temperature range above the  $T_B$ .

Bharti et al. [1.112] synthesized magnesium ferrite, zinc ferrite, and magnesium zinc ferrite using an economic wet chemical synthesis technique. Phase formation of the synthesized powders has been confirmed by infrared spectroscopy and X-ray Rietveld refinement analyses. The structural features of these materials have been correlated with their magnetic properties. Single phase magnesium zinc ferrite nano-particles were investigated for carbon monoxide and hydrogen gas sensing properties. The response and recovery transients of conductance were modeled using Langmuir adsorption kinetic shaving two active sites in the sensing elements named as CO sensors. The activation energies for response and recovery behavior of these two adsorption sites were found to be different. This difference in activation energies for response and recovery is due to different chemo-adsorbed oxygen species in these two sites.

Dalt et al. [1.113] investigated the synthesis of nano structured  $\text{MgFe}_2\text{O}_4$  through solution combustion technique. The 30% fuel-deficient formulation was selected to synthesized powders at different furnace temperatures. The structural and morphological characterizations were performed by using X-ray diffraction and Transmission Electron Microscopy (TEM). Mössbauer spectroscopy and vibrating sample magnetometer (VSM) were employed for magnetic measurements. Crystallite



sizes of  $\text{MgFe}_2\text{O}_4$  around 42.8 nm calculated from the XRD pattern were consistent with the results obtained from TEM analysis.

Patil et al. [1.114] reported the synthesis of spinel  $\text{MgFe}_2\text{O}_4$  by a simple, inexpensive combustion method and applied as a gas sensor for reducing gases (LPG, Acetone, Ethanol, Ammonia). The reducing gas sensing properties as a function of structural and surface morphological properties has been studied. The structural and morphological features were analyzed by XRD and SEM respectively. The porous morphology revealed by SEM analysis owed to decrease with the grain growth by an increase in sintering temperature. The maximum response of 71% to 2000 ppm of LPG was observed at 698 K with the synthesized material.

In recent years, nanomaterials have emerged as a rapidly advancing field, providing vast avenues of research. Rapid growth in the demand for telecommunication and high-frequency magnetic devices require production of materials with significant improvements in their performance with lower fabrication costs. The literature of the last 10 - 15 years reveals that spinel magnesium ferrites of different compositions have been extensively studied and used in technological products. However, the search for a better product with lowest energy consumption and optimum performance is still going on.

On the base of literature survey carried out for magnesium ferrite spinel; it is observed that the efforts of the researchers have been mainly concentrated on the synthesis of single crystals, bulk materials, thin films and nanosized structures by using a variety of well known methods including the co-precipitation method, sol-gel and solid state method. The physical, magnetic and electrical properties of ferrite materials depend upon the synthesis routes, chemical composition, annealing temperature and distribution of metal ions at A- and B-sites. The conventional ceramic method of preparation involves the mixing of suitable metallic oxides with appropriate grinding followed by a solid-state reaction at high annealing temperatures of 1573 - 1973 K. Though the route is quite simple yet it has several drawbacks, such as; high sintering temperature, large reaction time, large particle size and limited degree of homogeneity. However, chemical methods like co-precipitation, spray-pyrolysis and sol-gel etc., are preferable because apart from the advantages of an economical and low-temperature processing, these methods make it possible to obtain nanosized ferrite materials. Although the aforesaid methods are capable of producing

nanometric ferrites, but the quality of producing nanoparticles in many cases has a large size distribution along with the arbitrary size control. In most of these methods, size variation is achieved through annealing at various temperatures. If multiple sizes are produced by the synthesis without thermal annealing or without changing the thermal annealing temperature, often major changes in the synthesis procedure is required [1.115].

To correlate size effects with changes in magnetic and electric properties, it is essential to select a synthesis method which allows controlling the size of nanoparticles with a narrow size distribution [1.116]. Chemical co-precipitation method is preferred over other methods for the reason stated above and has many advantages; especially low temperature wet chemical synthesis to obtain single-phase materials. It is also easier and cost effective than the other chemical methods. The chemical co-precipitation method has been known to successfully prepare nano crystalline spinel ferrites with the particle sizes less than 50 nm.

## **1.6 The Aims and Objectives of the Present Work**

This study is aimed to developed nanosized magnetic particles to develop MRI contrast else with the efficiency of MRI contrast enhancement. We expect the  $\text{MgFe}_2\text{O}_4$  nanoensemble is to exploit their pronounced ability to absorb the energy of the low frequency fields which is suitable for magnetic particle hyperthermia and the potential for biomedical application. Magnetic properties of these nanoparticles will be optimized under a composition, structure and size controlled conditions. The variation in those magnetic properties will be attempted by promoting atomic rearrangements between the tetrahedral (A) and octahedral sites (B) in the ferrite structure. Ferrites nanoensemble are much more economic than the rare earth based contrast agents. Extensive research is being pursued in order to derive the properties and potentials of SPION in the spinel ferrites of other composition from the perspective of better biocompatibility, biodegradability element than Fe, an attempt will be made to explore the possibility of its biomedical applications exploiting the superparamagnetic properties of  $\text{MgFe}_2\text{O}_4$  nanoensemble.



Following steps will be taken to achieve the objectives:

- Synthesis of magnesium ferrite nanoparticles: The synthesis will be done by co-precipitation method, using nitrate salt as precursor materials in aqueous solvent and sodium hydroxide as the precipitate agent.
- The as-dried product will be treated thermally at various temperatures from 200 to up to 1400°C to study on crystallite size evolution.
- Structural Analysis: XRD characterization will be done to know about the crystal structure and crystallinity. Mössbauer studies will be performed to analysis the cation distribution. We will also measure the Isomer shift, Quadrupole splitting and Hyperfine field splitting.
- Magnetic measurement: The VSM and SQUID characterization will be performed to study the magnetic behavior of synthesized materials, along with all the characterizations like saturation magnetization and coercivity. The spin dynamics of the nanoensemble and their bulk magnetic properties will be studies by the field dependence of magnetization measurements.
- NMR study: To evaluate the possible application of obtained nanoparticles as both  $T_1$  and  $T_2$  contrast agents in magnetic resonance imaging (MRI), NMR study will be performed. Ferrite nanoparticle based  $T_2$  contrast agents such as Feridex, has also been developed and are now used clinically to obtain better  $T_2$  images.

## 1.7 Outline of the Thesis

This thesis deals with development of tailored magnetic nanomaterials for different bio-applications, such as early diagnosis of diseases and injectable drug delivery systems. The common base of the different studies included is the engineering approach to tackle a problem: first specific requirements about the problem are acquired, determining the main objective that has to be reached. Then some possible strategies are proposed and the most viable ones are chosen in order to guide the work, and after following these guidelines scientific data are collected and the results are discussed in order to check whether they fulfill the expected objectives and requirements. This is an iterative procession order to develop and improve the strategies and the results step by step.



Chapter I includes the introduction and the objectives of the present thesis. The theoretical background, which includes the fundamentals of magnetism, general information on the ferrite nanoparticles as well as the synthesis technique will be presented in chapter II. The methodology of the synthesis samples and characterization techniques is the next part of this thesis and is presented in chapter III. This section also includes details of the experimental procedure. Chapter IV presents the main findings of the research and the corresponding interpretation. The concluding remarks are summarized in Chapter V.

## **CHAPTER II**

# **THEORY OF NANOMAGNETISM**

# THEORY OF NANOMAGNETISM

## 2.1 General Changes as a Function of Scaling

Nanostructures and systems are of great interest beyond the simple scaling down of larger systems. Although it is useful to create smaller versions of large systems that do the same work, like smaller hard drives, it is not the sole motivation for nano research. A primary motivation is the fact that nano scale systems have entirely different and often very useful properties that are not presented in larger scale systems. There are several reasons why this is the case.

### 2.1.1 Surface Area to Volume Increases

When an object is scaled, the volume changes by the said scale cubed, and the surface area changes by that scale squared. This means that the surface area to volume ratio increases by the scaling factor as the system scales down. For example, if a catalyst of platinum spheres with a radius of 1mm is scaled down by a factor of 1 million, therefore becoming 1 nanometer radius spheres; this would increase the surface area to volume ratio by a factor of  $10^6$ . That means 1 million times less platinum would be required to achieve the same total surface area in the nano scale platinum than in its larger counterpart system. This represents a considerable resource savings.

As a great deal of interesting and relevant physics occurs at surface level, greatly increasing surface area can produce some very interesting results. An example provided by nature is the gecko's ability to stick to surfaces without the use of conventional adhesive. Electron microscope studies have shown that the feet of the gecko have millions of tiny hairs protruding from them creating greatly larger surface area than a simple smooth foot could have. This great increase in the surface area allows the gecko's feet to adhere to surfaces through Van der Waals bonding over this huge surface area [2.1].



### **2.1.2 Particle Size Approaching Characteristic Length Scales**

There are many useful physical characteristics of scales that emerge at the submicron scale. The size of the structures comes close to and below these characteristic lengths, the physics changes. A few examples of the difficulties inherent in studying systems at these scales are domain size, exchange length, mean free electron path coherence length and wavelength of visible light.

## **2.2 Magnetism in Nanoparticles**

### **2.2.1 Origins of Magnetic Domains**

To understand magnetism in a bulk sample of a magnetic material, several forces, and the mechanisms in which they find balance, need to be understood. First are the atomic origins of magnetism. The electrons in an atom can have both spin and orbital angular momentum. From the study of electricity and magnetism we know that a charge with angular momentum generates a magnetic field. This means that both the electron's spin and orbital angular momentum can produce magnetic fields at the atomic level. Studying the individual atom, we see that many have an equal number of up and down electron spins, and that their orbitals are configured in such a way as to have a total of zero angular momentum. This causes the net magnetic field produced to be zero. However, a large number of atoms on the periodic table do not produce this canceling effect and have a net magnetic field or magnetic moment. So, why does it seem like there are so few magnetic materials? The answer to this is exchange coupling. In a great number of magnetic materials, random thermal agitation or the specific coupling between atoms causes their magnetic moments to point in a way that cancels out the magnetic moments of the surrounding atoms. It is seen in some materials however, that the exchange coupling is such that the nearby atoms align their magnetic moment with each other creating a large net magnetic field. In these systems we might expect the entire material to spontaneously align all magnetic moments and become a completely saturated magnet, as each atom affects adjacent atoms throughout the system. Generally this is not seen because the magnetostatic energy is proportional to the total magnetic moments that have aligned. The magnetostatic energy is reduced by aligning the fields in a way that causes the stray fields produced to be minimized, and a balance is created between these two competing forces. Magnetostatic energy is given in equation 2.1.

$$E = \frac{1}{2} \mu_0 \int M \cdot H_{ms} d^3r \quad (2.1)$$

Where,  $E$  is the energy,  $M$  is the magnetization,  $H_{ms}$  is the demagnetizing field, and  $\mu_0$  is the permeability of free space. The ferromagnetic exchange force pushes each atomic magnetic moment to align with its neighbors, but the magnetostatic force compels them to align anti-parallel.

On the small scale, the exchange energy is much greater than the magnetostatic energy, but as the number of aligned moments increase, so does the magnetostatic energy increase until it is the dominant force. The result is that there is alignment between magnetic moments in small sections called domains, but the domains do not necessarily align with neighboring domains. There is also anisotropy energies which play a role in the size and shape of the domains formed. The domain size is determined by exactly how these forces balance.

## 2.2.2 Anisotropic Effect of Single Domain Particles

A single-domain particle is uniformly magnetized with all the spins aligned in the same direction. The magnetization can be reversed by spin rotation since there are no domain walls to move. This is the reason for the very high coercivity observed in small nanoparticles [2.2]. Magnetic single-domain nanoparticles possess another important property, the anisotropy energy, which refers to the preference of the magnetization to lie along particular directions (with respect to the crystallographic directions) within the nanoparticles. These directions minimize the magnetic energy and are called anisotropy directions or easy axes. The magnetic energy of a nanoparticle increases with the tilt angle between the magnetization vector and the easy directions, as shown in Fig 2.1.

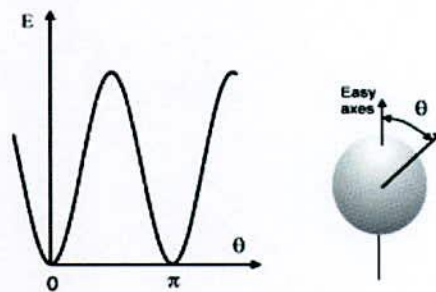


**Fig.2.1** Evolution of the magnetic energy with the tilt angle between the easy axis and the magnetization direction



The anisotropy energy, represented as the variation of the amplitude of this curve, is the product of the crystal volume times the anisotropy constant. The anisotropy energy is a function of the tilt angle and the following expression is commonly used:

$$E = KV \sin^2\theta \quad (2.2)$$

Where,  $K$  is the effective uniaxial magneto crystalline anisotropy constant per unit volume,  $\theta$  is the angle between the magnetization direction and the easy axis of the particle, and  $V$  is the volume of the particle. The anisotropy energy is dependent on several contributions, such as bulk magneto crystalline anisotropy, shape of the crystal, anisotropy constant, and dipolar interaction between neighboring nanoparticles [2.3].

### 2.2.3 Single Domain Limit

Domain wall movement is the primary mechanism through which the overall magnetization changes. As a result, as a bulk material is made smaller its coercivity increases due to the domains not being able to subdivide into as many smaller units. This trend continues until a critical size is reached. At this critical size the particle can only be single domain because the energy cost of forming a domain wall exceeds the reduction in magnetostatic energy. This is known as the single domain limit. For spherical particles this equation is:

$$R_{sd} = \frac{9E_\sigma}{\mu_0 M_s^2} \quad (2.3)$$

Where,  $M_s$  is the saturation magnetization and  $E_\sigma$  is the total domain wall energy, per unit area. It is near the single domain size limit that coercivity is at a maximum. There are no domain walls to assist with magnetization direction switching. As such, particles below this size must be single domain.

### 2.2.4 Magnetization Processes and Thermal Energy Effect

In the case of nanoparticles with an average diameter in the range of few tens of nanometers, the anisotropy energy becomes comparable with the thermal energy  $k_B T$ . According to Boltzmann distribution



$$f(\theta)d\theta = \frac{\exp\left(\frac{-E(\theta)}{k_B T}\right) \sin(\theta) d\theta}{\int_0^\pi \exp\left(\frac{-E(\theta)}{k_B T}\right) \sin(\theta) d\theta} \quad (2.4)$$

Where,  $k_B$  is the Boltzmann constant and  $T$  the absolute temperature. It is possible to calculate the probability  $f$  between angle  $\theta$  and  $\theta + d\theta$ . Two different situations can occur:

In the first case:  $k_B T \ll KV$ :  $f(\theta)$  is large around  $d\theta = 0$ . The magnetic moment is fixed along the easy direction of magnetization. This means that the thermal energy is not high enough to overcome the energy barrier  $KV$  that separates the two energetically equivalent easy directions of magnetization. Nanoparticles that exhibit this condition are called thermally blocked particles, and their magnetic moment is blocked along a specific crystallographic direction (easy axis).

In the second case:  $k_B T > KV$ : where the thermal energy, is high enough to move the magnetic moments away from the easy axis and the magnetization is easily flipped. In this situation the system behaves like a paramagnet, instead of atomic magnetic moments, there is now a giant (super) moment inside each nanoparticle. This phenomenon is called superparamagnetism, a term coined by Bean and Livingston [2.4].

### 2.2.5 Superparamagnetism

For superparamagnetic nanoparticles, the magnetization evolution with the external magnetic field is proportional to the Langevin function that takes into account the Boltzmann distribution of the energy level corresponding to the possible orientations of the particle magnetization moment. This function is commonly used to fit experimental magnetization curves of nanoparticles and to determine the size of the crystals and its specific magnetization. The characteristic features of superparamagnetic nanoparticles are their response to a magnetic field, where there are no coercivity field, no remanent magnetization and very high field saturation of the magnetization [2.3].

A typical feature of superparamagnetic nanoparticles is the Néel relaxation time,  $\tau_N$ , that is the time constant of the return to equilibrium of the magnetization after perturbation. It can be expressed as:

$$\tau_N = \tau_0 \left( \frac{KV}{k_B T} \right) \quad (2.5)$$

Where,  $\tau_0$  is the pre-exponential factor called characteristic relaxation time (dependent on anisotropy energy),  $k_B$  is the Boltzmann constant and  $T$  is the absolute temperature. This time is characteristic of the internal relaxation of the magnetization of nanoparticles. According to equation (2.5), the volume of nanoparticle and the temperature are two critical parameters affecting the Néel relaxation time and therefore the superparamagnetic or thermally blocked behavior of the system.

There is a size limit that divides the internal relaxation occurring in single domains in two different time regimes, slow and fast relaxation compared to a characteristic measurement time of the methods used to investigate the magnetic behavior of the system. The superparamagnetic nanoparticles relax rapidly and do not show any magnetic remanence or coercivity, while the thermally blocked single domains have longer relaxation time and show both remanent magnetization and coercivity [2.5].

A blocking volume  $V_B$  and a blocking temperature  $T_B$  can be defined in order to distinguish the superparamagnetic single domains from the thermally blocked ones:

$$V_B = \frac{K_B T}{K} \ln \left( \frac{t_{exp}}{\tau_0} \right) \quad (2.6)$$

$$T_B = \frac{KV}{K_B \ln \left( \frac{t_{exp}}{\tau_0} \right)} \quad (2.7)$$

Where,  $t_{exp}$  is the characteristic experiment time of the measuring technique being used. It is important to notice that the blocking limit is dependent of the experiment time, and it is possible to obtain different values of  $V_B$  and  $T_B$  for different techniques. For instance, vibrating sample magnetometer (VSM) has a characteristic measurement time of 10s, while superconducting quantum interference device (SQUID) has a measuring time of  $10^{-2}$  s and Mössbauer spectroscopy  $10^{-8}$  s [2.6].

When nanoparticles are suspended in a liquid, the Brownian motion of such nanoparticles plays an important role. This physical phenomenon occurs due to continuous collision between particles and the thermally activated liquid molecules, and the effects are more pronounced for small particles in the sub-micron range. The Brownian motion mechanism can be arbitrarily divided into a translational (linear) motion and a rotational motion. The linear movement can be measured by dynamic light scattering or photon correlation spectroscopy and can be described by the Stokes-Einstein equation [2.5]:

$$\tau_L = \frac{3\pi\eta D_H}{K_B T q^2} \quad (2.8)$$

Where,  $\eta$  is the viscosity of the liquid,  $D_H$  the hydrodynamic diameter of the particle and  $q$  is the light scattering wave number. The rotational motion can be described by a characteristic rotational diffusion time, according to:

$$\tau_B = \frac{\pi\eta D_H^3}{2K_B T} \quad (2.9)$$

It is possible to determine the rotational Brownian relaxation of magnetic nanoparticles through magnetic measurements of the frequency dependent complex susceptibility [2.7].

For magnetic nanoparticles suspended in a liquid, an effective relaxation time  $\tau_{eff}$  related to magnetic measurements can be defined as follow:

$$\frac{1}{\tau_{eff}} = \frac{1}{\tau_N} + \frac{1}{\tau_B} \quad (2.10)$$

Both the Néel and the Brownian relaxation processes are contributing to this effective time, while the translational motion time is neglected because it does not affect magnetic measurements. Fig.2.2 represents the different time constants related to the different relaxation mechanism for nanoparticle in suspension as a function of their radius.

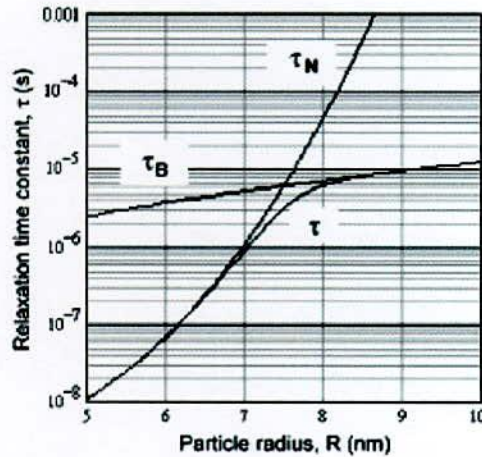


Fig.2.2 Time constant vs particles size for magnetite particles



The plot illustrated in Fig.2.2 is given for magnetite nanoparticles at room temperature. The blocking radius is estimated as  $\sim 7$  nm [2.8]. There are two ways to measure the relaxation phenomena: either in the time domain or in the frequency domain. By measuring the complex susceptibility it is therefore possible to determine the Brownian relaxation time and the mean hydrodynamic volume of the nanoparticles.

### 2.2.6 Superparamagnetic Limit

As the particle size continues to decrease the coercivity also declines. This is due to the fact that there are physically fewer spins in the particle that need to be rotated, thereby requiring less energy. As the decrease continues, the energy required to switch the particle magnetic moment approaches the ambient thermal energy. This causes the particle to randomly and spontaneously switch magnetization orientation as a result of ambient thermal fluctuations. The particle effectively has zero coercivity. This is known as superparamagnetism as it closely resembles paramagnetism, however the fluctuations are of a “super spin” type instead of the single atomic spins found in paramagnetism. Neel derived that the particles approach equilibrium with a characteristic relaxation time given by:

$$\frac{1}{\tau} = f_0 e^{\frac{-K_U v}{k_B T}} \quad (2.11)$$

Where  $\tau$  is the relaxation time,  $f_0$  is frequency factor ( $10^9 \text{sec}^{-1}$ ),  $K_U$  is the anisotropy constant,  $v$  is particle volume,  $k_B$  is the Boltzmann’s constant, and  $T$  is absolute temperature [2.9]. This progression from large to small is graphically depicted in Fig.2.3. In this figure MD means multi domain, SD, single domain, PSD pseudo single domain,  $d_0$  is the diameter below which particles must be single domain,  $d_s$  is the diameter below which the particle is superparamagnetic at room temperature. Since blocking temperature is an exponential, we can define it for a given time and particle volume, where that time is equal to  $\tau$ . We could also use a given temperature and time to define a blocking volume or a critical radius for superparamagnetism. It is important to note that no definition of superparamagnetic (SPM) limit size can be defined without choosing a time scale.

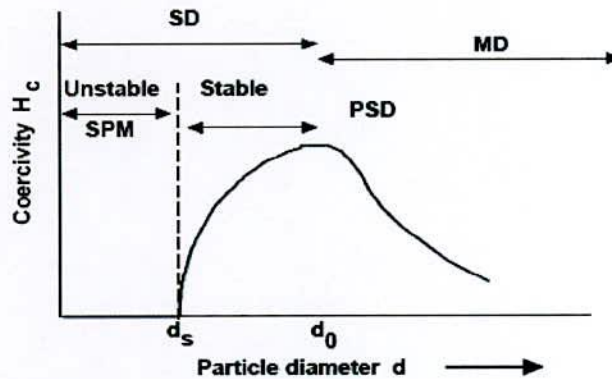


**Fig.2.3** particle sizes vs. coercivity showing onset of superparamagnetism

The property of superparamagnetism is achievable at room temperature in nanoparticle systems with diameters in the range of 10 to 100 nm, for relaxation times on the order of milliseconds. This is highly attainable in laboratory settings and the ability to produce a system with zero coercivity has many possible applications. However, in some cases the superparamagnetic limit represents a difficulty, as in making hard drives. As the size of a bit stored on the surface of a magnetic material gets smaller, the superparamagnetic limit is approached. If the bit has no coercivity, then its direction of magnetization flips randomly and with no external energy input. This makes it unsuitable for data storage.

The difference in  $M-H$  curves between ferromagnetic and superparamagnetic particles can be seen in Fig.2.4 below, whereby the influence of particle size on magnetization is evident.

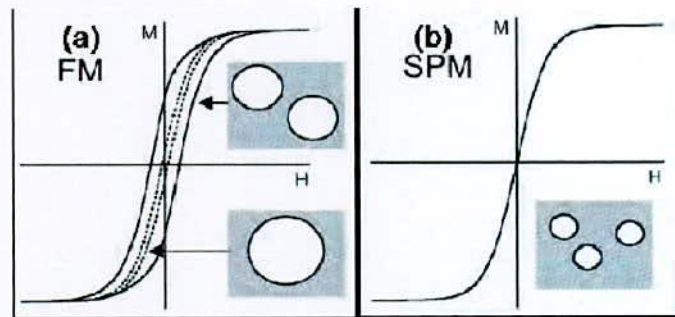


**Fig.2.4** Comparison of the  $M-H$  curves of (a) ferromagnetic and (b) superparamagnetic particles. Adapted from Pankhurst et al.[2.10].

## 2.3. Basic Concept of Nanoparticles Synthesis

### 2.3.1 Nucleation and Growth

The common feature of the solution-based approaches is the precipitation of solid products from homogeneous solutions. Precipitation of solid particles is a dynamic process involving three stages: nucleation, growth, and coarsening/aggregation [2.11].

According to LaMer and Dinegar, who firstly described the theory behind the formation of mono dispersed sulfur colloids from sodium thiosulfate and hydrochloric acid, uniformly sized and shaped particles are obtained only when the nucleation and growth processes are completely separated. They proposed a diagram showing the variation of the solute concentration in time where three regions, corresponding to the pre-nucleation, nucleation and growth processes, can be easily identified (Fig.2.5) [2.12-2.13]. The pre-nucleation process (region I) is characterized by a relatively sharp increase of the solute (monomer) concentration as the chemical reaction progresses.

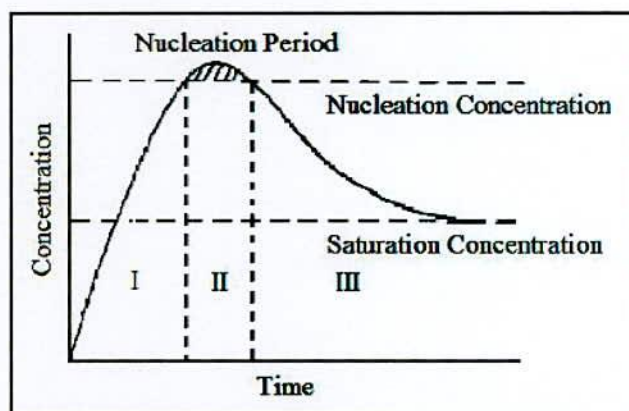


Fig.2.5 LaMer's diagram describing the formation mechanism for monodisperse colloidal particles



At a critical value of the solute concentration (“nucleation concentration”) corresponding to a certain level of the super-saturation, a transition from the homogeneous to heterogeneous state occurs as a result of the onset of the nucleation process. The solute concentration continues to increase with time during the “nucleation period” (region II), but is shortly followed by a rapid decrease due to an intensive colloid nucleation. Once the solute concentration approaches the “nucleation concentration” again, the nuclei are no longer produced in the system because the super-saturation level is now too low to further sustain the nucleation process. The existing nuclei enlarge by migration of the monomer species from the slightly supersaturated solution toward their surfaces, thereby causing a further decrease of the concentration (region III). The growth process occurs until the monomer concentration reaches the “saturation concentration”. According to the LaMer diagram, the shape of the concentration–time curve suggests that the precipitation takes place through a fast nucleation process followed by a slower diffusional growth eventually leading to the formation of monodisperse colloidal particles. The free energy associated with the formation of a nucleus by the aggregation of the solute species (monomers) in the supersaturated solution is given by the following equation:

$$\Delta G = -\left(\frac{V}{\Omega}\right) K_B T \ln \beta + S \gamma \quad (2.12)$$

Where, V is the volume of the nucleus, S represents its surface area,  $\Omega$  stands for the volume of a monomer molecule contained in the nucleus,  $\beta$  denotes the saturation ratio and  $\gamma$  is the normalized surface free energy. Particularly, for spherically-shaped nuclei with  $V = \frac{4\pi r^3}{3}$  and  $S = 4\pi r^2$ , the free energy can be expressed as:

$$\Delta G(r) = -\left(\frac{4\pi r^3}{3\Omega}\right) K_B T \ln \beta + 4\pi r^2 \gamma \quad (2.13)$$

Its sign is principally determined by the value of the saturation ratio ( $\beta$ ). Thus, when  $\beta < 1.0$  (the solution is not enough supersaturated to induce the nucleation), the free energy,  $\Delta G(r)$ , takes positive values and the nucleation processes do not occur spontaneously. Conversely, when  $\beta > 1.0$ , the free energy reaches a maximum,  $\Delta G^*(r)$ , corresponding to a certain value of the nuclear radius,  $r^* = \frac{2\Omega\gamma}{K_B T \ln \beta}$ , which is calculated by considering  $\frac{d(\Delta G)}{dr} = 0$ . Therefore, all the nuclei having a radius smaller than  $r^*$  are energetically unstable and shrink until they completely dissolve, whereas

those with  $r$  higher than  $r^*$  continue to enlarge and become more stable since their energy decreases with increasing the size [2.14-2.15].

### 2.3.2 Aggregation Phenomena

Such a growth mechanism by which small-sized particles called “primary particles” cluster into intermediate shapeless aggregates to produce well-defined, nearly monodisperse “secondary particles” is referred as aggregation (coalescence) [2.16]. In many cases, formation of nano structured materials involves a single aggregation step by which the primary particles resulted from the nucleation and diffusional growth processes tend to minimize their surface free energy by clustering and coalescence into larger, more stable structural entities [2.17 - 2.18].

However, as Zheng *et al.* have recently demonstrated for nanocrystalline  $\alpha$ - $\text{Fe}_2\text{O}_3$  prepared solvothermally, the growth mechanism can occur through more than one aggregation step. A close examination of the TEM micrographs corresponding to the iron oxide samples collected at different reaction times revealed that the small 5 - 8 nm-sized crystals cluster together to give larger particles with sizes ranging between 15 and 30 nm. The resulting nanoparticles act as building blocks for the subsequent growth of the 40 - 50 nm irregularly-shaped aggregates. Each of these single crystalline entities undergoes a coarsening (Ostwald ripening) process leading to the formation of highly faceted  $\alpha$ - $\text{Fe}_2\text{O}_3$  particles with a relatively narrow size distribution [2.19].

The secondary particles resulting by the clustering and coalescence of two or more primary nano crystallites can be either mono crystalline or polycrystalline in nature, depending on the arrangement of the smaller units within each larger structural entity [2.17]. Polycrystalline secondary structures have been obtained when the nanosized primary particles aggregate in a random manner. The random clustering of the nanocrystalline units can also yield mono crystalline secondary particles when the aggregation is followed by an internal recrystallization process.

However, mono crystalline particles are commonly obtained by the oriented attachment of the primary nano crystallites which necessitates a continuity of the crystal lattices of the neighboring particles through each shared interface [2.20 - 2.21]. In such a case, a perfect alignment of the lattice fringes over the whole assembly can be easily identified by examining the HRTEM micrographs. The formation of



secondary particles through the oriented attachment mechanism is often accompanied by the formation of various packing defects including dislocations, twins, phase boundaries and stacking faults [2.22 - 2.24]. In some cases, both the aggregation and the Ostwald ripening processes contribute to the formation of nanocrystalline ferrite particles [2.25].

## **2.4 Synthesis Methods of the Nanocrystalline Ferrites**

Bulk ferrites have been traditionally prepared by solid state reactions consisting in a succession of heat treatments intermediate regrinding of stoichiometric mixtures of powdered precursors. Although this conventional “shake and bake” route is cheap and easily scalable, the slow rate of diffusional processes necessitates prolonged annealing at relatively high temperatures resulting in a very limited control over the morphology of the reaction products.

Translation of the dimensions of ferrites to the nanometer scale can be achieved through a wide variety of methods, both physical and chemical. The physical methods are “top-down” strategies in which high purity powders of bulk precursor materials are transformed into nanocrystalline ferrites by a mechanical, mechano-chemical or laser assisted process. Although they are simple, inexpensive and easily scalable, physical methods present limited control over the morphology and /or chemical composition of the final products. Conversely, solution-based chemical methods are “bottom-up” approaches where nanoparticles are produced via chemical reactions between sub-nanometer reactive species, such as atoms or molecules. Depending on the nature of the solvent used, solution-based chemical methods are classified into two main categories: aqueous solution-based techniques and non-aqueous techniques.

### **2.4.1 Preparation of Nanostructured Ferrites by Physical Methods**

Physical methods employing the high-energy ball milling technique are wide spread used in the preparation of nano structured ferrite materials. These methods can be generally classified into three categories: mechanical activation, mechano-chemical synthesis (mechano synthesis) and mechanical alloying. Mechanical activation refers to the grinding of bulk ferrite material in planetary ball mills until the grain size reaches the nanometer scale. The bulk ferrites used as precursor materials in



the ball-milling process were obtained by a conventional thermal (ceramic) method from mixtures of a divalent metal oxide ( $MO$ ,  $M^{2+} = Mg^{2+}, Mn^{2+}, Ni^{2+}, Zn^{2+}$ ) and  $\alpha$ - $Fe_2O_3$ .

In general, one of the short comings of the physical methods is related to the limited number of parameters which can be varied in order to achieve a better control over the morphology of the resulting nano powders. In the mechanical activation process, the average grain size of the ferrite powders could be tuned by varying the milling time. Chinnasamy *et al.* showed that the average grain size of the  $NiFe_2O_4$  powders, determined from X-ray diffraction measurements, decreases from 60 nm to 10 nm as the milling time increases from 1h to 30h [2.26]. Mahmoud *et al.* observed a similar behavior for  $MnFe_2O_4$  powders prepared by mechanical activation. Increasing the milling time from 10 min to 3 h decreased the particle size from 200 nm to 82 nm. A close examination of the TEM micrograph revealed a relatively small number of individual, roughly spherical nanoparticles as well as a large number of aggregates. The aggregated appearance of the  $MnFe_2O_4$  nanoparticles made difficult the accurate determination of the average particle size from electron microscopy measurements [2.27].

The high-energy ball milling process induces the diffusion of the divalent ( $M^{2+}$ ) and trivalent ( $Fe^{3+}$ ) metal ions between the two sublattices of the spinel structure, which results in a change of the inversion parameter ( $\gamma$ ) of the obtained nano powders as compared with the bulk material. It was also observed that the inversion parameter varies differently with the particle size depending on the type of spinel structure adopted by the bulk ferrites. For instance, the inversion parameter of the mixed spinel  $MnFe_2O_4$  increases from 0.23 (corresponding to the bulk material) to 0.45 (for 82 nm - sized particles) [2.27].

In addition to the morphological changes, the structural modifications undergone by the bulk ferrites during mechanical activation process were found to have a significant effect on the magnetic properties of the resulting nano structured ferrites. The mechanically activated ferrite nano powders have been the subject of intense studies aiming at understanding the relationship between the crystal structure of nanosized ferrites and the observed magnetic properties. The slight contraction of the unit cell observed in some of the mechanically activated ferrites causes distortions

of the cation (B) - anion (A) – cation (B) bond angle, which in turn affect the strength of the interaction between the magnetic ions occupying the octahedral (B) interstices.

In spinel crystals, the inter sublattice (A-O-B) exchange interactions are stronger than the intra sublattice (A-O-A and B-O-B) interactions [2.28]. The spins of the magnetic ions located in the tetrahedral interstices (A) are coupled anti-ferromagnetically with those of the cations residing in the octahedral sites (B). The antiparallel coupling of the metal ions is mediated, in the case of metal oxides, by the diamagnetic  $O^{2-}$  ion which contains paired electrons in each of its 2p orbital's. The exchange interaction between metal ions having unpaired 3d electrons is strong when the B-O-B bond angle approaches  $180^\circ$ . For the inter sublattice A-O-B exchange interactions (or super exchange interaction) the bond angle is  $126^\circ$ , whereas for the intra sublattice A-O-A and B-O-B exchange interactions the bond angles are  $79^\circ$  and  $90^\circ$ , respectively [2.29]. The magnetic ions occupying the same type of interstitial sites are characterized by a parallel alignment of their spins which results in a weaker ferromagnetic coupling [2.30].

Similar to the mechano-chemical synthesis, the mechanical alloying process employs the high-energy ball milling technique to prepare nanocrystalline ferrites both by fracturing the large particles of the precursor materials and promoting the solid state reactions between the resulting nanosized powders. Mixtures of metal hydroxides or mixed metal oxides with spinel structure are usually used as precursor materials to prepared nano sized ferrites by mechanical alloying [2.31].

Other physical methods used to produce nano sized ferrite powders include pulse laser ablation (for mixtures of iron oxides with sizes ranging from 30 -100 nm) [2.32], radio frequency plasma torch synthesis (for 20 nm and 26 nm Ni-substituted  $Fe_3O_4$  and 18 nm  $NiFe_2O_4$ ) [2.33],  $CO_2$  laser pyrolysis (for 5 nm-sized  $\gamma-Fe_2O_3$ ) [2.34] and  $\gamma$ -ray radiation (for 14 nm sized  $Fe_3O_4$ ) [2.35].

#### **2.4.2 Preparation of Nanocrystalline Ferrites by Wet Chemical Methods**

Although the physical methods are simple and versatile, enabling the preparation of a wide variety of ferrite nano-powders in large quantities and with a relatively low cost, their reliability is often questionable due to the contamination of



the products (especially in the mechanical milling processes) and the limited control of the morphology of the resulting nanosized materials. The wet chemical synthetic routes have proven to be much more advantageous for the preparation of transition metal ferrites than the physical methods since they provide a better control over the size, size distribution, shape, and degree of agglomeration of the resulting nanocrystals. These characteristics, along with the chemical composition were found to influence significantly the magnetic properties of the ferrite nanoparticles and therefore, their potential application in high-density magnetic storage media [2.36], magnetic resonance imaging [2.37], magnetic refrigeration [2.38] magneto-optical devices [2.39], and ferrofluids [2.40]. The use of nano phase ferrites in certain biological and biomedical areas requires them to possess not only uniform sizes (usually smaller than 20nm), shapes, and high values of the saturation magnetization, but also individual coatings with bio-compatible molecules [2.41 - 2.43]. The solution-based chemical methods produce nano structured transition metal ferrites with relatively good crystallinity even though they are, usually, low-temperature synthetic approaches. Moreover, a limited number of synthetic routes do afford large-scale preparations of high quality ferrite nanocrystals without a significant alteration of the morphology and properties of the resulting materials. However, the great disadvantages of the chemical methods lie in the fact that some of them use highly toxic reagents as metal precursors and necessitate a rigorous control over the reaction parameters in order to obtain nanocrystalline ferrites with the desired morphology. In addition, most of the chemical methods use large amounts of capping ligands and surfactants rendering the resulting ferrite nanocrystals soluble in non-polar media. This imposes some restrictions on the use of the ferrite nanocrystals in certain biological systems which require solubility in aqueous media. Several solution-based approaches, both in aqueous and non-aqueous media, have been reported for the preparation of nanocrystalline ferrites particles; they include co-precipitation, micro emulsion, sol-gel, hydrothermal or solvothermal and sonochemical methods.

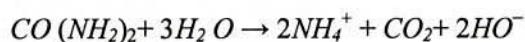
#### **2.4.2.1 Synthesis of Nanocrystalline Ferrites in Aqueous Solutions**

##### **2.4.2.1.1 The Co-precipitation Method**

Co-precipitation of nanocrystalline ferrites from aqueous homogeneous solutions is one of the most popular liquid phase synthetic approaches due to its



simplicity, low cost and versatility. Transition metal ferrite nanoparticles with a wide variety of compositions ranging from ternary metal oxides [ 2.44 - 2.45] ( $AFe_2O_4$ ,  $A^{2+} = Mn^{2+}, Fe^{2+}, Co^{2+}, Cu^{2+}, Zn^{2+}$ ) to mixed metal oxides containing two [2.46] [ $A_xB_{1-x}Fe_2O_4$ ,  $A^{2+} = Co^{2+}$ ,  $B^{2+} = Ni^{2+}$ ] or three [2.47] [ $A_xB_yC_{1-x-y}Fe_2O_4$ ,  $A_{2+} = Ni_{2+}$ ,  $B^{2+} = Cu^{2+}$ ,  $C^{2+} = Zn^{2+}$ ] different divalent metal ions have been prepared by using the co-precipitation technique. In a typical co-precipitation process, aqueous solutions containing divalent metal precursors, such as acetates, chlorides, nitrates or sulphates, and an iron (III) salt are treated with a precipitating agent [2.47 - 2.48]. Alternatively, the synthesis can be performed by replacing the ferric precursor with a ferrous salt, but in this case the partial oxidation of the iron (II) compound is required. In addition to alkaline hydroxides (NaOH, KOH) and ammonia solutions another commonly used precipitant is urea [2.49]. This organic compound undergoes a hydrolysis reaction [2.50] when heated at temperatures higher than 60°C with the formation of hydroxide ions (HO<sup>-</sup>):



The nature of the precipitating agent was found to influence significantly the morphology of the ferrite nano powders synthesized by the co-precipitation method. For example, Ryu and coworkers reported the preparation of nanophase  $Co_{1-x}Ni_xFe_2O_4$  ( $0 < x < 1$ ) and compared the morphology of the particles obtained in the presence of two different precipitating agents, that is, NaOH and  $NH_4OH$ , respectively [2.46]. When the precipitation is performed with NaOH the resulting particles possess a relatively good crystallinity, their sizes vary between 15 and 25 nm, depending on the Co / Ni ratio and have a needle-like aspect, except for the first term of the series ( $x = 0$ ), where the particles are spherical. This is not the case of the nano powders precipitated in the presence of  $NH_4OH$ , when the particles are found to be less crystalline and their sizes range from 2 to 10 nm. However, regardless of the morphology of the as-prepared nano powders, the nano structured ferrite materials resulting from their heat treatment at 600°C consist of agglomerated particles with an average size of 30 nm. The morphological changes of the as-prepared nano powders during the annealing process were found to depend on their initial composition. Thus, while in the alkaline medium the transition metal ions precipitate as hydroxides, in the presence of an ammonia solution the co-precipitation occurs with the formation of transition metal complexes incorporating the  $NH_4^+$  ions.

The temperature is one of the most important parameters in the co-precipitation process. When the metal ions are precipitated at room temperature, amorphous intermediate compounds such as hydroxides or oxyhydroxides separate from the reaction solution. In such a case, a subsequent heat treatment of the hydroxo-intermediates is required in order to obtain the corresponding nanocrystalline ferrite materials [2.47]. Chen *et al.* prepared nanosized  $\text{MnFe}_2\text{O}_4$  particles by mixing stoichiometric amounts of Mn (II) and Fe (III) chlorides with NaOH at room temperature followed by the digestion of the resulting precipitate at 100 °C. In addition to promoting the dehydration of the metal hydroxide intermediates and the crystallization of the nanophase  $\text{MnFe}_2\text{O}_4$ , the thermal treatment was found to strongly influence the size of the ferrite nanoparticles [2.51].

However, if the co-precipitation reaction takes place in boiling solutions containing the metal precursors and the precipitating agent, the hydroxo-intermediates formed at elevated temperature are immediately converted into nanocrystalline ferrites [2.44]. For instance, Sousa and coworkers prepared a series of nano sized transition metal ferrites [ $\text{MFe}_2\text{O}_4$ ,  $\text{M}^{2+} = \text{Ni}^{2+}, \text{Cu}^{2+}, \text{Zn}^{2+}$ ] by precipitating the metal ions in alkaline media at 100 °C. As demonstrated by the XRD measurements, the isolated solid products were found to be single-phase mixed metal oxides with spinel structure and good crystallinity [2.45].

Unlike the other transition metal ferrites,  $\text{Fe}_3\text{O}_4$  can be obtained as an oxide even at room temperature. Kang *et al.* reported the synthesis of 8.5 nm-sized  $\text{Fe}_3\text{O}_4$  particles by room temperature co-precipitation of a 1:2 molar mixture of Fe (II) and Fe (III) precursors with a solution of NaOH. The resulting black solid was treated with a diluted solution of HCl and then dispersed in water to form an aqueous colloid. The positive charges built up at the surface of the  $\text{Fe}_3\text{O}_4$  nanocrystals upon acidification induce electrostatic repulsions between neighboring particles thereby stabilizing the colloidal dispersion against aggregation. The TEM investigation of the aqueous colloid revealed that the  $\text{Fe}_2\text{O}_4$  nanoparticles are uniformly sized and shaped and they assemble in to mono layers [2.39]

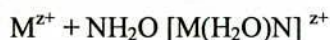
#### **2.4.2.1.2 The Sol-Gel Method**

Nanocrystalline ferrites have also been synthesized by the sol-gel method [2.52 -2.54], a synthetic route widely used for the preparation of various types of ceramic materials as well as glasses [2.55] and catalysts [2.56]. The sol-gel technique

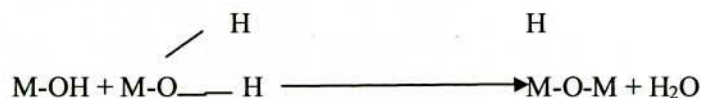


is a multi-step synthetic route in which a precursor dissolved in a suitable solvent is converted into the corresponding crystalline oxide through a succession of chemical and physical processes [2.57]. The precursor materials generally used in the sol-gel approach are the metal / metalloid alkoxides and the metal salts. For example, various silicon alkoxide precursors, such as tetra-alkoxysilanes [Si(OR)<sub>4</sub>, R = CH<sub>3</sub>, C<sub>2</sub>H<sub>5</sub>, n-C<sub>3</sub>H<sub>7</sub>, n-C<sub>4</sub>H<sub>9</sub>, OCH<sub>2</sub>CH<sub>2</sub>OCH<sub>3</sub>], organo alkoxysilanes [R'<sub>x</sub>Si(OR)<sub>4-x</sub>], x = 1-3 and R' is an organic radical unreactive towards hydrolysis) and alkoxysiloxanes (oligomeric compounds consisting of 1 to 8 silicon atoms) have been employed in the sol-gel preparation of silicon-based compounds including silica (SiO<sub>2</sub>), silicones, and silicate gels, respectively [2.58].

Regardless of the nature of the oxide product, two types of chemical reactions are usually involved in the sol-gel technique: the hydrolysis of the metal / metalloid precursor and the condensation of the resulting intermediates [2.57]. Hydrolysis and condensation are complex reactions occurring either concurrently or separately in the course of the sol-gel process and being closely dependent on the nature of the precursor. As an example, when metal salts are used as precursors, the hydrolysis reaction involves solvated cations generated in aqueous solutions by the electron transfer from the water molecules to the metal ions: [2.58]



Once formed in the aqueous solution, these intermediates undergo subsequent condensation reactions eventually leading to the formation of metal oxide products. However, the mechanistic path ways through which the intermediates are transformed into the final product are substantially different, being primarily determined by the nature of the groups coordinated to the metal ions. Thus, when hydroxo-aquo species are involved in the condensation process, hydroxo bridges are created between the M<sup>z+</sup> cations. Such a condensation reaction is called oblation and proceeds through a nucleophilic substitution (SN) mechanism with elimination of a water molecule [2.58].

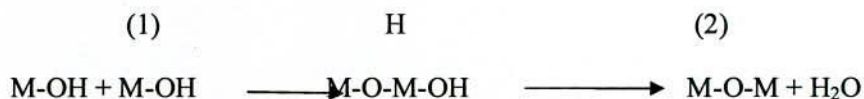


Conversely, when the condensation reaction takes place in the presence of oxo-hydroxo intermediates, oxo bridges are created between the M<sup>z+</sup> cations. Such a



reaction refers to as oxolation and can proceed either through a nucleophilic addition (AN) or through anucleophilic substitution (SN), depending on the saturation of the coordination sphere of the  $M^{z+}$  cations. For the  $M^{z+}$  cations with unsaturated coordination spheres, the oxolation reaction between the corresponding oxo-hydroxo intermediates takes place through a nucleophilic addition mechanism [2.58].

If the coordination sphere of the  $M^{z+}$  cations is saturated, the oxolation reaction takes place through a nucleophilic substitution mechanism. In such a case, the oxo-hydroxospecies undergo a condensation reaction which is usually described as a two-step process consisting of a nucleophilic addition and a  $\beta$ -elimination. The hydroxo-bridged intermediate formed by the nucleophilic addition loses a water molecule to give a compound in which the  $M^{z+}$  cations are linked by an oxo bridge:[2.58]



In general, the sol-gel processing involves several successive stages: (a) the formation of a sol which represents a colloidal suspension containing small particles with a diameter less than 1000 nm dispersed in a continuous liquid medium; (b) the gelation of the sol to give a three-dimensional M-O-M / M-OH-M network whose pores are filled with solvent molecules (wet gel); (c) the aging of the resulting wet gel, process known as synthesis; (d) the elimination of the solvent from the gel pores (drying) and (e) the calcination of the resulting porous gels with the formation of metal oxide ceramic materials(densification) [2.57-2.58].

Transition metal ferrite nano powders were typically obtained by calcining the amorphous gels resulting from the hydrolysis of metal salts (acetates, nitrates) dissolved in different solvent mixtures. It is worth noting that, in all cases, the temperature effect on the magnetic properties of the nanocrystalline ferrites shows a similar trend regardless of their chemical composition. Specifically, the saturation magnetization ( $M_s$ ) of the ferrite powders increases with increasing the calcination temperature, where as the coercivity ( $H_c$ ) increases to reach a maximum and then drops abruptly. Such a variation of the magnetic properties of the nanophase ferrites is dependent on the particle size which was found to increase with the calcination temperature [2.52-2.53].

### 2.4.2.1.3 The Hydrothermal / Solvothermal Method

Aqueous solution-based synthetic strategies have been extensively used for the preparation of nanophase ferrites by virtue of their simplicity, low cost and versatility. However, due to the low boiling point of water (b.p = 100°C at 1 atm) the chemical reactions in aqueous medium usually take place at low temperatures, thus leading to nano structured metal oxides with a relatively poor crystallinity. Due to the mild reaction conditions, a subsequent annealing step is often required to convert the as-prepared powders into highly crystalline nanophase ferrites. Although the grain size and the crystallinity of the as-prepared nano powders can be significantly improved during the post-synthesis heat treatment, in most of the cases the resulting particles have a wide size distribution, irregular shapes and a high degree of agglomeration.

An effective approach to obtain highly crystalline ferrites from aqueous solutions, eliminating the annealing step, consists of heating the reaction mixture in a sealed container at moderate temperatures. In such conditions, a high pressure is built up inside the bomb-type reactor, thereby increasing the temperature of the solution high enough to promote the chemical reactions between the precursors and to produce ferrite powders with good crystallinity. As the pressure inside the reaction vessel increases, significant changes on the physical properties of the solvent are observed over a wide temperature interval. Thus, the polarity and density of the water decrease, whereas its temperature increases rapidly to reach values much higher than the boiling point. Additionally, its solvent properties are greatly enhanced, thereby enabling the complete dissolution of various compounds, both organic and inorganic, which otherwise have a sparse solubility in aqueous media. Finally, when the temperature and pressure attain the so-called "critical values" ( $T_C = 374^\circ\text{C}$ ,  $P_C = 218 \text{ atm}$ ), the dissimilarities between the gaseous and liquid phases disappear completely and a new phase known as supercritical water is formed. In the supercritical state, water combines the individual characteristics of the liquid and gas phases making it very attractive as reaction medium for various chemical reactions [2.59].

However, such a behavior is not restricted only to water; other many non-aqueous solvents can serve as reaction media under similar conditions. Thus, when the chemical reactions take place in aqueous solutions the process is known as hydrothermal, whereas for non-aqueous solvents the technique is called solvothermal [2.60].



Under such extreme conditions, chemical reactions can occur in both sub-critical and super-critical regime, thereby resulting into highly crystalline single-phase products which do not necessitate post-synthesis annealing. However, although the hydrothermal /solvothetical process is a one-pot, highly efficient “green-chemistry” preparative route for various ferrite materials, it allows only for a limited control of the nucleation and growth processes usually yielding particles with irregular shapes, relatively large sizes and a wide size distribution [2.61].

#### 2.4.2.1.4 The Microemulsion Method

The microemulsion technique has proven to be a viable synthetic route for the preparation of a wide range of nano structured inorganic materials. In particular, this synthetic approach has been extensively used for the synthesis of spinel-type ferrites containing one  $[MFe_2O_4]$ , where  $M^{2+} = Mn^{2+}, Fe^{2+}, Co^{2+}, Ni^{2+}$  [2.62 - 2.64] or more  $[M'_xM_{1-x}Fe_2O_4]$ , where  $M'^{2+} = Mn^{2+}, Ni^{2+}$  and  $M^{2+} = Zn^{2+}$  [2.65 - 2.66] divalent metal cations. Micro-emulsions are colloidal systems in which one of the two mutually insoluble liquids is dispersed as fine droplets (with a size typically less than 100nm) in a second continuous liquid phase.

The two liquids are commonly referred to as the “aqueous phase”, that is an aqueous solution containing transition metal salts:  $[M^{2+}]/[Fe^{3+}] = 1:2$ ,  $[M^{2+}]/[Fe^{2+}] = 1:2$  and  $[M'^{2+}]/[M^{2+}]/[Fe^{2+}] = 1:1:4$  [2.62-2.63] or a precipitating agent (tetramethyl ammonium hydroxide-  $(CH_3)_4NOH$ , ammonium hydroxide-  $NH_4OH$ , sodium hydroxide-  $NaOH$  and methyl amine-  $[CH_3NH_3OH]$  [2.62 - 2.65], and the “oil phase”, represented by an organic solvent immiscible with water.

However, because of the high interfacial tension between the two mutually insoluble liquids, such heterogeneous systems are labile with respect to separation and surface active agents (surfactants) are often required to stabilize the micro-emulsion. Surfactants are amphiphilic organic molecules containing a polar (hydrophilic) group attached to a non-polar hydrocarbon (lipophilic) chain [2.67].

Depending on the charge of the hydrophilic group, the surfactants can be classified into three main categories: ionic (anionic or cationic), non-ionic (neutral), and amphoteric (possess both positively and negatively charged moieties), respectively. The hydrophobic part of the surfactant molecule usually consists of one



or more aliphatic chains, aromatic rings or combinations of them where the number of carbon atoms typically varies between 10 and 20 [2.68].

When a certain amount of surfactant is added to a mixture of two immiscible concentration at which the micelles form in the heterogeneous system is referred to as “critical micellar concentration” [2.67]. Micelles are categorized in two types that are “normal” and “reverse”, depending on the nature of the liquid phase contained in their cores. For example, in the normal micellar solutions (oil-in-water) the surfactant stabilized nano droplets of a non-polar liquid (oil phase) are dispersed in a continuous polar medium (aqueous phase). In this case, the surfactant molecules will have the hydrophilic functional groups (heads) oriented to the continuous aqueous phase, where as the hydrophobic chains (tails) will point to the non-polar liquid confined in the micellar core.

In many cases, the chemical reactions are performed at room temperature and the isolated solid products consist of mixtures of metal hydroxides /oxyhydroxides with a poor crystallinity. In these conditions, a post-synthesis annealing is often necessary to convert them into crystalline mixed metal oxides. However, this would be detrimental for the ferrite nano powders since it results not only in complex structural changes like the cation redistribution, but also in morphological transformations such as aggregation of the nanoparticles [2.63 - 2.65] or increase in the grain size [2.69]. Such side effects can be decreased upon elimination of the post-synthesis heat treatment. This is possible if the microemulsion-based syntheses are carried out at moderate temperatures (45-95°C) when the as-prepared ferrites nano powders possess a relatively good crystallinity and a supplementary heat treatment is not longer necessary [2.66].

Pileni and coworkers applied the oil-in-water microemulsion technique to the preparation of various nanocrystalline transition metal ferrites. In these syntheses, the nanophase ferrites were precipitated by introducing a controlled amount of methylamine into a normal micellar solution containing transition metal dodecyl sulfates. Interestingly, these metal compounds act both as metal sources for the synthesis of nano structured ferrites and as surfactants for the formation of the normal micellar systems. The metal dodecyl sulfates were prepared prior to the synthesis by reacting divalent metal salts, typically chlorides and acetates, with sodium dodecyl sulfate (NaDS). The experiments were usually carried out in air in order to promote

the oxidation of the  $\text{Fe}^{2+}$  ions to  $\text{Fe}^{3+}$  ions necessary in the synthesis of the ferrite materials [2.64].

The investigation of the formation mechanism of the nanophase magnetite revealed that two parameters influence the size of the resulting nanoparticles, i.e., the reaction temperature and the concentration of the iron (II) dodecyl sulfate [ $\text{Fe}(\text{DS})_2$ ]. TEM measurements showed that by changing the iron (II) dodecyl sulfate concentration from  $2.5 \times 10^{-3} \text{ M}$  to  $10^{-2} \text{ M}$  the particle size increased from 3.7 nm to 7 nm when the reaction was performed at room temperature. Likewise, by varying the reaction temperature from  $25^\circ\text{C}$  to  $80^\circ\text{C}$  and keeping constant the concentration of the iron (II) dodecyl sulfate at  $2.5 \times 10^{-3} \text{ M}$ , the dimensions of the particles increased from 3.7 nm to 6.6 nm. The largest magnetite particles (11.6 nm) were obtained for the highest values of both the  $\text{Fe}(\text{DS})_2$  concentration ( $10^{-2} \text{ M}$ ) and the reaction temperature ( $80^\circ\text{C}$ ). The authors assumed that the variation of the nanoparticle size is dictated by the fraction of the  $\text{Fe}^{2+}$  ions being oxidized to the  $\text{Fe}^{3+}$  ions rather than the modification of the morphology of the normal micelles. Their hypothesis was supported by a series of small angle X-ray spectroscopy (SAXS) measurements which indicated that neither the surfactant concentration nor the reaction temperature affected the dimensions of the normal micelles. When either of these parameters is increased, a larger amount of oxygen is dissolved in the normal micellar solution which induces the oxidation of a higher proportion of the  $\text{Fe}^{2+}$  ions and, eventually, the enlargement of the magnetite particles [2.64].

Vestal *et al.* performed a comparative study on the properties of the nanocrystalline  $\text{CoCrFeO}_4$  synthesized by using both the oil-in-water and water-in-oil microemulsion techniques [2.70]. Although the resulting ferrite particles were quite different in size, their shape, relative size distributions as well as the trends in the variations of the magnetic properties showed similarities regardless of the nature of the micellar solution used in the synthesis. Thus, while  $\text{CoCrFeO}_4$  particles synthesized from normal micellar solutions possess a size which ranges from 8 nm to 16 nm depending on the reaction temperature, the average diameters of the nanocrystals obtained by the reverse micelle technique can be varied between 6 nm and 11 nm upon adjustment of the water /oil volume ratio.

The large-scale preparation of the nanophase ferrites using the micro emulsion technique has long been a challenge since this synthetic approach usually produces



small amounts of solid materials, typically on the order of several tens of milligrams. According to two recent reports, large quantities of nanocrystalline ferrites could be produced in a single experiment by performing the precipitation reactions in a reverse micelle system [2.71]. Lee and coworkers reported the multi-gram preparation of variable sized  $\text{Fe}_3\text{O}_4$  nanocrystals by precipitating stoichiometric mixtures of iron salts with hydrazine in a water-sodium dodecylbenzene sulfonate-xylene micellar system. Refluxing the reaction solution for several hours under argon atmosphere resulted in the formation of pure nanometer-sized  $\text{Fe}_3\text{O}_4$  particles with a high crystallinity. Interestingly, the prolonged refluxing at temperatures around  $100^\circ\text{C}$  did not disrupt the micellar structure of the solution and allowed the preparation of non-aggregated  $\text{Fe}_3\text{O}_4$  nanocrystals with spheroidal shape and relatively tight size distribution. The particle dimensions could be varied between 2 nm and 10 nm by adjusting the relative amounts of the divalent and trivalent iron salts and the polar solvent /surfactant molar ratio. This large-scale preparation technique was adapted to the synthesis of other nanocrystalline transition metal ferrites, such as  $\text{MnFe}_2\text{O}_4$ ,  $\text{CoFe}_2\text{O}_4$ ,  $\text{NiFe}_2\text{O}_4$  and  $\text{ZnFe}_2\text{O}_4$ . The obtained particles have sizes that range from 4 nm to 6.5 nm depending on the nature of the divalent metal cation. Compared to  $\text{Fe}_3\text{O}_4$ , the mixed metal ferrite nanocrystals are characterized by more irregular shapes and broader size distributions. The great advantage of the synthetic procedure developed by Lee and coworkers lies in the use of relatively small quantities of organic solvents, similar to those employed in the conventional water-in-oil micro-emulsion method, whereas the amounts of the metal precursors are up to 10 times larger than those used in a regular experiment [2.71].

#### **2.4.2.2 Synthesis of Nanocrystalline Ferrites in Non-Aqueous**

##### **Medium**

In addition to the precipitation in aqueous solutions, nanocrystalline mixed metal oxides can be alternatively synthesized by chemical reactions performed in non-aqueous media. Although they are not always environmentally friendly, non-aqueous approaches present some major advantages over the conventional aqueous solution methods examples include a strict control over the size of the nanoparticles, a high crystallinity, as well as a tunable solubility in polar and non-polar solvents. Due to the high boiling point of the organic solvents, chemical reactions in non-aqueous solutions take place at much more elevated temperatures than those in aqueous media,



usually leading to the formation of highly crystalline products without the need of post-synthesis heat treatment. In addition, the reaction rates can be controlled much easier in non-aqueous media, thus allowing for a complete separation of the nucleation and growth processes and yielding nearly monodisperse nanoparticles with a controllable size, shape and agglomeration degree. One of the characteristics common to the organic solution techniques is the use of capping agents. In general, capping ligands are long chain organic molecules that passivity the nanoparticles' surface, thus inhibiting their growth and stabilizing them against clustering and aggregation. Depending on the nature of their free groups, the capping ligands facilitate the dispersion of the passivated nanocrystals into various solvents, either polar or non-polar, with the formation of stable colloidal suspensions. The non-aqueous techniques involved in the preparation of the nanocrystalline ferrites usually fall within two categories, *i. e.* the hydrolysis of the transition metal ions in polyol medium (the polyol method) and the thermal decomposition of single molecular precursors.

#### **2.4.2.2.1. The Polyol Method**

The hydrolysis of the transition metal ions in polyol (ethylene glycol, diethylene glycol or 1,2-propanediol) solutions with the formation of nanophase binary or mixed metal oxides is traditionally referred to as the polyol method. [2.72 - 2.73]. Although the polyol process was initially aimed at the synthesis of various micrometer to nanometer-sized metallic particles [Co, Ni, Cu, Ag, Pt, Pd, Sn, W, Rh, Ru,  $\text{Co}_x\text{Ni}_{100-x}$ ,  $\text{Fe}_z [\text{Co}_x\text{Ni}_{100-x}]_{(1-z)}$ ] [2.74 - 2.76], due to its simplicity and versatility this technique has been successfully extended to other types of nanocrystalline materials, including ferrites. In this process, the metallic particles were obtained by reducing the corresponding metal oxides or hydroxides with a polyol which acts not only as a reducing agent, but also as a solvent for the starting materials and a stabilizing agent for the resulting compounds [2.74 - 2.75]. When transition metal salts are used as precursor materials, their conversion into the corresponding metal hydroxides will require the presence of sodium hydroxide in the reaction system [2.76]. It was also observed that the addition of sodium hydroxide into the reaction mixture can affect the rate of the reduction process as well as the size of the as prepared metallic particles [2.75]. Because the presence of water in the

system can potentially affect the reduction of the metal ions, syntheses in polyol media are usually performed by refluxing the reaction mixture for extended periods of time. Thus, in addition to the water molecules, other organic compounds resulting from the oxidation of the polyols will be also removed during the course of the synthetic process [2.74-2.76]. Several factors, such as the reaction temperature the metal precursor/polyalcohol molar ratio the reaction time and the nature of the noble metal used as seeds in the heterogeneous nucleation of other metals or alloys were found to play an important role on the size of the resulting metallic nanoparticles [2.76].

Unlike the metals, the presence of a certain amount of water in the reaction mixture is essential for the preparation of metal oxide nanoparticles through the polyol process. This synthetic pathway, known as “forced hydrolysis in polyol medium” has been successfully applied to the preparation of various nanocrystalline oxides, such as  $\alpha$ -Fe<sub>2</sub>O<sub>3</sub> [2.77] and spinel-type ferrites [CoFe<sub>2</sub>O<sub>4</sub>, NiFe<sub>2</sub>O<sub>4</sub>] [2.72-2.73], respectively.

#### **2.4.2.2.2 Thermal Decomposition of Single Molecular Precursors**

A non-hydrolytic synthetic approach extensively used for the preparation of nanocrystalline ferrites is the thermolysis of single molecular precursors (organometallic compounds or metal-fatty acid complexes) in high boiling point organic solvents (long chain ethers, amines, alkenes) [2.78 - 2.79]. A major advantage of such one-pot synthetic route is related to the possibility to obtain large amounts of variable-sized metal oxide nanoparticles with high crystallinity and tight size distributions [2.78]. The similarity in both the size and the shape of the nanocrystals is critical for the formation of multi dimensional architectures (superlattices) which can be used as building blocks for the design of nanoscale optical, electronic and magnetic devices.

Sun *et al.* synthesized highly crystalline MFe<sub>2</sub>O<sub>4</sub> (M = Mn, Fe, Co) nanoparticles by refluxing solutions of metal acetylacetonates [M (acac)<sub>n</sub>, n = 1, 2] in phenyl (or benzyl) ether in the presence of 1,2-hexadecanediol as a reducing agent under a protected atmosphere. The as-prepared nanocrystals stabilized with oleic acid and oleyl amine had narrow size distributions ( $\sigma < 5\%$ ) and average diameters which can be varied between 3 and 10 nm by increasing the reaction time and temperature. According to them, bigger ferrite particles (10 - 20 nm) can be obtained through the

so-called “seed-mediated growth” method, which consists of performing the reaction between metal acetylacetonates and 1,2-hexadecanediol in solutions containing variable amounts of the as-prepared nanoparticles (3 - 10 nm) serving as seeds [2.80].



**CHAPTER III**

**SYNTHESIS AND CHARACTERIZATION  
TECHNIQUES**

## SYNTHESIS AND CHARACTERIZATION TECHNIQUES

### 3.1 Synthesis of MgFe<sub>2</sub>O<sub>4</sub> Nanoparticles

A lot of synthetic strategies for preparing nanosized magnesium ferrite have been presented in chapter two. The size and magnetic properties of MgFe<sub>2</sub>O<sub>4</sub> nanoparticles prepared by the co-precipitation method can be greatly varied depending on pH, salt concentration, temperature, stirring speed, counter ion nature, etc. The advantage of this method over the others is that the control of production of ferrite particles, its size and size distribution is relatively easy and there is no need of extra mechanical or subsequent step.

In this study, we have synthesized MgFe<sub>2</sub>O<sub>4</sub> nanoparticles by chemical co-precipitation method in alkaline aqueous media along with heat treatment at various temperatures. The size and size distribution was controlled by controlling the nucleation and growth rates through heat treatment.

#### 3.1.1 Materials

In this study, all reagent grade high purity chemicals were used without further purification. Magnesium nitrate hexahydrated [Mg(NO<sub>3</sub>)<sub>2</sub>.6H<sub>2</sub>O] and iron chloride hexahydrated [FeCl<sub>3</sub>.6H<sub>2</sub>O] were selected as a precursor chemicals because of their relative high solubility in water. Sodium hydroxide [8M NaOH] was used as the reaction agent. Deionized water was chosen as the solvent.

#### 3.1.2 Experimental Procedure

First, [Mg (NO<sub>3</sub>)<sub>2</sub>.6H<sub>2</sub>O] and FeCl<sub>3</sub>.6H<sub>2</sub>O with Mg:Fe atomic ratio of 1:2 were dissolved in deionized water. Deionized distilled water was used as a solvent in order to avoid the production of impurities in the final product. 8M solution of sodium hydroxide was prepared and slowly added to the salt solution drop wise. The pH of the solution was constantly monitored as the NaOH solution was added. The precipitated was heated to 80°C with constant stirring.

The ferrite formation takes place according to this reaction is described by



When reaction was completed the precipitate was filtered and washed several times using deionized water until the pH value of the solution became neutral. To get free particles from sodium compounds, the precipitate centrifuged for 20 minutes at 15000 rpm. Finally, the precipitate was dried at 90 °C for 36 hours in air to form a powder sample. The powder was pelletized and heated in box furnace at various temperatures range from 200 °C to 1400 °C. Formation of ferrites has been studied by X-ray diffraction, VSM and Mossbauer spectroscopy. Fig.3.1 summarizes the experimental procedure to synthesized  $\text{MgFe}_2\text{O}_4$  nanoparticles.

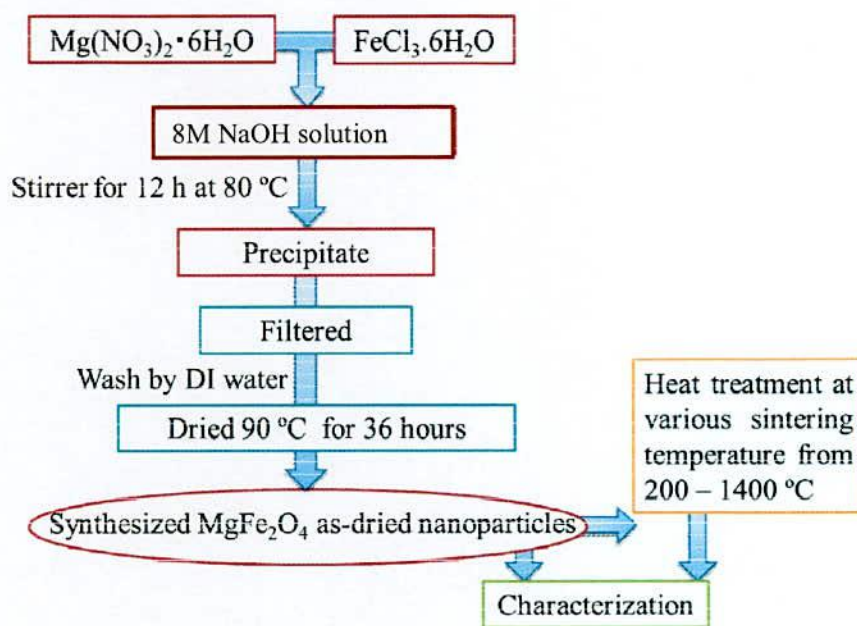


**Fig. 3.1** Flow chart of  $\text{MgFe}_2\text{O}_4$  nanoparticles synthesis by chemical co-precipitation method

### 3.2 X-Ray Diffraction

X-rays are the electromagnetic waves whose wavelength is in the neighborhood of  $1 \text{ \AA}$ . The wavelength of an X-ray is that the same order of magnitude as the lattice constant of crystals and it is this which makes X-ray so useful in structural analysis of crystals. X-ray diffraction (XRD) provides precise knowledge of the lattice parameter as well as the substantial information on the crystal structure of the material under



study. XRD is a versatile nondestructive analytical technique for identification and quantitative determination of various crystalline phases of powder or solid sample of any compound. When X-ray beam is incident on a material, the photons primarily interact with the electrons in atoms and get scattered. Diffracted waves from different atoms can interfere with each other and the resultant intensity distribution is strongly modulated by this interaction. If the atoms are arranged in a periodic fashion, as in crystals, the diffracted waves will consist of sharp interference maxima (peaks) with the same symmetry as in the distribution of atoms. Measuring the diffraction pattern therefore allows us to deduce the distribution of atoms in a material. It is to be noted here that, in diffraction experiments, only XRD via elastic scattering are measured.

The peaks in an XRD pattern are directly related to the atomic distance. Let us consider an incident X-ray beam interacting with the atoms arranged in a periodic manner as shown in two dimensions in Fig. 3.5. The atoms, represented as spheres in the illustration, can be viewed as forming different sets of planes in the crystal. For a given set of lattice planes with an inter-plane distance of  $d$ , the condition for a diffraction (peak) to occur can be simply written as

$$2d\sin\theta = n\lambda, \quad (3.1)$$

which is known as Bragg's law. In the equation,  $\lambda$  is the wavelength of the X-ray,  $\theta$  is the scattering angle, and  $n$  is an integer representing the order of the diffraction peak. The Bragg's Law is one of the most important laws used for interpreting X - ray diffraction data. From the law, we find that the diffraction is only possible when  $\lambda < 2d$  [3.1].

Three types of radiations are used for crystal diffraction studies; X- rays, electrons and neutrons. The X- ray wavelength commonly employed is the characteristic  $K_{\alpha}$  radiation,  $\lambda = 1.5418\text{\AA}$ , emitted by Copper. Thin sheets of the samples were prepared from the alloy ingot by rolling the ingot. Sharp strip like samples were cut from the thin sheet for Debye-Scherrer experiment.

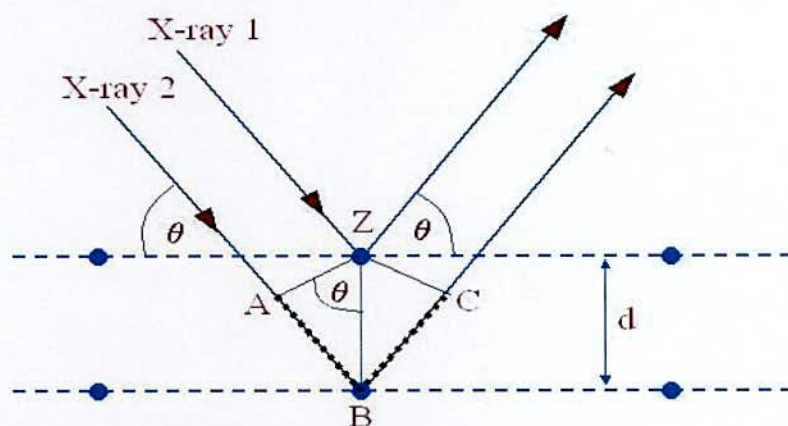


Fig.-3.2 Bragg's diffraction pattern

After heat treatment of the samples separately to remove strain the lattice parameter of the quenched specimen in the disordered state were measured by Debye-Scherrer method using Cu radiation. In the present case a special technique was used to determine the lattice parameter using Debye-Scherrer method. The shape of the sample was used as the same of Debye-Scherrer method sample. But in the conventional Debye-Scherrer experiment, sharp strip sample rotates and X-ray tube and camera remain fixed. In the present case, sample was kept fixed and X-ray tube and detector were moved to the  $\theta$  and  $2\theta$  ranges respectively. Instead of the film, digital data was recovered for the whole  $2\theta$  range.

After the pattern is obtained the value of  $2\theta$  is calculated for each diffraction lines; set of  $2\theta$  values is the raw data for the determination of the lattice parameters of the unit cell. Fig.3.3 shows the block diagram of X-ray diffractometer.

In the present work A PHILIPS PW3040 X'Pert PRO X-ray diffractometer was used to study the crystalline phases of the prepared samples in the Materials Science division, Atomic Energy Centre, Dhaka. Fig.3.4 shows the inside view of the PHILIPS X'Pert PRO XRD system. The powder diffraction technique was used with a primary beam power of 40 kV and 30 mA for Cu radiation. A nickel filter was used to reduce  $\text{Cu-K}\beta$  radiation and finally  $\text{Cu-K}\alpha$  radiation was only used as the primary beam. A  $2\theta$  scan was taken from  $25^\circ$  to  $70^\circ$  to get possible fundamental peaks with the sampling pitch of  $0.02^\circ$  and time for each step data collection was 1.0 sec. After that data of the samples were analyzed by computer software.

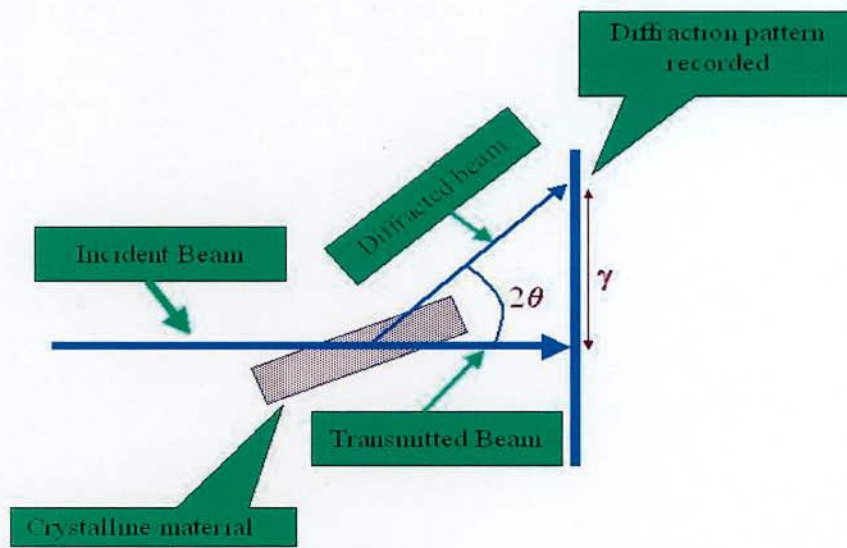


Fig. 3.3 Schematic diagram of X-ray diffraction



Fig. 3.4 A PHILIPS PW3040 X'Pert PRO X-ray diffractometer.

Both the programmable divergence and receiving sheets were used to control the irradiated beam area and output intensity from the powder sample, respectively. An anti scatter sheet was used just after the tube and in front of the detector to get parallel beam only. All the data of the sample were stored in the computer memory and later on analyzed then with computer "software" X'Pert HIGHS CORE



### 3.2.1 Interpretation of the XRD data

The XRD data consisting of  $\theta_{hkl}$  and  $d_{hkl}$  values corresponding to the different crystallographic planes are used to determine the structural information of the samples like lattice parameter and constituent phase. Lattice parameters of  $MgFe_2O_4$  ferrites samples were determined. Normally, lattice parameter of an alloy composition is determined by the Debye-Scherrer method after extrapolation of the curve. We determine the lattice spacing (inter planer distance),  $d$  using these reflections from the equation which is known as Bragg's Law.

$$2d_{hkl} \sin\theta = \lambda$$
$$\text{i.e. } d_{hkl} = \frac{\lambda}{2 \sin \theta}, \quad (3.2)$$

where  $\lambda$  is the wavelength of the X-ray,  $\theta$  is the diffraction angle and  $n$  is an integer representing the order of the diffraction.

The lattice parameter for each peak of each sample was calculated by using the formula:

$$a = d_{hkl} \times \sqrt{h^2 + k^2 + l^2}, \quad (3.3)$$

where  $h, k, l$  are the indices of the crystal planes. We get  $d_{hkl}$  values from the computer using software "X'-Pert HJGHS CORE". So we got ten 'a' values for ten reflection planes such as  $a_1, a_2, a_3, \dots$  etc. Determine the exact lattice parameter for each sample, through the Nelson-Riley extrapolation method. The values of the lattice parameter obtained from each reflected plane are plotted against Nelson-Riley function [3.2]. The Nelson-Riley function  $F(\theta)$ , can be written as

$$F(\theta) = \frac{1}{2} \left[ \frac{\cos^2 \theta}{\sin \theta} + \frac{\cos^2 \theta}{\theta} \right], \quad (3.4)$$

where  $\theta$  is the Bragg's angle. Now drawing the graph of 'a' vs.  $F(\theta)$  and using linear fitting of those points will give us the lattice parameter 'a<sub>0</sub>'. This value of 'a<sub>0</sub>' at  $F(\theta) = 0$  or  $\theta = 90^\circ$ . These 'a<sub>0</sub>'s are calculated with an error estimated to be  $\pm 0.0001$ .

### 3.2.2 Determination of Nanometric Grain Size by X-ray Diffraction

Nanocrystalline alloys are basically crystalline and because of their crystallinity exhibit Bragg scattering peaks in XRD experiments. However, due to their small size, significant fine particle broadening is observed in the Bragg peaks.

The condition for constructive interference, reinforcement of X-ray scattering from a crystalline solid is given by Bragg's law:

$$n\lambda = 2d \sin \theta \quad (3.5)$$

This equates the path difference of X-rays scattered from parallel crystalline planes spaced  $d = d_{hkl}$  apart to an integral ( $n$ ) number of X-ray wavelengths  $\lambda$ . Here  $\theta$  is the X-ray angle of incidence (and of diffraction) measured with respect to the crystalline planes. For an infinite crystal Bragg scattering occurs at discrete values of  $2\theta$  satisfying the Bragg condition, i.e. Bragg peaks are  $\delta$ -functions. For finite sized crystals the peaks are broadened over a range of angles as shown Fig. 3.5.

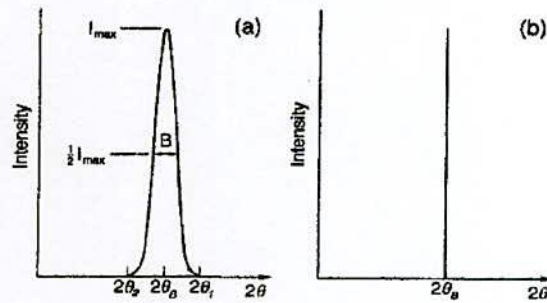


**Fig.3.5** Effect of fine particle broadening in XRD (a) fine particles and (b) perfect crystal

To better understand the phenomenon of fine particle broadening [3.3] we consider a finite crystal of thickness  $D_g = md$ , where  $m$  is an integer, and  $d$  is the distance between crystalline planes, i.e., there are  $m$  planes in  $D_g$ . Considering Fig. 3.5, if the broadened Bragg peak begins at an angle  $2\theta_2$  and ends at  $2\theta_1$ , the breadth of the peak or full width at half maximum is given as:

$$\beta = \frac{1}{2}(2\theta_1 - 2\theta_2) = \theta_1 - \theta_2 \quad (3.6)$$

Now consider the path differences for each of the two angles  $\theta_1$  and  $\theta_2$ , for X-rays traveling through the full thickness of the crystal. The width  $\beta$  is usually measured in radians, an intensity equal to half the maximum intensity. As a rough measure of  $\beta$ , we can take half the difference between the two extreme angles at which the intensity zero, which amounts to assuming that the diffraction line is triangle in shape. We now

write path difference equations for these two angles, related to the entire thickness of the crystal rather to the distance between adjacent planes.

$$2D_g \sin \theta_1 = (m+1)\lambda \quad (3.7)$$

$$2D_g \sin \theta_2 = (m-1)\lambda \quad (3.8)$$

By subtraction we find:

$$D_g (\sin \theta_1 - \sin \theta_2) = \lambda \quad (3.9)$$

$$D_g 2 \cos \left( \frac{\theta_1 + \theta_2}{2} \right) \sin \left( \frac{\theta_1 - \theta_2}{2} \right) = \lambda \quad (3.10)$$

But  $\theta_1$  and  $\theta_2$  are both very nearly equal to  $\theta$ , so that  $\theta_1 + \theta_2 \approx 2\theta$  and

$\sin \left( \frac{\theta_1 - \theta_2}{2} \right) \approx \left( \frac{\theta_1 - \theta_2}{2} \right)$  so that equation (3.10) can be written as:

$$2D_g \cos \theta \left( \frac{\theta_1 - \theta_2}{2} \right) = \lambda \quad (3.11)$$

From equation (3.6) and equation (3.11) we get:

$$\beta D_g \cos \theta = \lambda \quad (3.12)$$

$$D_g = \frac{\lambda}{\beta \cos \theta} \quad (3.13)$$

A more exact empirical treatment yields:

$$D_g = \frac{0.9\lambda}{\beta \cos \theta} \quad (3.14)$$

which is known as the Scherrer's formula. It is used to estimate the particle size of very small crystals from the measured width of their diffraction curves.

The aim of the present study was to prepare nanometer size  $\text{MgFe}_2\text{O}_4$  particles. Therefore, particle size determination was also important in the present study. Particle size of the prepared  $\text{MgFe}_2\text{O}_4$  nanoparticles was determined from the strongest peak of each XRD patterns using Scherrer's equation (3.14), where  $D_g$  is the average particle size,  $\lambda$  is the wavelength of the radiation used as the primary beam of  $\text{Cu-K}_\alpha$  ( $\lambda = 1.54178 \text{ \AA}$ ),  $\theta$  is the angle of incidence in degree and  $\beta$  is the full width at half maximum (FWHM) of the strongest reflection (311) in radian. At (311) reflection's position of the peak, the value of instrumental broadening was found to be  $0.07^\circ$ .



### 3.3 Vibration Sample Magnetometer

The principle of vibrations sample magnetometer (VSM) is the measurement of electromotive force induces by magnetic sample when it is vibrate at a constant frequency in the presence of a static and uniform magnetic field. A small part of the (10 - 50 mg) was weighted and made to avoid movements inside the sample holder shown in Fig. 3.6. VSM is a versatile and sensitive method of measuring magnetic properties developed by S. Foner [3.4] and is based on the flux change in a coil when the sample is vibrate near it.

The simplest of these is the rotating coil which rotates at a fixed angular velocity. Therefore the amplitude of the generated voltage by rotating coil is proportional to the magnetic induction and therefore the amplitude can be used to measure magnetic induction (B) or magnetic field (H) in free space. The signal can be read directly as an AC voltage or converted to a DC voltage which is proportional to the amplitude.

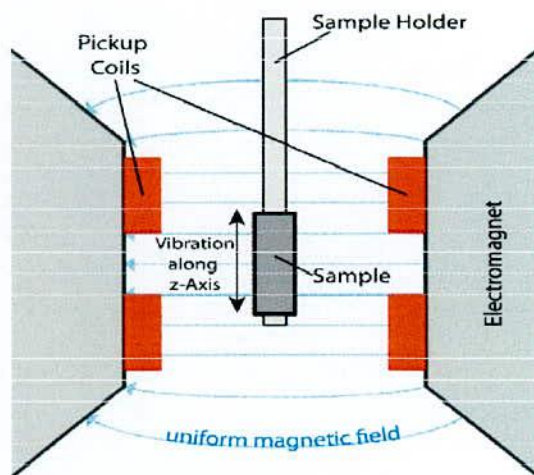


Fig 3.6 Vibrating Sample Magnetometer: sample holder and detection mechanism

Fig. 3.7 shows VSM of Model EV7 system. The magnetic properties measurement system model EV7 is a sophisticated analytical instrument configured specially for the study of the magnetic properties of the small samples over a broad range of temperature from 103K to 800K and magnetic field from -20kOe to +20kOe. The VSM is designed to continuously measure the magnetic properties of materials as

a function of temperature and the field. In this type of magnetometer, the sample is vibrated up and down in a region surrounded by several pick up coils. The magnetic sample is thus acting as a time-changing magnetic flux, varying the electric flux is accompanied by an electric field and the field induces a voltage in pick up coils. This alternating voltage signal is processed by a control unit system, in order to increase the signal to noise ratio. The result is a measure of the magnetization of the sample.

By using a compact gradiometer pickup coil configuration, relatively large oscillation amplitude (1-3mm peak) and a frequency of 40 Hz, the system is able to resolve magnetization changes of less than  $10^{-6}$  emu at a data rate of 1 Hz. The VSM option for the PPMS consists primarily of a VSM line a motor transport (head) for vibrating the sample, a coil set puck for detection, electronics for driving the linear motor transport and detecting the response from the pickup coils. If a sample is placed in a uniform magnetic field, created between the poles of electromagnet, a dipole moment will be induced. If the sample vibrates with sinusoidal motion sinusoidal electrical signal can be induced in suitable placed pick-up coils. The signal has same frequency of vibration and its amplitude will be proportional to the magnetic moment.



**Fig. 3.7** Vibrating Sample Magnetometer at Materials Science Division, AECD



The sample is attached to the end of a sample rod that is driven sinusoidally. The center of oscillation is positioned at the vertical center of a gradiometer pickup coil. The precise position and amplitude of oscillation is controlled from the VSM motor module using an optical linear encoder signal read back from the VSM linear motor transport. The voltage induced in the pickup coil is amplified and lock-in detected in the VSM detection module.

The VSM detection module uses the position encoder signal as a reference for the synchronous detection. This encoder signal is obtained from the VSM motor module, which interprets the raw encoder signals from the VSM linear motor transport. The VSM detection module detects the in-phase and quadrature-phase signals from the encoder and from the amplified voltage from the pickup coil.

The sample is fixed to sample holder located at the end of a sample rod mounted in a electromechanical transducer. The transducer is driver by a power amplifier which itself is driver by an oscillator at a frequency of 90Hz. So, the sample vibrates along the z-axis perpendicular to the magnetizing field. The latter induce a signal in the pick-up coil system that is fed to a differential. The output of the differential amplifier is subsequently fed into a tuned amplifier and an internal lock in amplifier that receives signal supplied by the oscillator. The output of the lock-in amplifier, or the output of the magnetometer itself, is a DC signal proportional to the magnetic moment of the sample being studied. Calibration of the VSM is done by measuring the signal of a pure Ni standard of Known saturation magnetic moment placed in the saddle point. The basic instrument included the electromechanical system and the electronic system including in personal computer. Laboratory electromagnet coils of various maximum field strengths may be used.

### **3.4 SQUID Magnetometer**

Superconducting Quantum Interface Device (SQUID) magnetometer MPMS XL, USA is the most sensitive available device for measuring magnetization at the Department of Engineering Sciences, Ångström laboratory, Uppsala University, Sweden. The magnetic properties measurement system MPMS XL is a sophisticated analytical instrument configured specially for the study of the magnetic properties of small samples over a broad range of temperature from 4.2 K to 400 K and magnetic fields from -50 KOe to +50 KOe. This standard system can measure the magnetic moment of solid, powder



and liquid samples with a differential sensitivity of  $10^{-9}$  emu and can handle a maximum signal size of 0.5 emu.

A general view of the MPMS XL with its system components is shown in Fig. 3.8 SQUID magnetometers are used to characterize materials when the highest detection sensitivity over a broad temperature range and using applied magnetic fields up to several Tesla is needed. Nowadays, this instrument is widely used worldwide in research laboratories. The system is designed to measure the magnetic moment of a sample, from which the magnetization and magnetic susceptibility can be obtained. Therefore, SQUID magnetometers are versatile instruments that perform both, DC and AC magnetic moment measurement. MPMS MultiVu is the software application controlling the RSO system.



**Fig 3.8** MPMS XL SQUID Magnetometer

The major components of a SQUID magnetometer are: The RSO sample rod consists of one long, graphite sample rod; one short, graphite sample rod; and two centering plugs, superconducting magnet, superconducting detection coil, a SQUID connected to the detection coil, superconducting magnetic shield. Superconducting magnets are solenoid made of superconducting wire which must be kept at liquid helium

Dewar. The uniform magnetic field is produced along the axial cylindrical bore of the coil. The superconducting pick-up coil system, which is configured as a second order gradiometer is placed in the uniform magnetic field region of the solenoidal superconducting magnet. The SQUID device is usually a thin film that functions as an extremely sensitive current to voltage converter.

During an RSO measurement, a shaft encoder on the servo motor tracks the position of the sample. The position is recorded synchronous to the acquisition of the SQUID signal. The data is analyzed by using a nonlinear, least-squares fitting routine to fit the data to an ideal dipole response. The magnetic moment calibration for the MPMS is determined by measuring a palladium standard over a range of magnetic fields and by then adjusting the system calibration factors to obtain the correct moment for the standard. The standard is a right circular cylinder approximately 3 mm in diameter  $\times$  3 mm in height. Samples of this size or smaller effectively imitate a point dipole to an accuracy of approximately 0.1%.

Measurements are done in this equipment by moving the samples through the second order gradiometer. Hence, the magnetic moment of the sample induces an electric current in the pick-up coil system. Superconducting magnetic shield is used to shield the SQUID sensor from the fluctuations of the ambient magnetic field of the place where the magnetometer is located and from the large magnetic field produced by the superconducting magnet. It is an important feature of the instrument that one can change the magnetic field either by "oscillate mode" or "no overshoot mode". The oscillate mode is used to minimize the remanent field of the magnet, whenever an accurate value of magnetic field is needed, e.g. in case of zero field cooling. In the hysteresis measurement the no overshoot mode has been selected, in which the field is changed directly from one value to another, and the magnet is returned to its persistent mode.

The accuracy of an RSO sample measurement is determined by how well the sample is centered within the SQUID pickup coils. If the sample is not centered, the coils read only part of the magnetic moment of the sample. Properly centering the sample is particularly important if it will be measured at the maximum slope position. During maximum slope position measurements, MPMS MultiVu cannot use auto tracking or the iterative regression algorithm, which both help keep the sample correctly positioned, even when temperature changes alter the geometry of the sample rod.

The new temperature sweep mode of operation provides MPMSXL users with the ability to take magnetic measurements while sweeping the system temperature at a controlled rate, automatically with no manual intervention. This mode provides a



controlled, monotonic change in temperature during a measurement sequence at rates up to 10 K/min. Measurements of temperature dependence over large temperature ranges, which previously required time consuming temperature stabilization, can now be made quickly and precisely using temperature sweep mode.

The main components of a SQUID magnetometer are:

- (i) Superconducting magnet (that must be acquired together is programmable bipolar power supply);
- (ii) Superconducting detection coil which is coupled inductively to the sample
- (iii) A SQUID connected to the detection coil and
- (iv) Superconducting magnetic shield.

High sensitivity is possible because this device responds to a fraction of the flux quantum. The SQUID device is usually a thin film that functions as a extremely sensitive current to voltage converter. A measurement is done in this equipment by moving the sample through the second order gradiometer. Hence the magnetic moment of the sample induces an electric current in the pick-up coil system. A change in the magnetic flux in these coils changes the persistent current in the detection circuit. So, the change in the current in the detection coils produce variation in the SQUID output voltage proportional to the magnetic moment of sample.

The difference between low and high temperature SQUID's and their suitability for specific applications is discussed. Although SQUID electronics have the capability to operate well above 1 MHz, most applications tend to be at lower frequencies. Specific examples of input circuits, detection coil configuration for different applications and environments along with expected performance.

SQUID measures the magnetic moment by moving the sample through the detection coil. The magnetic moment of the sample creates a flux in the detection coil, which changes with the sample position. The flux is converted to a voltage by the magnetometer and the voltage versus sample position data is further used to extract the magnetic moment. The software package supplied with the MPMS analyzes the voltage versus sample position data and determines a value for the magnetic moment as a result of a fitting procedure between a theoretically expected curve and the experimental data.



### 3.5 Mössbauer Spectroscopy

Mössbauer spectroscopy can give very precise information about the chemical, structural, magnetic and time - dependent properties of a material. Key to the success of the technique is the discovery of recoilless  $\gamma$ -ray emission and absorption, now referred to as the 'Mössbauer Effect', after its discoverer Rudolph Mössbauer, who first observed the effect in 1957 and received the Nobel Prize in Physics in 1961 for his work.

In the content of magnetization one learns about the internal magnetic field and hence magnetic moment, at the local sites of the resonant nucleus. Careful analysis can also tell about the relative orientation of the magnetic moments. Mössbauer spectroscopy yields information on the magnetic properties of individual atoms rather than on assemblies of atoms as in conventional magnetization measurements. Mössbauer spectroscopy is used for the identification of magnetic field distribution of magnetic atoms in magnetic materials by the evaluation of the collected spectra. This is a very useful technique for studying the nature and the number of nearest magnetic neighbors in magnetic alloys.

The Mössbauer effect provides information about the local magnetic and electronic environment of Mössbauer nuclei (i.e.  $^{57}\text{Fe}$  or  $^{119}\text{Sn}$ ) in a sample. Since this technique does not require the application of an external field, it is possible to observe very weak magnetic interactions, without the perturbing effect of the external field.

Mössbauer spectroscopy has also been used to determine the average direction of magnetization by using the well known fact that for the  $^{57}\text{Fe}$ , The intensity of the six lines of the hyperfine spectra have an area ratio 3: Z: 1:1: Z: 3, Where  $Z = \frac{4}{1 + \cot^2 \theta}$ ,  $\theta$  being the angle between the direction of magnetic field at the nucleus and the direction of  $\gamma$ -ray emission [3.5]. In  $^{57}\text{Fe}$  the strength of this magnetic field is  $H=33\text{T}$  [3.6] at room temperature. The value  $Z$  varies from 0 for the axis magnetization in the sample phase to 4 for the axis of magnetization in sample plane.

Mössbauer spectroscopy is a technique which enables these energy levels to be investigated since the recoil free processes arising from the Mössbauer effect lead to the resonant absorption of  $\gamma$ -rays with an extremely precise energy. Hence, small changes in energy levels because of the hyperfine interactions between the nucleus

and surrounding changes can be detected with the technique. A Mössbauer spectrum is characterized by the number, shape, position and relative intensity of the various absorption lines.

### 3.5.1 Mössbauer Effect

The principle of the Mössbauer effect is essentially the observation of fine structure in the transition between different nuclear energy levels, e.g. of  $^{57}\text{Fe}$  or  $^{119}\text{Sn}$  nuclei, by means of nuclear resonance absorption or fluorescence radiation. In the experiment a source containing  $^{57}\text{Co}$  nuclei provides a convenient supply of excited  $^{57}\text{Fe}$  nuclei, which decay into the ground state accompanied by a  $\gamma$ -ray emission.

Nuclear transitions emitting  $\gamma$ -radiation, which are not preceded by phonon transitions. These zero-phonon gamma transitions, take place between the excited and ground state nuclear energy levels of the nucleus which is bound in a solid matrix as reported by Mössbauer [3.7]. Therefore, the nucleus is no longer isolated, but fixed with the lattice. In this situation the recoil energy may be less than the lowest quantized lattice vibration energy and consequently the  $\gamma$ -ray energy may be emitted without any loss of energy due to the recoil of nucleus. This is known as the Mössbauer effect. The frequency spreads of such transitions which occur between nuclear excited states are solely determined by the energy uncertainty of the nuclear excited state involved. The Mössbauer  $\gamma$ -rays has a finite spread in energy which is quantized by a line width, defined as the full width at half maxima of maximum intensity and related to the life time of the nuclear excited state. The line width restricts the number of isotopes in which the Mössbauer effect is observed.

The important parameters which can be measured by using Mössbauer spectroscopy are describing the interaction of the nucleus with the surrounding atomic electrons. These parameters give information about the nature of the chemical bonds, electric field gradient and magnetic ordering moments. The Hamiltonian for the interaction between the nucleus and the surrounding changes may be written as [3.8]

$$H = E_0 + M_1 + E_2 + \dots \quad (3.15)$$

Where  $E_0$  represents electric monopole coulombing interaction between nuclear charges and the electron clouds which affect the nuclear energy levels,  $M_1$  refers to magnetic dipole interaction between nuclear magnetic moments and the effective magnetic field at the nucleus and  $E_2$  represents the electric quadrupole interaction



between electric field gradient at the nucleus and the electric quadrupole moment of the nucleus. Higher order terms are usually very small and can be neglected.

This is most often achieved by oscillating a radioactive source with a velocity of a few mm/s and recording the spectrum in discrete velocity steps. Fractions of mm/s compared to the speed of light ( $3 \times 10^{11}$  mm/s) gives the minute energy shifts necessary to observe the hyperfine interactions. For convenience the energy scale of a Mössbauer spectrum is thus quoted in terms of the source velocity, as shown in Fig.3.9.

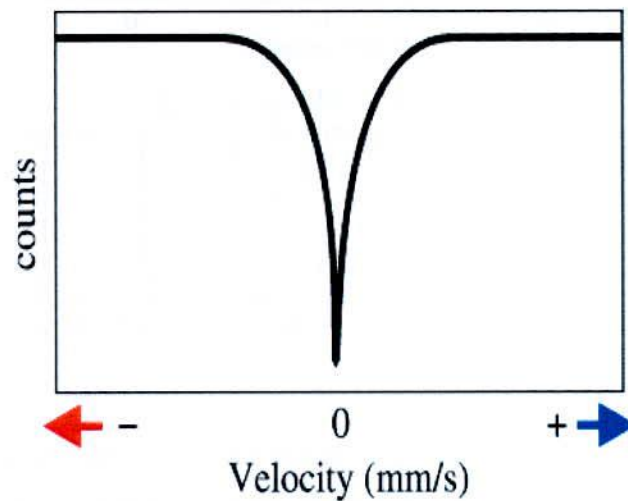


Fig.3.9 Simple spectrum showing the velocity scale and motion of source relative to the absorber

In Fig.3.9 the absorption peak occurs at 0 mm/s, where source and absorber are identical. The energy levels in the absorbing nuclei can be modified by their environment in three main ways: by the Isomer Shift, Quadrupole Splitting and Magnetic Splitting.

### 3.5.1.1 Isomer Shift

The isomer shift arises due to the slight change in the Coulomb interaction between the nuclear and electronic charge distributions over the nuclear volume which is associated with the slight increase of the  $^{57}\text{Fe}$  nucleus in the  $I = \frac{3}{2}$  state. In a Mössbauer spectrum the isomer shift is the velocity of the center of gravity of the



Thermal vibration of the nuclei will also shift the  $\gamma$ -ray energy. As these thermal vibrations are temperature dependent, the temperature of both the source and absorber should be considered when quoting isomer shifts.

Measurement of isomer shifts have been performed in a variety of compounds. Expression in velocity until the isomer shift is given by

$$V = c [\psi(0)_s^2 - \psi(0)_A^2] \quad (3.16)$$

where  $\psi(0)^2$  is the difference of electron densities at the nuclear sites for the sources and absorbers used and  $c$  is a constant characteristic for the particular  $\gamma$ -transition and is independent of the chemical environment.

The IS arises from the fact that a nucleus has a finite volume and S-electrons spend a fraction of their time inside the nuclear region. The nuclear charge thus interacts electro statically with the S-electron charge. As a result of this interaction the nuclear energy levels get shifted by a small amount, the shift depends upon the chemical environment. Although, we cannot measure change directly, it is possible to compare values by mean of a suitable reference which can be either the  $\gamma$ -ray source or another standard absorber. The observed range of IS is within an order of magnitude of the natural line width of the transition i.e,  $10^{-8}$  to  $10^{-9}$  ev. Isomer shifts provides important information concerning the nature of the chemical bond because the outer electrons (valence electrons) would be must effected by changes chemical surrounding and consequently the changes in the outer S-electrons densities would contributed.

### 3.5.1.2 Electric Quadrupole Splitting

The interaction of the quadruple moment of a nucleus with an electric field gradient (EFG) established at its site by the surrounding environment causes quadrupole splitting in nuclear levels [3.7-3.8]. An oblate (flattened) nucleus has a negative quadrupole moment while a prolate (elongated) one has a positive moment. Nuclei whose spin is up or  $\frac{1}{2}$  are spherical symmetric and have zero quadrupole moment and thus the ground state of  $^{57}\text{Fe}$  with  $I = \frac{1}{2}$  does not exhibit quadrupole

splitting. While determining the isomer shift; it is assumed that the nuclear charges distribution is spherical. However, nuclei in states with a nuclear angular momentum which are greater than  $\frac{1}{2}$  have in general non-spherical charge distribution which are characterized by a nuclear quadrupole moment. When the nuclear quadrupole moment experiences an asymmetric electric field produced by the arrangement of asymmetric electronic charge distribution and characterized by the electric field gradient (EFG), an electric quadrupole interaction occurs which gives rise to a splitting of the nuclear energy levels corresponding to different alignments of the quadrupole moment with respect to the principal axis of the nuclear quadrupole is fixed for a certain nucleus and hence the EFG can be determined from the Mössbauer Spectrum.

The valance electrons of the Mössbauer atoms and the asymmetry in the electronic structure contribute to the EFG and this is known as valence contributions. Lattice contribution is due to the asymmetric arrangement of Legend atoms in non-cubic Lattices. Molecular orbits and the polarization of the core electrons also modify the EFG. For the EFG, the greatest contribution comes from the electrons on the ion. The polarizable nature of the electron cloud may change the EFG by increasing or decreasing it and is described quantitatively by the sternheimer anti shielding factors [3.9]. For the open shell ion (non S-state) such as  $Fe^{+2}$ , the principal source of  $q$ ; namely  $q_{val}$  comes from integrating over the valence electrons on the Mössbauer ion itself, plus a secondary contribution of  $q_{lat}$  from the rest of the crystal ( usually assumed to be a sum over point charges).

Therefore

$$q = (1 - R)q_{val} + (1 - \gamma_{\alpha})q_{lat} \quad (3.17)$$

where Sternheimer factor  $R$  and  $\gamma_{\alpha}$  denote the fraction of each EFG arising from deformed closed sub shells in the Mössbauer atom.

The quantum mechanical expression that describes the interaction between a nucleus with quadrupole moment  $eQ$  and EFG  $q$  is given by the Hamiltonian operator

$$H = \frac{eqa}{4I(2I-1)} [3I_z^2 - I(I+1) + \frac{n}{2}(I_+^2 - I_-^2)] \quad (3.18)$$

Where  $I_+$  and  $I_-$  are the raising and lowering operators for the conventional spin operators. For direct determination of quadrupole moment values, we discuss the

determination of the quadrupole moment of the  $\frac{3}{2}$ , 14.4 Kev state of  $\text{Co}^{57}$ . For the ferrous  $\text{Fe}^{+2}$  state, the EFG is predominantly because of lattice contribution in the expression

$$q = (1 - R)q_{\text{val}} + (1 - \gamma_a)q_{\text{lat}} \quad (3.19)$$

$m_l = \pm \frac{1}{2}$  and  $m_l = \pm \frac{3}{2}$ . This is shown in Fig. 2.11, giving two line spectrum or 'doublet'.

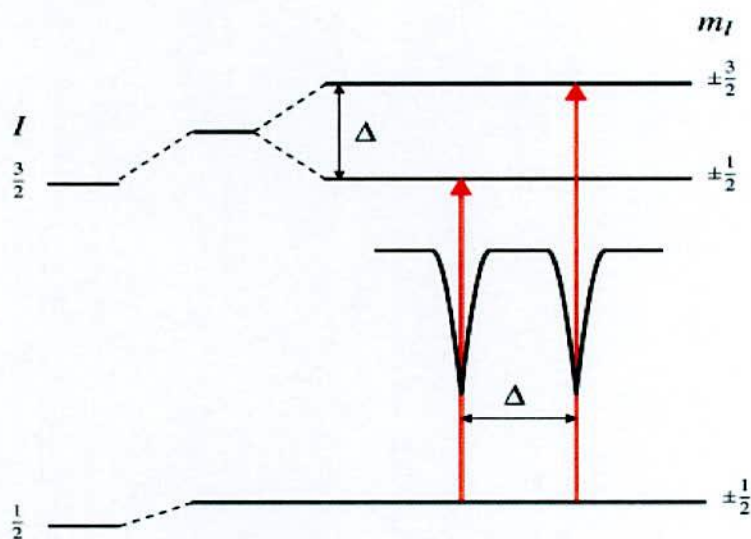


Fig.3.11 Quadrupole splitting for  $\frac{3}{2}$  to  $\frac{1}{2}$  transition. The magnitude of quadrupole splitting,  $\Delta$ , is shown

For ferric ( $\text{Fe}^{+3}$ ) iron, the quadrupole splitting in  $\text{O-Fe}_2\text{O}_3$  was studied. Since this ion is in the  ${}^6S_{5/2}$  state; no contribution is expected from  $q_{\text{val}}$  and only  $q_{\text{lat}}$  must be considered. The Mössbauer spectrum shows a magnetic six-line pattern. The quadrupole interaction shifts the spectrum asymmetrically.



In the case of an isotope with a  $I = \frac{3}{2}$  excited state, such as  $^{57}\text{Fe}$  or  $^{119}\text{Sn}$ , the excited state is split into two sub states. The magnitude of splitting,  $\Delta$ , is related to the nuclear quadrupole moment,  $Q$ , and the principle component of the EFG,  $V_{zz}$ , by the relation

$$\Delta = \frac{eQV_{zz}}{2} \quad (3.20)$$

### 3.5.1.3 Magnetic Splitting

The hyperfine Hamiltonian for a nuclear magnetic dipole in a magnetic field  $H$  is given by

$$\begin{aligned} H_M &= -\mu \cdot H \quad (\text{Since } \mu = g\mu_N I) \\ H_M &= -g\mu_N I \cdot H \end{aligned} \quad (3.21)$$

Where  $\mu_N$  is the nuclear magnetron  $\left(\frac{e\hbar}{2m_N C}\right)$ ,  $m_N$  is the mass the nucleus and  $g$  is the gyromagnetic ratio. The energy levels are

$$E_M = -\frac{\mu_N H m_I}{I} = gM_N H m_I \quad [m_I = I, I-1, \dots, \dots] \quad (3.22)$$

These indicate that  $2I+1$  magnetic sub levels are equally spaced with a separation of  $g\mu_N H$  between the levels.

When a nucleus experiences a magnetic field, a magnetic dipole interaction takes place between the nuclear magnetic moment and the magnetic field. This interaction splits the nuclear state (with  $I > 0$ ) into two substates and the excited state with  $I = \frac{3}{2}$  splits into four substates. The selection rules with  $m_I = 0, \pm 1$  allows six possible transitions between these sets of excited and ground state leading to six-line Mössbauer spectrum.

The magnetic splitting is proportional to the magnetic field at the nucleus. The intensities of the absorption lines depend on the transitions probabilities between the different substates. Contribution for magnetic hyperfine field can come from all electrons that are present within the atom, the molecule and the lattice. The effects of magnetic hyperfine fields are observed in the Mössbauer spectra of magnetically ordered systems if the electron spin relaxation times are long. Magnetic splitting can

arise due to magnetic hyperfine field and any external applied field and the field at the nucleus is a vector sum of two.

This magnetic field splits nuclear levels with a spin of  $I$  into  $(2I+1)$  substates. This is shown in Fig.3.12 for  $^{57}\text{Fe}$ . Transitions between the excited state and ground state can only occur where  $m_I$  changes by 0 or 1. This gives six possible transitions for  $\frac{3}{2}$  to  $\frac{1}{2}$  transition, giving a sextet as illustrated in Fig. 3.12, with the line spacing being proportional to  $B$  effective magnetic field at the nucleus.

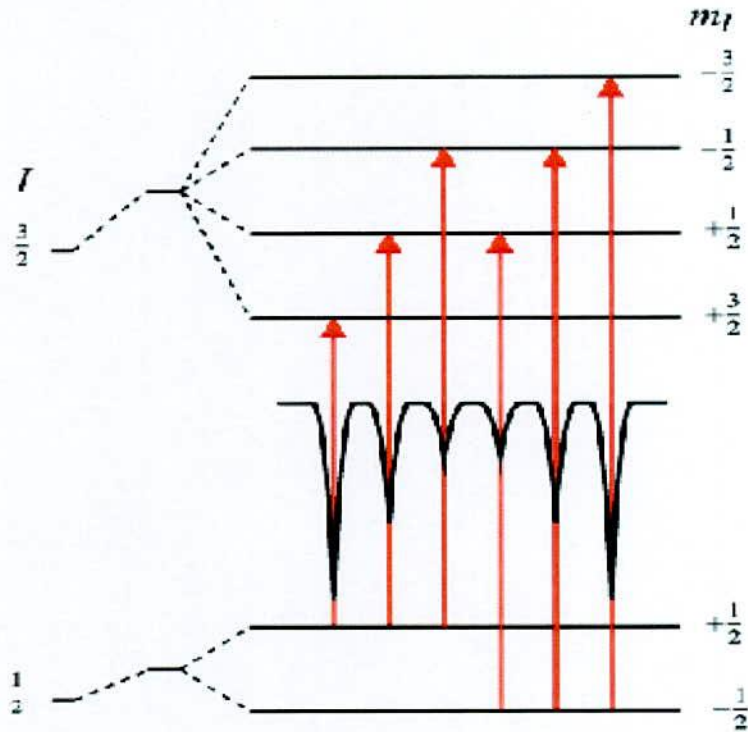


Fig. 3.12 Magnetic splitting of the nuclear energy levels

The line positions are related to the splitting of the energy levels, but the line *intensities* are related to the angle between the Mössbauer gamma-ray and the nuclear spin moment. The outer, middle and inner line intensities are related by:

$$3 : \frac{4 \sin^2 \theta}{1 + \cos^2 \theta} : 1$$

meaning the outer and inner lines are always in the same proportion but the middle lines can vary in relative intensity between 0 and 4 depending upon the angle the

nuclear spin moments make to the  $\gamma$ -ray. In polycrystalline samples with no applied field this value averages to 2 but in single crystals or under applied fields the relative line intensities can give information about moment orientation and magnetic ordering as shown in Fig.3.12.

### 3.5.1.4 Magnetic Hyperfine Interaction

The internal magnetic field at the nucleus has its origin from the spin and radial and angular distribution of the electron density in the atom. The magnetic field is given by [3.10-3.11]

$$H = -\frac{8}{3}n\mu_B |\psi_{\uparrow}(0)|^2 \bar{s} - 2\mu_B \langle \bar{l} \rangle \left\langle \frac{1}{r^3} \right\rangle - 2\mu_B \frac{\langle 3\bar{r}\bar{\Delta}\bar{r} - r^2\bar{s} \rangle}{r^5} \quad (3.23)$$

Where  $\mu_B$  is Bhor magnetron,  $s$  and  $l$  are operators for the spin and orbital moment of the electron and  $|\psi_{\uparrow}(0)|^2$  is the electron density at the nucleus with  $+\frac{1}{2}$  spin projection.

The first term, in this expression is known as Fermi contact term which describes the contact magnetic interaction between the s-electrons and a nucleus, only S- electron contribute to the Fermi contact term since the S- electron have a non-zero charge density at the nucleus. The field resulting from this source is very large compared to that from other sources. The Fermi contact field mainly arises from the polarization of the spins of paired S- electrons by the unpaired 3d electrons via exchange attraction that emits between electrons of like spins [3.12-3.13]. The inner core electrons (1s and 2s) produce a large negative field, whereas 3s and 4s electron produce smaller positive fields resulting in a net negative field almost of the nuclei [3.14]. The second term in the above expression is known as orbital current field and it is produce due to an interaction of the unquenched orbital moment of the electron with the nuclear magnetic moment.

The third term known as Dipolar field arises due to dipole-dipole interactions operation between the electron spin and the nuclear magnetic moment. For observing a well resolved Zeeman splitting in the Mössbauer spectrum, two conditions have to satisfied

$$\tau_0 > \tau_L \quad \text{and} \quad \tau_s > \tau_L; \quad (3.24)$$



Where  $\tau_0$  the life time of the nuclear is excited state,  $\tau_s$  is the electron spin correlation time and  $\tau_L$  is the Larmour precession time of the nucleus. The first conditions state that the Zeeman splitting must be larger than the natural line width. The second condition states the relationship between the spin correlation time and nuclear Larmour precession time. In paramagnetic system the spin correlation time is so small, of the order of  $10^{-12}$  and  $10^{-14}$  gu, That during on Larmour precession, the electron of spin undergoes several fluctuation and hence the nuclei will not experience any hyperfine field to presses around and hence no magnetic splitting will be absorbed. In magnetically ordered system, the strong exchange interaction helps to increase the spin correlations times, thus the direction of the hyperfine field is steady and the nucleus spin process round it to lift the degeneracy of the nuclear levels yielding hyperfine split spectrum.

### 3.6 Experimental Procedure for Mössbauer Spectrometer

Mössbauer experiments on the magnesium ferrite powder sample were performed Materials Science Division, AECD. Mössbauer measurement can be made in two different geometries, transmission and scattering configurations. In the present work only transmission geometry was used. In transmission type measurements, the intensity of  $\gamma$ -rays transmitted through a thin absorber are measured with the help of a suitable detector like proportional counter.  $\gamma$ -ray source is driven electromagnetically by a transducer so as to Doppler shift the energy spectrum is obtained by counting transmitted  $\gamma$ -rays by small and known amounts. The absorption Mössbauer spectrum is obtained by counting transmitted  $\gamma$ -rays as a function of the source to absorber velocity. The Mössbauer effect allows for very precise measurements of  $\gamma$ -rays resonance. In combination with the Doppler shift, it can be used to observe the hyperfine splitting of the  $^{57}\text{Fe}$  nucleus and thus determine the internal field of the  $^{57}\text{Fe}$  nuclei. A measurement of the line width can also be made. In our experiment, a FeCo nucleus decays into an excited state of the  $^{57}\text{Fe}$  nucleus shown in Fig.-3.13

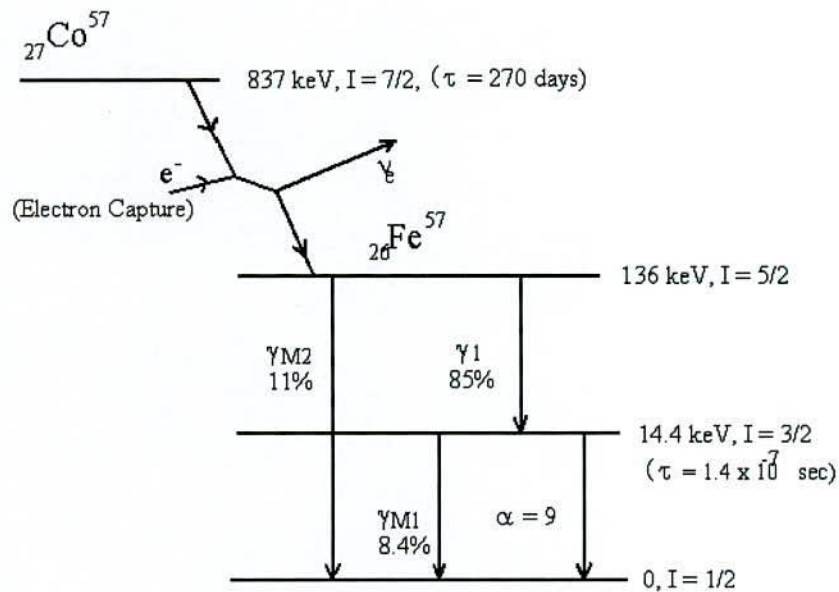


**Fig. 3.13** Energy level scheme of  $^{57}\text{Fe}$  Mössbauer spectroscopy involves the 14.4 keV transition. Intensities are given in % of decays

Since FeCo is not ferromagnetic, the decaying nucleus does not experience any Zeeman splitting and emits 14.4 keV  $\gamma$ -rays. The emitted gamma rays are incident on an absorber with roughly 2.2% abundance of  $^{57}\text{Fe}$  nuclei. This concentration is sufficient that any absorbing nucleus experiences Zeeman splitting due to the magnetic field from surrounding  $^{57}\text{Fe}$  atoms. If the source is at rest relative to the absorber, the splitting of energy levels in the absorber prevents resonant absorption. If the relative velocity of the source in the direction of the absorber increases, Doppler shift  $\gamma$ -rays can be made to match resonance conditions with the split levels in the absorber. By changing the velocity of the source, resonance conditions can be reached for each of the different transitions in the absorber. When in resonance, the absorber will absorb much more of the gamma rays. The shape of the excess absorption peaks may be compared to theoretical estimates and the natural line width may be determined

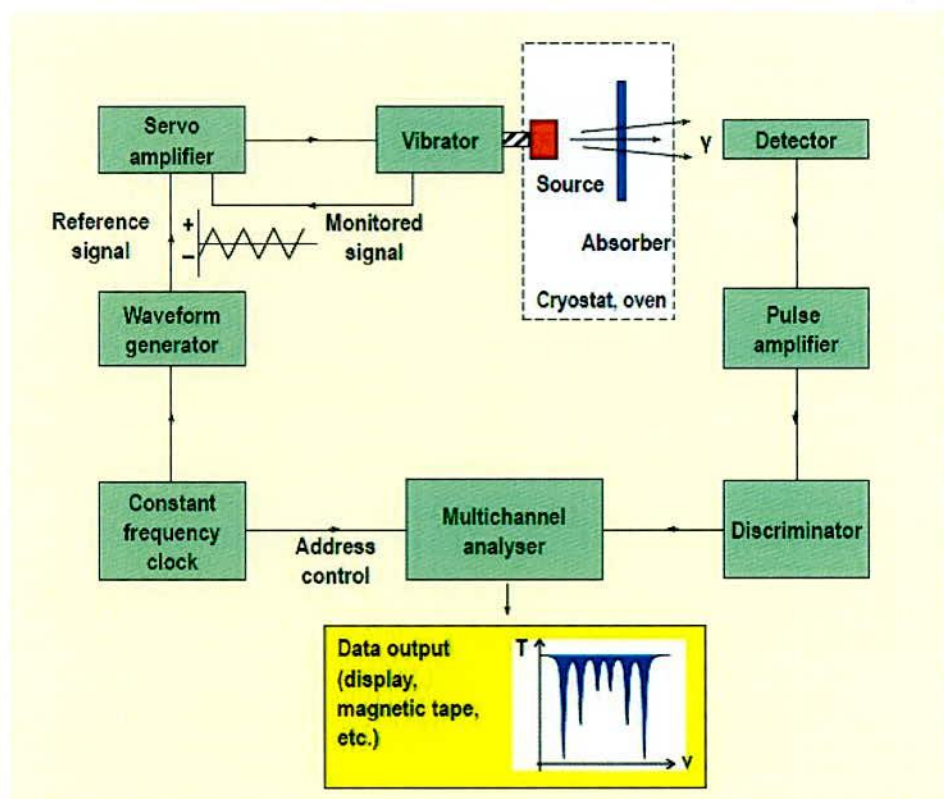


Fig. 3.14 Scheme of Mössbauer Spectroscopy

The detector counts and source velocity are synchronized by a micro processor system. The counts accumulate in 576 channels for one complete cycle which contain two complete spectra; one for positive acceleration and one for negative acceleration of the source. As the acceleration is constant the time interval is equal for all velocity intervals hence each channel records for the same amount of time. During analysis the full spectrum is folded around a central point to produce a single spectrum. This increases the number of counts (and hence gives better statistics) and flattens the background profile produced by the difference intensity of the source radiation as the source move relative to the absorber and detector. The experimental apparatus is drawn in Fig. 3.14. A radioactive FeCo source is mounted on a vibrating shaft that moves in the direction of a Geiger Mueller tube (detector). An absorber placed between the source and the detector may limit the number of  $\gamma$ -rays that reach the detector. Several pieces of electronic equipment are used to control the motion of the source and correlate it with the signal from the detector.





**Fig. 3.15** Sample preparations for Mossbauer measurement



**Fig. 3.16** SEE Co. MS4 Spectrometer recording a Mossbauer spectrum

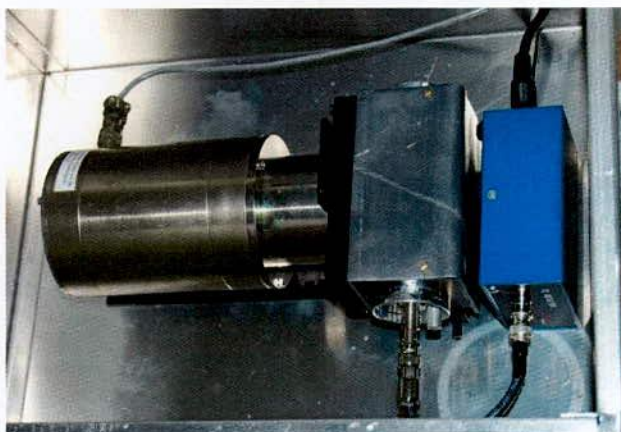


**Fig. 3.17** Velocity Transducer with the sample at room temperature

### **3.7 Nuclear Magnetic Resonance Spectroscopy**

Felix Bloch and Edward Mills Purcell, Nuclear Magnetic Resonance (NMR), has grown to be one of the major tools for scientists to obtain information about the structure and dynamics of molecules with atomic resolution. NMR spectroscopy has been widely used for many applications ranging from mineralogy, physics, materials science, and inorganic chemistry through organic chemistry and polymer research to analysis of proteins and nucleic acids in relation to molecular biology and medicine. By using NMR spectroscopy one can obtain qualitative and quantitative information about chemical species. After its discovery, there have been a significant number of enabling developments that have expanded applications for nuclear magnetic resonance and greatly improved the efficiency of the technique. Relatively recent advances such as cross-polarization, magic-angle spinning, new probe design, signal receiver hardware configuration and pulse sequence design, multidimensional NMR experiments and many others allow us to solve more complicated structural problems or even obtain other important information, such as molecular dynamics, chemical exchange, molecular binding, screening, etc. Many of these new methods involve the parallel acquisition of spectra via multiple receivers for both small molecules and macromolecules. As compared to a number of other analytical techniques, NMR is definitely 'sensitivity challenged'. The question of sensitivity boils down to whether, it is possible to detect the desired signal above the noise level. Though, it remains a

unique and powerful tool for the structural elucidation of chemical compounds and determination of molecular dynamics.

### 3.7.1 Basic Principle of NMR

Spectroscopy, the study of the interaction between matter and electromagnetic radiation, uses adsorption, scattering, or emission of electromagnetic radiation to analyze atoms and molecules qualitatively and quantitatively. Resulting spectra are obtained by the measurement of radiation intensity as a function of wavelength. Nuclear magnetic resonance, NMR, is a physical phenomenon in which atomic nuclei absorb and re-emit electromagnetic radiation. The resonance transition between magnetic energy levels happens when atomic nuclei are placed in an external magnetic field and then an electromagnetic radiation with specific frequency is applied. An NMR spectrum can be acquired by detecting the absorption signals. Positions, intensities and fine structure of resonance peaks in the resulting spectra are used to determine the structures of molecules and to analyze them quantitatively. The adsorption process in NMR involves atomic nuclei that absorb electromagnetic radiation in the radio-frequency region when placed in an intense external magnetic field.

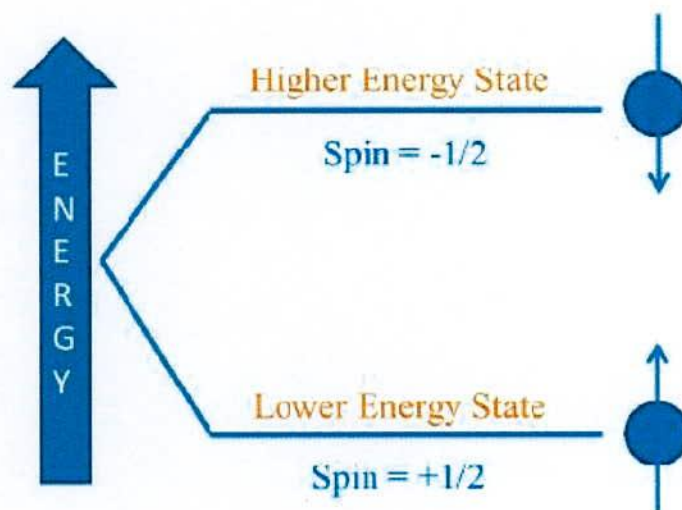
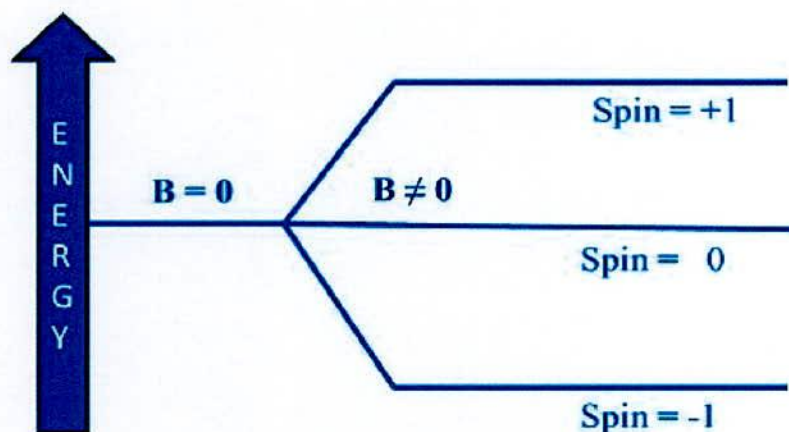


Fig. 3.18 Energy splitting diagram for spin  $I = \frac{1}{2}$  nuclei



When there is an applied magnetic field, the nuclei orient themselves with or against the larger applied field. These different states increase or decrease the effective magnetic field experienced by a nearby nucleus, allowing for two distinct signals. The splitting of nucleic energy levels with a spin  $I=1$  is shown in Fig. 3.19



**Fig. 3.19** Energy splitting diagram for spin  $I=1$  nuclei. There are  $(2I+1)$  possible orientations for each nucleus when external electromagnetic field is applied

The difference in energy between the states,  $E$ , depends on the strength of the applied magnetic field,  $B_0$ , according to the following equation:

$$\Delta E = E_{\frac{1}{2}} - E_{-\frac{1}{2}} = h\nu = \frac{\omega\hbar}{2\pi} \quad (3.25)$$

correspond to the energy that can be absorbed or emitted by the system, described by the Larmor frequency  $\omega$ .

$$\Delta E = \frac{\gamma B_0 \hbar}{2\pi} \quad (3.26)$$

In this equation  $\gamma$  is the gyromagnetic ratio, a fundamental property of each type of nucleus and  $h$  is Planck's constant.

$$\omega_0 = \gamma B_0 \quad (3.27)$$

The Larmor frequency can be understood as the precession frequency of the spins about the axis of the magnetic field  $B_0$ , caused by the magnetic force acting on them

and trying ( $I_z$  is quantized) to turn them completely into the field's direction (like a gyroscope "feeling" the pull of gravity).

### 3.7.2 NMR Signal Processing

The signal in NMR is produced by absorption of electromagnetic radiation of a certain frequency. In the presence of external magnetic field, a nucleus can absorb electromagnetic radiation of the appropriate frequency and undergo a transition between the two energy states. The transitions occur from the lower energy ( $\alpha$ ) to the higher energy ( $\beta$ ) spin states. If the number of nuclei in the lower energy state is equal to the number of nuclei in the higher state, the rate of absorption approaches the rate of relaxation. This process is called saturation. If the relaxation rate is fast, then saturation is reduced. In NMR, the difference in energy in the two spin states is very small therefore the population difference is also small (about 1 in 10,000 for  $^1\text{H}$  in an 11.74 T magnetic field). The NMR signal is thus proportional to the population difference between the states. NMR is a very sensitive method allowing detection of very small population differences between the energy states. At room temperature, the number of spins in the lower energy level,  $N^\alpha$ , slightly outnumbers the number in the upper level,  $N^\beta$ . According to Boltzmann Statistics

$$\frac{N^\alpha}{N^\beta} = \exp\left(\frac{\Delta E}{K_B T}\right) = \exp\left(\frac{\gamma \hbar B_0}{2\pi K_B T}\right) \quad (3.28)$$

$\Delta E$  is the energy difference between the spin states;  $K_B$  is Boltzmann's constant,  $1.3805 \times 10^{-23}$  J/Kelvin; and  $T$  is the temperature in Kelvin. From this equation one can see that the ratio of the number of spins in the lower energy level and the number in the upper level is temperature dependent. As the temperature decreases, so does the ratio  $\frac{N^\alpha}{N^\beta}$ . As the temperature increases, the ratio approaches one, so  $N^\alpha = N^\beta$

Electrons in a molecule circulating around the nucleus produce a magnetic field which opposes the applied external magnetic field or shields it. The electron density around each nucleus in a molecule varies according to the types of nuclei and bonds in the molecule. The opposing field and therefore the effective field at each nucleus will vary. This is called the chemical shift phenomenon which is reported in

ppm and given the symbol delta,  $\delta$ . By definition, the chemical shift of a nucleus is the difference between the resonance frequency of the nucleus ( $\nu$ ) and a standard ( $\nu_0$ ):

$$\delta = \frac{\nu - \nu_0}{\nu_0} \times 10^6.$$

### 3.7.3 Relaxation Mode

Spin relaxation consists of two processes:

#### 3.7.3.1 Longitudinal relaxation or $T_1$ -recovery

The z component of the proton magnetization is reduced to zero at the excited state. During relaxation it exponentially recovers to its initial value.  $T_1$ -recovery has a time constant  $T_1$  – this is the time at which z component has recovered to 63% of its equilibrium energy. During  $T_1$ -recovery radiated energy is absorbed by nearby structures (spin-to-lattice relaxation).

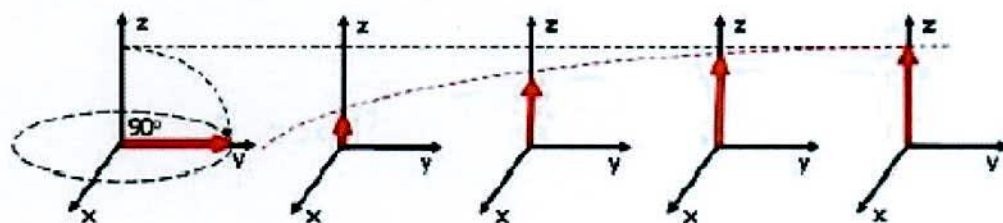


Fig. 3.20  $T_1$  relaxation

#### 3.7.3.2 Transverse relaxation or $T_2$ -decay

The xy plane component has maximum magnetization energy at excited state. During relaxation it loses coherence – dephasing of magnetization vector takes place, and transverse component exponentially decreases till zero.  $T_2$  time constant represents the time, when transversal component has lost 63% of its excited state energy. During  $T_2$ -decay radiated energy is absorbed by nearby spins (spin-to-spin relaxation).





Fig. 3.21 T<sub>2</sub> relaxation

By changing sequences of exciting radiofrequency impulses, image can be formed mainly from T<sub>1</sub> relaxation or T<sub>2</sub> relaxation signals. T<sub>1</sub>-weighted scanning show fat brighter but water darker and is called positive; T<sub>2</sub>-weighted scanning shows reverse – fat darker and water brighter, so called negative. T<sub>1</sub> sequence is more efficient for brain imaging, T<sub>2</sub> for spinal cord diagnostics.

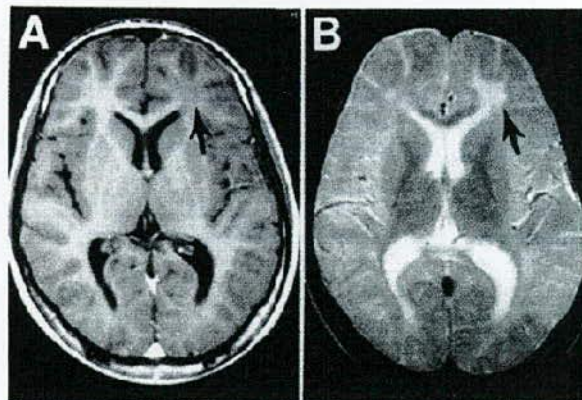


Fig. 3.22 T<sub>1</sub>(A) and T<sub>2</sub>(B) weighted images of human brain

Due to they have their own magnetization, T<sub>1</sub> and T<sub>2</sub> relaxation times of water protons are modified. This enhances a contrast in a specific area where contrast agent is located. MRI signal intensity depends on relaxation rates ( $r_{1,2}$ ) of tissue, which are back-proportional to T<sub>1</sub> and T<sub>2</sub> relaxation times ( $r_1 = \frac{1}{T_1}$  and  $r_2 = \frac{1}{T_2}$ ). Contrast agent is effective, if it significantly changes only one (transverse or longitudinal) relaxation rate.  $\frac{r_2}{r_1}$  ratio of contrast agent determines if it modifies mainly transverse relaxation

rate  $r_2 \left( \frac{r_2}{r_1} \right) > 1$  or longitudinal relaxation rate  $r_1$ ,  $\left( \frac{r_2}{r_1} \right) < 1$ . So contrast agents are classified as  $T_1$  (positive) agents and  $T_2$  (negative) agents. Nowadays commercial contrast agents are satisfying main requirements like stability, safety, bio-distribution, tolerance, etc; but efficiency and quality are poor so actual researches in this field are promising the new generation of high efficiency contrast agents.

### 3.7.4 NMR Instrumentation

There are two NMR spectrometer designs, continuous-wave (CW), and pulsed or Fourier-transform (FT-NMR). In earlier days, primarily continuous wave (CW) experiments were used. This NMR technique can be performed with a constant magnetic field where the frequency is varied. Even though this approach is a valuable tool to look at very sensitive and highly abundant nuclei such as  $^1\text{H}$  and  $^{31}\text{P}$ , it becomes a very challenging task to observe nuclei with low natural abundance such as  $^{13}\text{C}$  or  $^{15}\text{N}$ . Continuous-wave NMR spectrometers have largely been replaced with pulsed FT-NMR instruments because the observed FT-NMR spectra have much higher signal-to-noise ratio and so Fourier-transform is a much more sensitive NMR method compared with CW. Fourier-transform NMR spectrometers use a pulse of radiofrequency (RF) radiation to cause nuclei in a magnetic field to flip into the higher-energy alignment. According to the Heisenberg uncertainty principle, the frequency width of the RF pulse (typically 1- 10  $\mu\text{s}$ ) is wide enough to simultaneously excite nuclei in all local environments when more than one frequency is radiated simultaneously. The nuclei will re-emit RF radiation at their respective resonance frequencies and create an interference pattern in the resulting RF emission as a function of time, defined as free-induction decay (FID). Because the FID results from the emission of nuclei in all environments, each pulse contains an interference pattern from which the complete spectrum can be obtained. Repetitive signals can be summed and averaged that allow to improve the signal-to noise ratio of the resulting FID significantly.

The diagram for a typical FT NMR spectrometer can be seen from Figure 3.20. When a sample is placed in the probe of NMR spectrometer, a radiofrequency (RF) pulse is transmitted by a coil that is surrounds the sample holder. Absorption

takes place when the frequency of the applied magnetic field ( $B_0$ ) resonates with a radiation frequency required for the transition between two energy levels to occur. FID of the resonated frequency can be detected by a RF receiver and Fourier transformed. A resulting NMR spectrum will be obtained and appear on the screen of the computer.

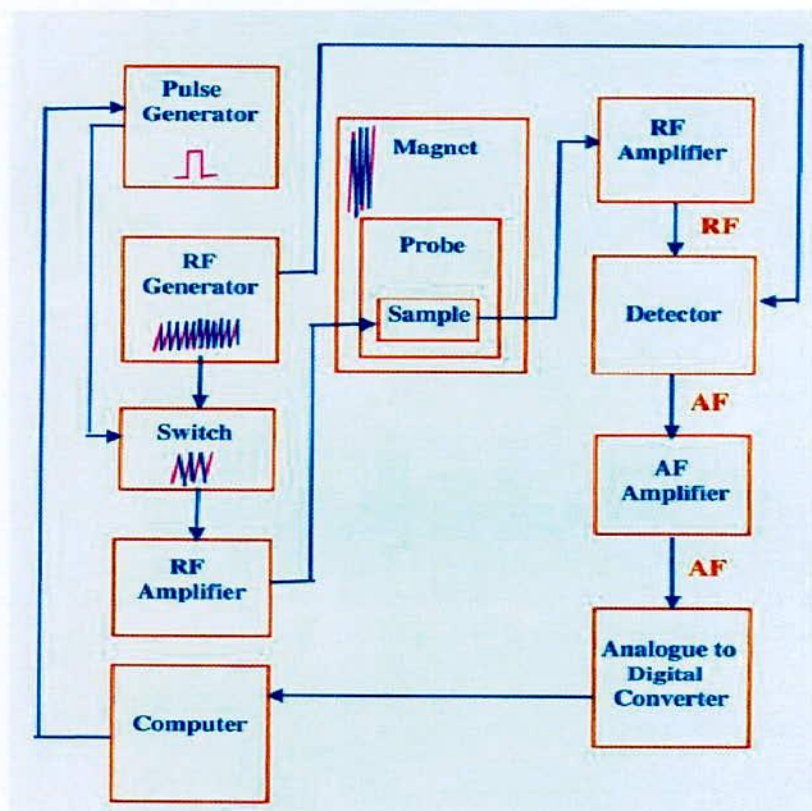


**Fig. 3.23** The diagram of a typical NMR spectrometer

For rare spin NMR, analysis at natural abundance, sensitivity is always a problem. It is even more of a problem in the solid state where spin-lattice relaxation times can be exceptionally long. Indeed, there are numerous reasons to conduct NMR experiments on solids. Some examples would include the cases where chemical compounds are insoluble or unstable in solution. For instance, the process of cross linking to produce an insoluble polymer should be followed as a solid state reaction. The usual approach to this problem is to use solid state NMR technique.



**CHAPTER IV**

**RESULTS AND DISCUSSION**

## RESULTS AND DISCUSSION

### 4.1 Structural Analysis

The prepared Magnesium ferrite samples were examined by XRD in order to determine the crystal structure, lattice parameters and average crystallite size. Figure 4.1 (a, b, c, d, e, f and g) have shown XRD spectra of powder samples annealed at 200, 400, 600, 800, 1000, 1200 and 1400°C respectively. The grain size of ferrites in the different annealed temperature were estimated by using Scherrer's equation.

As would be investigated in Fig.4.1 (a and b) the peak of  $\text{MgFe}_2\text{O}_4$  powder was very good and the many fundamental peaks did not appear. The low intensity indicated that the crystallization of these samples at these annealed temperatures was incomplete with a very small crystallite size. The most intense reflection peak (311) at  $2\theta$  value around  $35^\circ$  was identified in each diffraction pattern of the samples. From the analysis of the XRD which patterns consists of well-resolved peaks, we found that all investigated samples are polycrystalline with single cubic phase in cubic system and the unit cell symmetries can be described by the space groups  $Fd-3m$ , that confirmed the reported yielding of the synthesis route used. This observation matches well with those of earlier reporters [4.1 - 4.5]. The peaks of  $\text{MgFe}_2\text{O}_4$  were detected in all samples without any impurity peaks. No shift in the peaks was observed in any of the samples.

The powders annealed at 600°C shows good crystallinity but relatively broad peak, which also indicated that the  $\text{MgFe}_2\text{O}_4$  crystallization remained incomplete with crystal defects and smaller crystal size. In addition the peak for 800°C was relatively narrow and high which indicates that the crystal grew up with increasing temperature and the crystallization was complete. Further increase in intensity of diffraction peaks indicates that the crystallinity of the samples was improved with increase annealing temperature. The sharp peaks reflect the large grain size. In the other words, the peak sharpness indicates a greater degree of crystallinity. The full width at half maxima (FWHM) value was decreased with an increase in the annealing temperature.

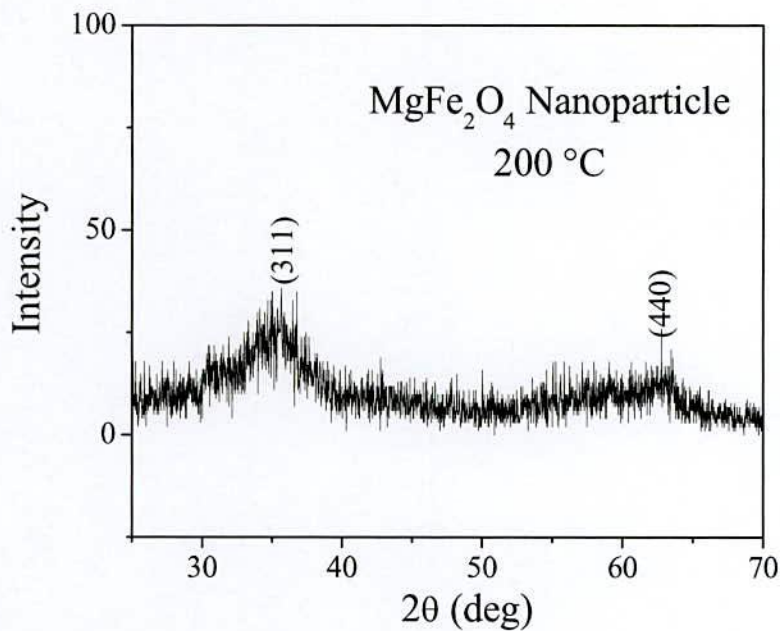


Fig. 4.1 (a) XRD spectra of MgFe<sub>2</sub>O<sub>4</sub> nanoparticles annealed at 200°C

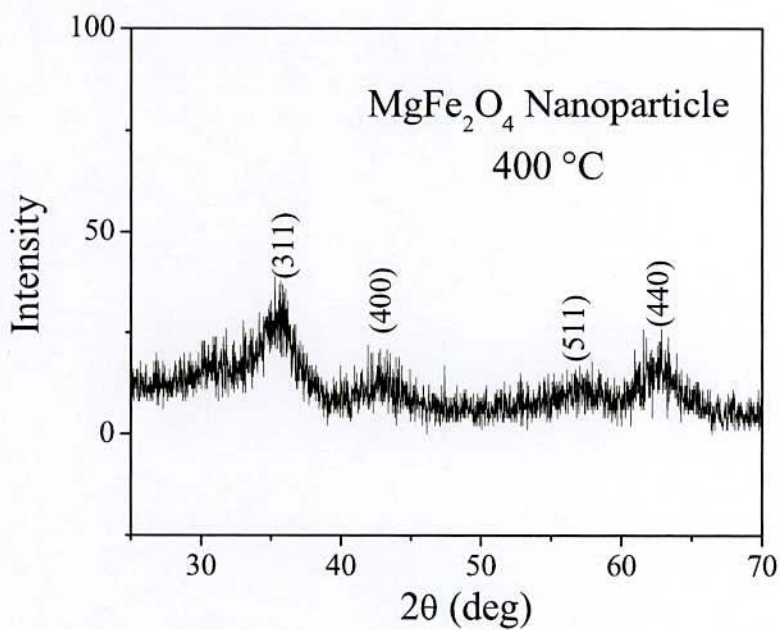


Fig. 4.1 (b) XRD spectra of MgFe<sub>2</sub>O<sub>4</sub> nanoparticles annealed at 400°C



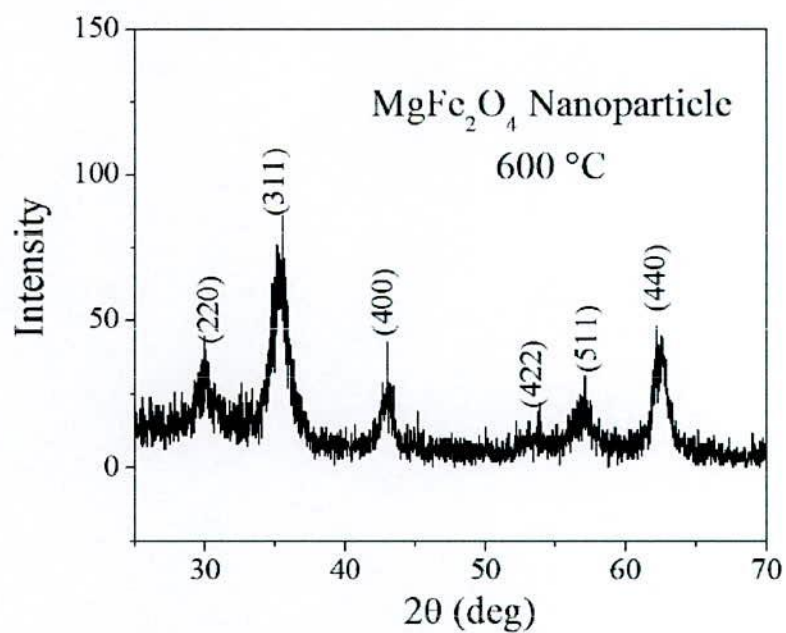


Fig.4.1(c) XRD spectra of MgFe<sub>2</sub>O<sub>4</sub> nanoparticles annealed at 600°C

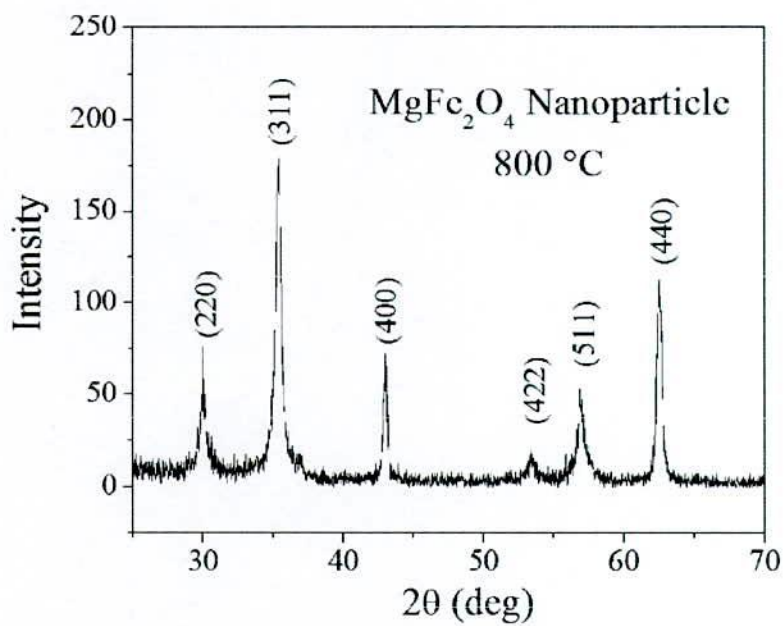


Fig. 4.1(d) XRD spectra of MgFe<sub>2</sub>O<sub>4</sub> nanoparticles annealed at 800°C

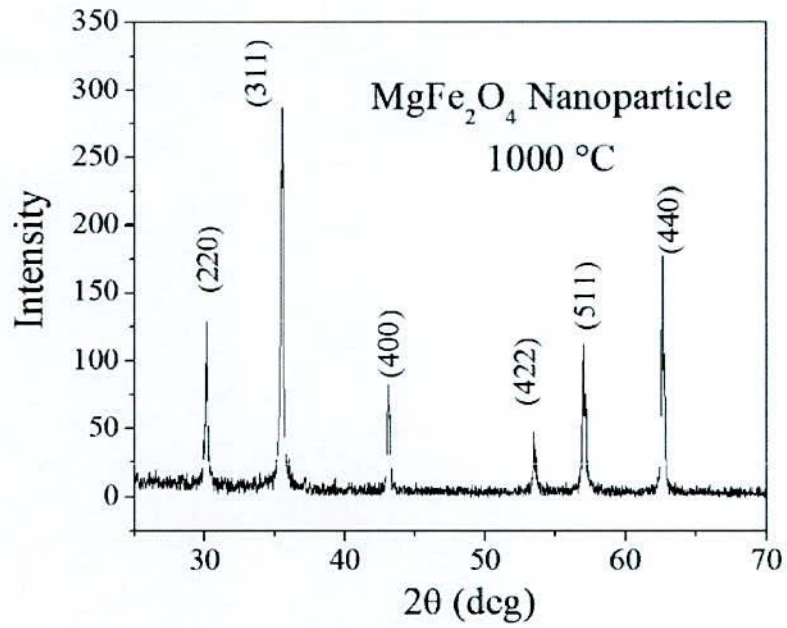


Fig. 4.1(e) XRD spectra of MgFe<sub>2</sub>O<sub>4</sub> nanoparticles annealed at 1000°C

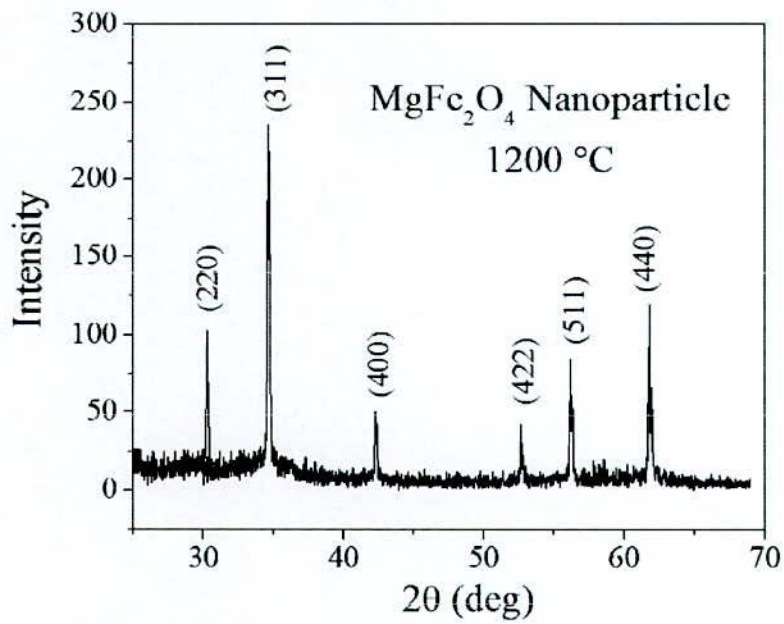


Fig. 4.1(f) XRD spectra of MgFe<sub>2</sub>O<sub>4</sub> nanoparticles annealed at 1200°C

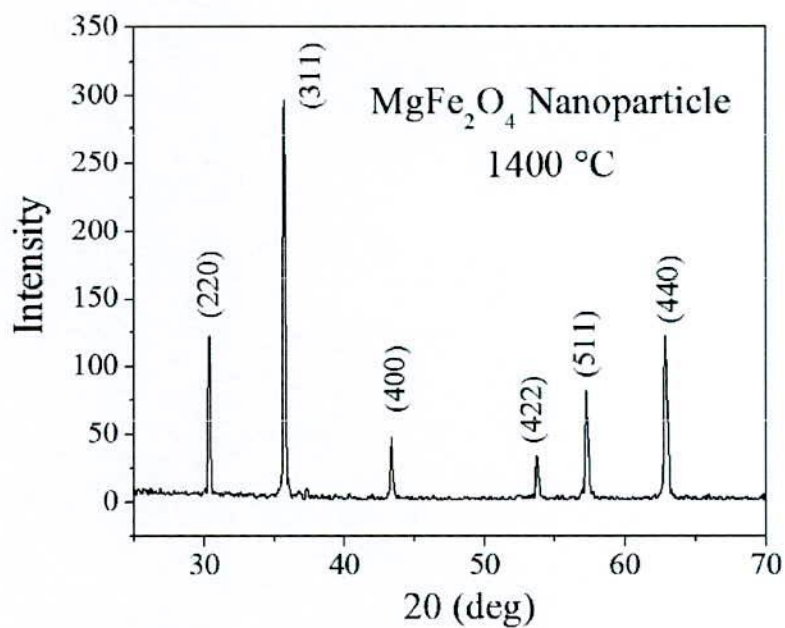


Fig. 4.1(g) XRD spectra of MgFe<sub>2</sub>O<sub>4</sub> nanoparticles annealed at 1400°C

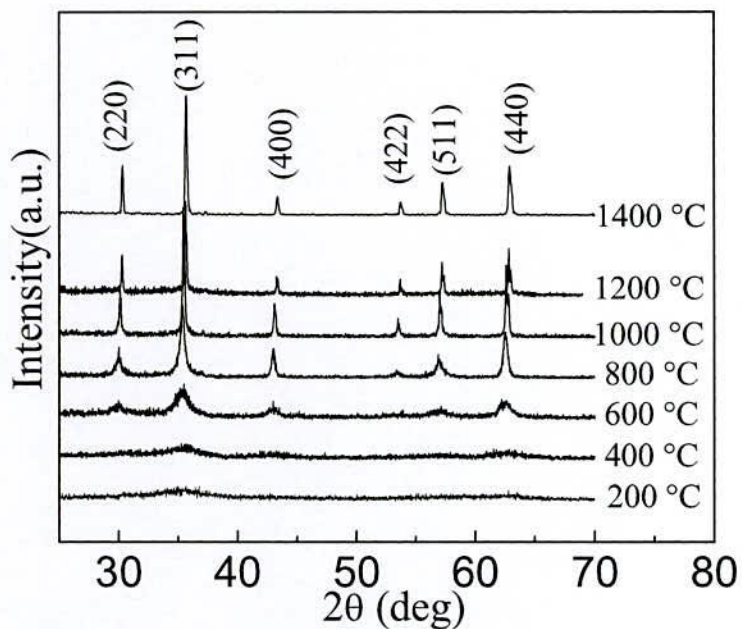
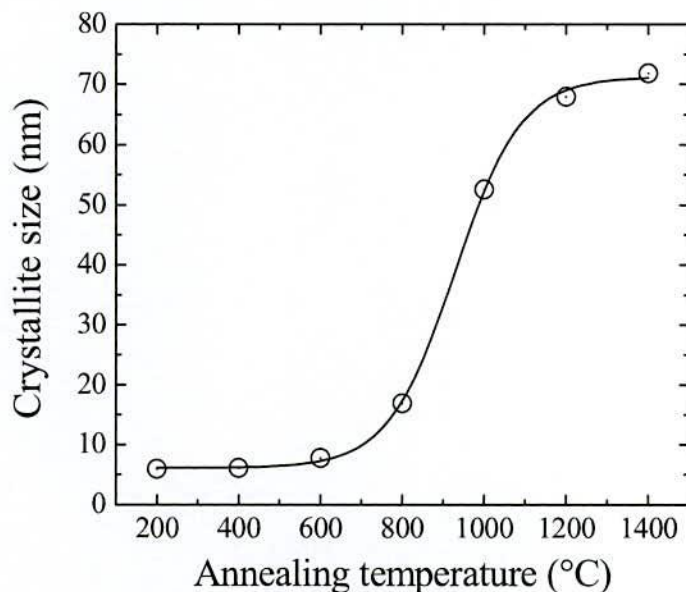


Fig.4.2 Compare the X-ray diffraction patterns of the MgFe<sub>2</sub>O<sub>4</sub> nanoparticles annealed at different temperatures





**Fig.4.3** Variation of crystallite size with different annealing temperature for  $\text{MgFe}_2\text{O}_4$  nanoparticles

The results obtained from XRD patterns of  $\text{MgFe}_2\text{O}_4$  annealed from 800°C to 1400°C have been corresponded to the diffraction peaks (220), (311), (400), (422), (511) and (440) represent that the samples were spinel cubic phase. The reflections also demonstrated the homogeneity of the samples.

Fig.4.3 shows the plots of the average crystallite size of the magnesium ferrite samples for different annealing temperature. Crystal diameter were found to be 5.97, 6.1, 7.79, 16.93, 52.57, 67.97 and 71.86 nm for the samples annealed at 200, 400, 600, 800, 1000, 1200 and 1400°C, respectively. The smallest crystallite size was about 3 nm obtained for as-dried sample while the largest value 71.86 nm was obtained from the highest annealed temperature 1400°C. The crystallite size of the nanoparticles abruptly increased with the annealing temperatures that occur after 600°C. This behavior can be attributed to an increase annealing temperature which provides energy to the crystal growth. These results indicate a strong relationship between crystallite size and annealing temperature.

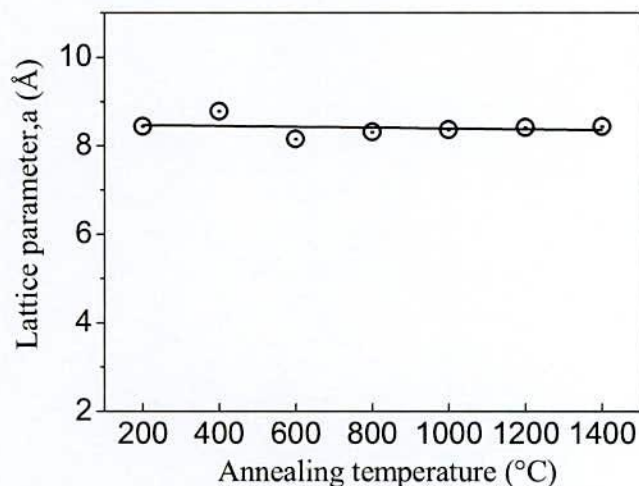


**Fig.4.4** Variation of Lattice parameter with annealing temperature for  $\text{MgFe}_2\text{O}_4$  nanoparticles

The lattice parameters for all samples have been determined from XRD patterns and have shown in Fig.4.4 From this figure, we can clearly see that the lattice parameters were slightly varied with annealing temperature and the values were 8.437, 8.775, 8.152, 8.311, 8.361, 8.413 and 8.434 Å for the samples of magnesium ferrite nanoparticles annealed at 200, 400, 600, 800, 1000, 1200 and 1400°C respectively. Any significant change in lattice parameter has been observed in higher annealing temperature which indicates completion of ferritization.

The crystalline size and lattice parameters are also summarized in Table 4.1 which reveals that the size of magnesium ferrite nanoparticles is sensitive to the temperature of formation. In conventional solid state mixing the corresponding oxides are mixed mechanically at macroscopic scale. However, in our method the constituent salts of precursor were mixed thoroughly to ensure the atomic level of mixing of starting materials and the synthesized precursor shows high reactive activity.

**Table 4.1** Average crystallite size and Lattice parameter of  $\text{MgFe}_2\text{O}_4$  nanoparticles annealed at different temperatures.

<b>Annealing Temperature (°C)</b>	<b>Lattice parameter (Å)</b>	<b>Crystallite size (nm)</b>
200	8.437	5.97
400	8.775	6.1
600	8.152	7.79
800	8.311	16.93
1000	8.361	52.57
1200	8.413	67.97
1400	8.434	71.86



## 4.2 Magnetic Properties

Magnetic properties of these ferrite nanoparticles are of immense interest for the fundamental understanding of magnetic interactions and have great significance owing to their possible applications. The chemical composition and size of the particle play a critical role in determining the magnetic parameters. For as dried samples, the magnetization measurements were made at different temperatures, starting from room temperature 300 K down to 5 K. At each temperature the sample was cooled and the magnetization loop was obtained for the field up to 60 kOe. We have presented hysteresis loops of the sample at temperatures 300 K and 5 K in Fig.4.5. The inset of the figure shows a magnified region around the origin to make the coercivity more visible at low temperature. One of the remarkable features in  $M(H)$  loops is that the magnetization value is high at low temperature but it does not saturate, even at so high applied magnetic field of 60 kOe. This is generally attributed to the canted or disordered spins at the surface of nanoparticles that are difficult to align along the field direction causing an unsaturated magnetization in these particles. In the subsequent discussion, we refer the magnetization at 60 kOe as the saturation magnetization. The increase in magnetization at low temperature may be the result of either of the two reasons. Firstly, it may be due to some extra contribution of the shell-spins moment to the total magnetization at low temperatures thereby increasing the resultant magnetization of the nanoparticles [4.5]. Secondly, such an effect (up turn in magnetization) may be due to the superparamagnetic properties of nanoparticles which would be activated as ferromagnetic properties at low temperatures and at high field (as 60 kOe in our case). These superparamagnetic properties have contribution to the magnetization at 5K that resultantly increases the saturation magnetization of magnesium ferrite as dried samples.

It is observed that compare the room temperature, coercivity was also more high at low temperature than the room temperature.. The reason for the high coercivity at low temperature can be understood by considering the effects of thermal fluctuations of the blocked moment across the anisotropy barrier. It is to be noted that when we were dealing with nanoparticles at low temperature; the anisotropy may be a function of temperature. Thus other factors, apart from the enhancement of anisotropy, like the structural properties that are intrinsic to the nanoparticles, including volume distribution, randomness of anisotropy axes and inter-particle

interactions may also influence the thermal dependence of coercivity in case of nanoparticles [4.6].

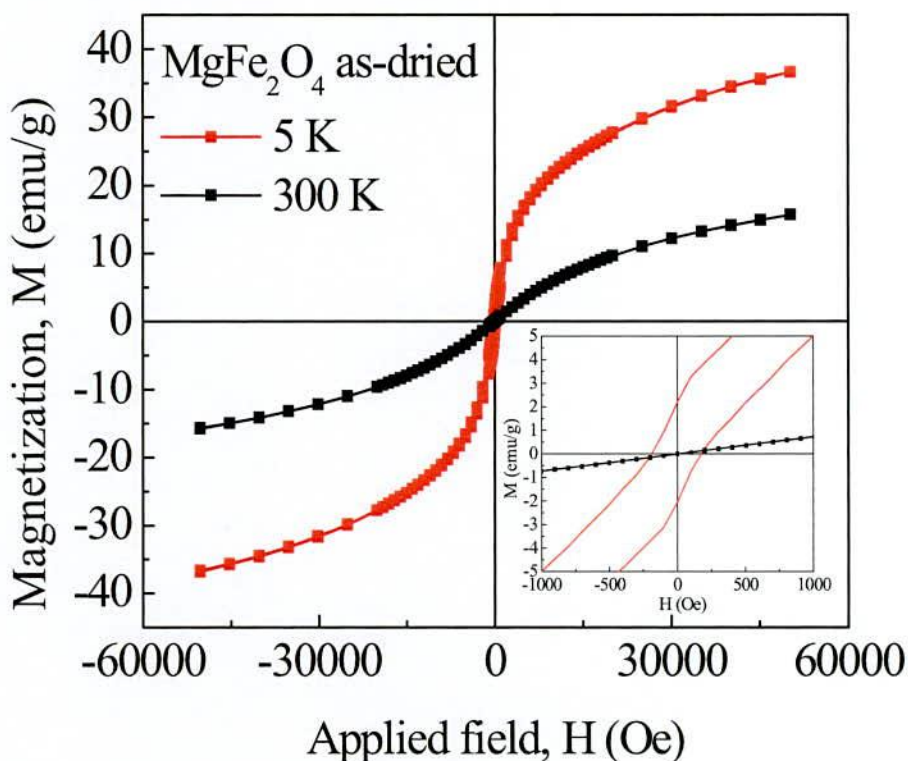


**Fig. 4.5** M (H) loops of MgFe<sub>2</sub>O<sub>4</sub> nanoparticles for as dried sample taken at 300 K and 5K up to maximum field of  $\pm 60$  kOe. The inset of the figure shows the magnified region around the origin to make the coercivity visible for the readers.

#### 4.2.1 Effects of Annealing Temperature on the Magnetic Properties

To understand the magnetic properties for different annealing temperatures and corresponding crystallite size all the samples were characterized using vibrating sample magnetometer (VSM) at room temperature within the applied magnetic field range of -20 to +20 kOe. Magnetic hysteresis loops of the nanoparticles produced at different annealing temperature are shown in Fig.4.6 (a, b, c, d, e, f, g) separately and combine graph have shown in Fig.4.7 with the expand graphs of origin region of hysteresis curve in the range of approximately -1000 to +1000 Oe are shown in Fig.4.8.

It has been seen that all investigated compounds produce a very narrow hysteresis cycle, which indicate that the samples were considered as soft ferrimagnetic materials while specific magnetization increase with increasing applied field and tends to saturate in the field range investigated. The saturation magnetization values ( $M_s$ ) and coercivity ( $H_c$ ) values of the nanoparticles were calculated from the hysteresis curve are shown in Fig.4.10 and Fig.4.11 respectively.

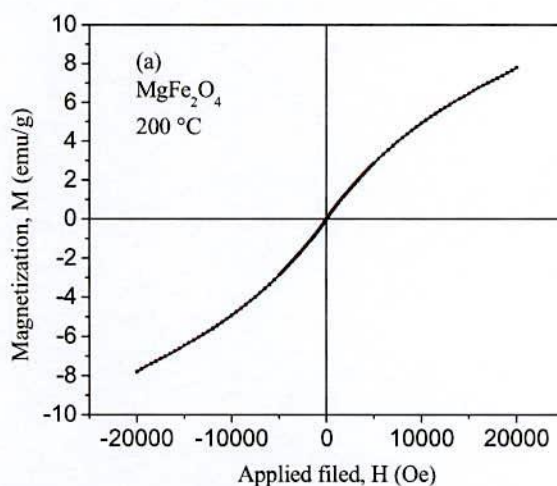


**Fig. 4.6 (a)** M-H loop of MgFe<sub>2</sub>O<sub>4</sub> nanoparticles annealed at 200°C

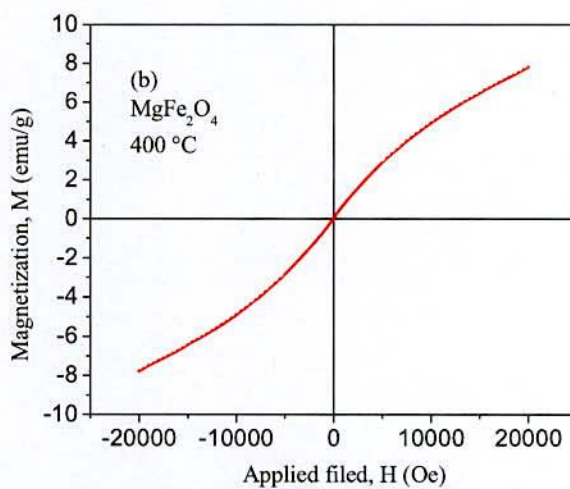


**Fig. 4.6 (b)** M-H loop of MgFe<sub>2</sub>O<sub>4</sub> nanoparticles annealed at 400°C



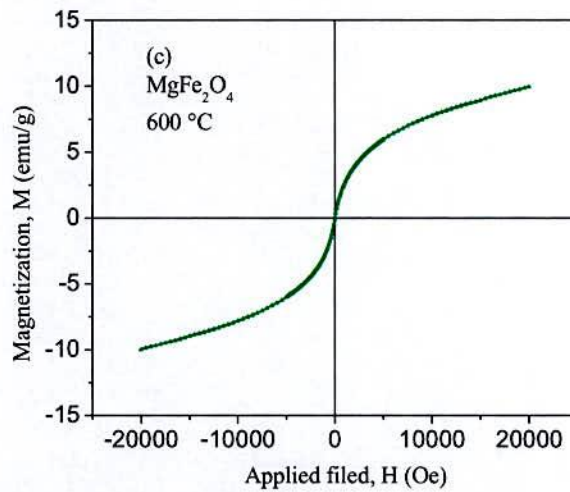


**Fig. 4.7(c)** M-H loop of MgFe<sub>2</sub>O<sub>4</sub> nanoparticles annealed at 600°C

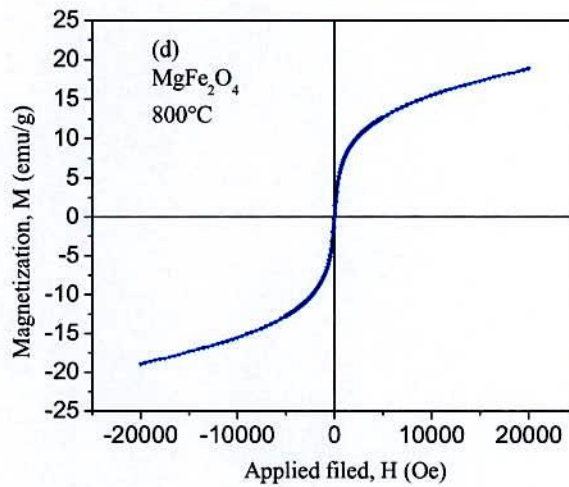


**Fig. 4.6 (d)** M-H loop of MgFe<sub>2</sub>O<sub>4</sub> nanoparticles annealed at 800°C

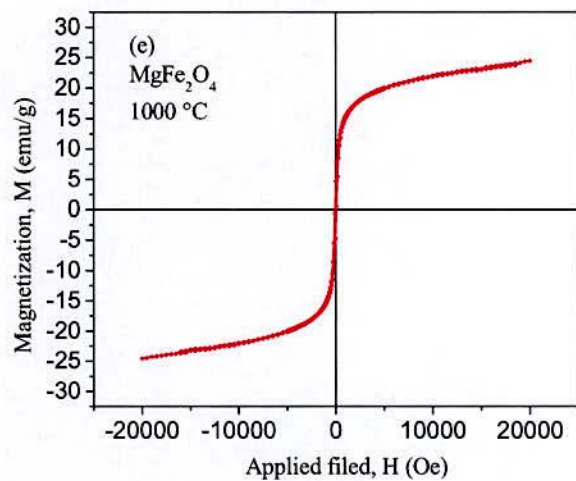


Fig. 4.6 (e) M-H loop of  $\text{MgFe}_2\text{O}_4$  nanoparticles annealed at 1000°C

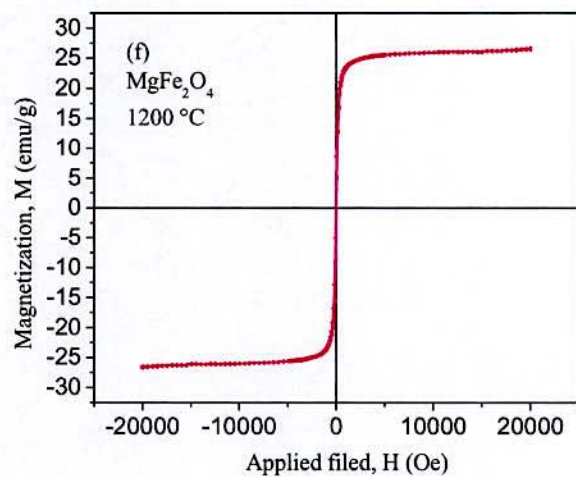


Fig. 4.6 (f) M-H loop of  $\text{MgFe}_2\text{O}_4$  nanoparticles annealed at 1200°C

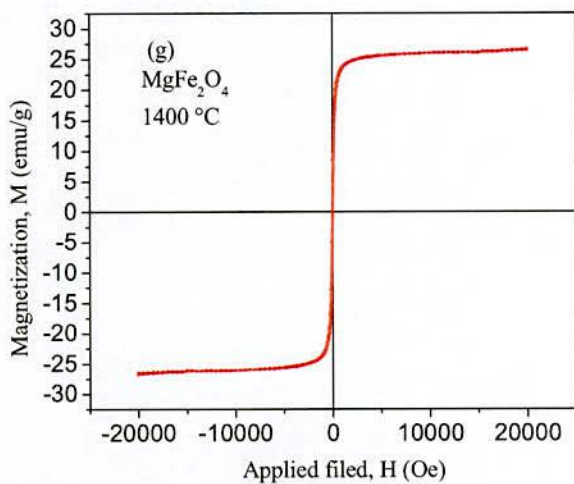


Fig. 4.7(g) M-H loop of MgFe<sub>2</sub>O<sub>4</sub> nanoparticles annealed at 1400°C.

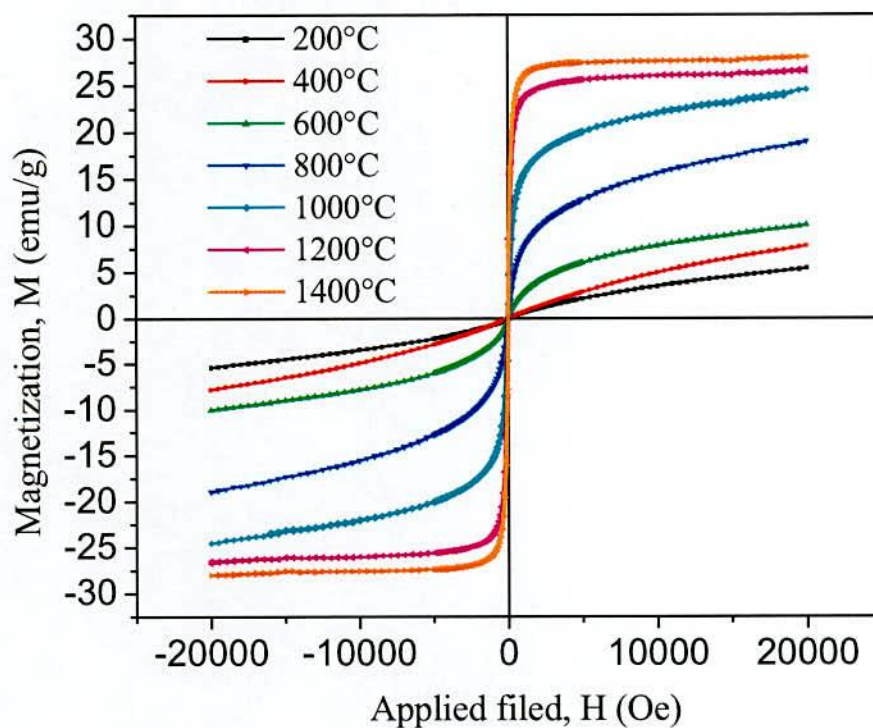
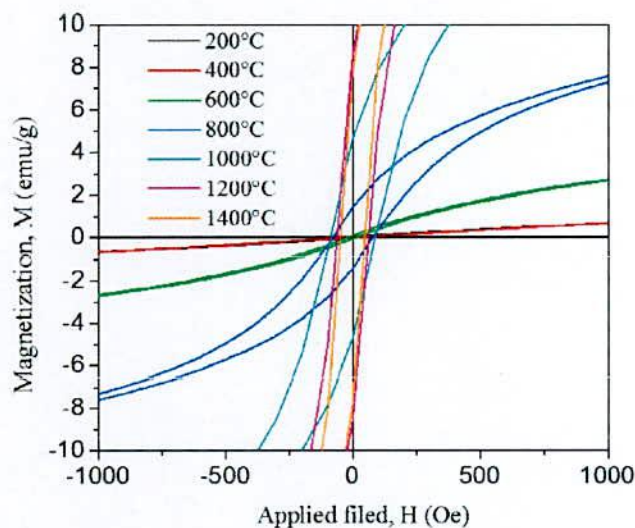


Fig.4.7 Compare of M-H loops with annealing temperature magnesium ferrite samples at room temperature





**Fig. 4.8** The expand graphs of origin region of hysteresis curve in the range of approximately -1000 to +1000 Oe

It is well known that the magnetic properties of nanocrystals are predominantly dictated by the intrinsic properties of materials such as the anisotropy and saturation magnetization. According to these results, it is possible to observe the relationship between annealing temperature and saturation magnetization. It has been seen that the specific magnetization of sample annealed at 200°C is much smaller as compared to other samples. This is attributed to its poor crystallization and relatively small grain size. This fact may be associated with the crystallite size and surface to volume ratio. The specific saturated magnetization value of sample annealed at 1400°C has a higher crystallite size and showed a higher magnetic moment compared to the other samples. This is about 27.96 emu/g (Table 4.2) which is lower than that of bulk Mg ferrite value which was about 33.4 emu/g [4.7]. This may be due to its high degree of crystallization and uniform morphologies. Surface effects can lead to a decrease of the magnetization of all small particles with respect to the bulk value. This reduction has been associated with different mechanisms such as the existence of a magnetically disordered layer on the nanoparticles surface or the existence of spin glass like behavior of the surface spins [4.8]. The existence of some degree of spin canting in the whole volume of the particle in addition to the disordered surface layer

could be an alternative explanation of this additional decrease of the saturation magnetization. In fact the surfaces distortion of the nanoparticles due to the interaction of transition metal ions with the oxygen atoms in the spinel lattice can reduce the net magnetic moment in the particles due to their large surface to volume ratio. In nanoparticles inter ionic separation may face an extension due to less number of structural matters in the surrounding of each particles [4.1]. Thus the nano size of the ferrite particles and ultimate change of the nature of ions in the respective size could have caused reduction of magnetization in magnesium ferrite nanoparticles.

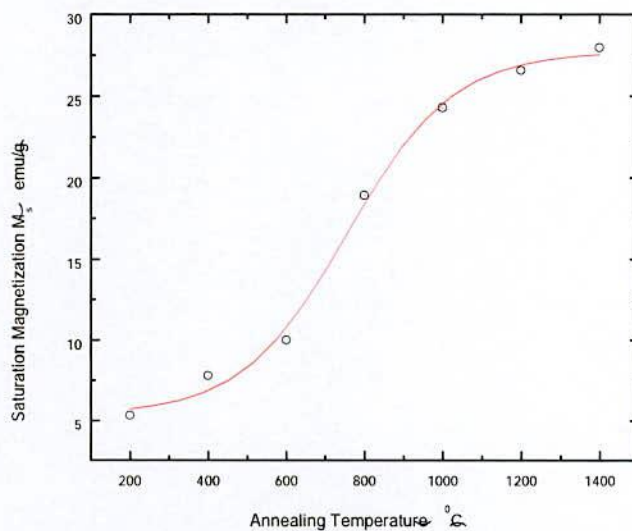


**Fig. 4.9** Variation of saturation magnetization with annealing temperature of produced samples

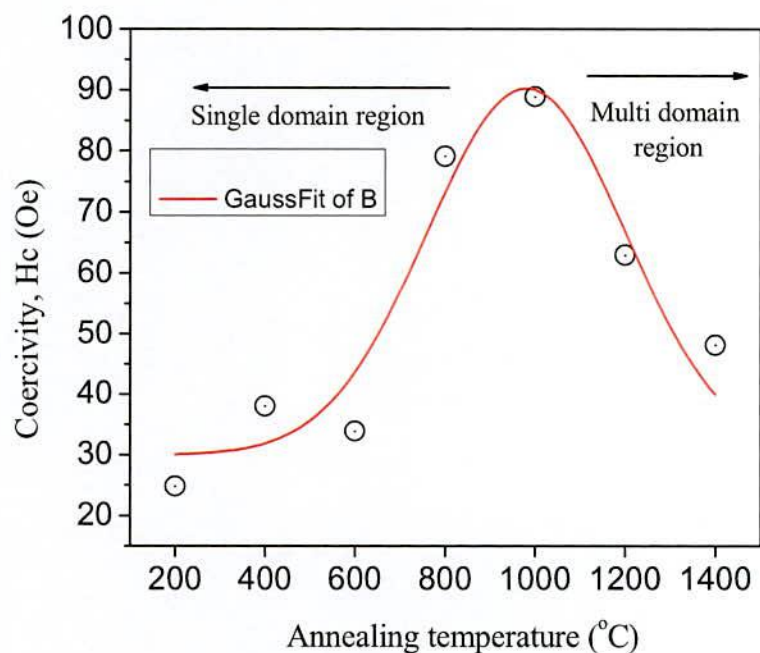


**Fig. 4.10** The correlation between the coercivity and the annealing temperature of magnesium ferrite nanoparticles

The difference between the values that have been found for saturated magnetization in the samples may be attributed to the distribution of cations in the structure which could be associated with temperature. It is found that the increase in the crystallinity and the values of saturation magnetization for the magnesium ferrite samples were observed to increase with increasing grain size. This type of behavior is entirely consistent with a model of crystal growth in such a way that the difference in the magnetic parameters is associated with the change in crystallite size. The variation of saturation magnetization with annealing temperature can be due to cation inversion which originates from nanoparticles fabrication. Due to nanoparticles formation some of the  $\text{Fe}^{3+}$  cations transferred from the B site to the A site and the same number of  $\text{Mg}^{2+}$  ions migrated from A sites to B site increasing the accumulation of  $\text{Fe}^{3+}$  ions at the A site and  $\text{Mg}^{2+}$  ions at the B site. However, the  $\text{Fe}_A^{3+} - \text{Fe}_B^{3+}$  super exchange interactions increased and this can lead to an increase in saturation magnetization in the magnesium ferrite nanoparticles. Inter sub lattice, super exchange interactions of



the cations on the A - B are much stronger than the A - A and B - B intra sub lattice exchange interactions [4.9]. The external parts of the nanoparticles seems to be composed of some distorted or canted spins that prevent the core spins from aligning with the direction of the field consequently the saturation magnetization increase for larger sizes and decrease for smaller sizes.

The coercivity of a magnetic material is usually a measure of its magneto-crystalline anisotropy. It is also seen from this Fig.4.10 that coercivity values of the nanoparticles have been increases with the increase in temperature. The nanoparticles prepared at low annealing temperatures have very small coercivity values. These samples showed the superparamagnetic behavior. In contrast to this situation, the samples begin to show ferromagnetic behavior with the increased annealing temperature. As a result, as expected the coercive force increased until it reached a maximum value and then began to diminish. In other words, it was observed that the samples passed from superparamagnetic behavior to paramagnetic or ferromagnetic behavior with the increase in the average particle size of samples due to the increase in annealing temperature.

It is known that the variation of coercivity with particle size can be explained on the basis of domain structure, critical diameter and the anisotropy of the crystal [4.10]. It is explained that nano ferrite particles having nanometer dimension are considered to have single domains. However, smaller coercive field is normally assumed to be caused by multi domains for bulk particles, in nano regime there is a change over from multi domain nature to single domain nature. The higher value of coercivity of nanoparticles is attributed to the demagnetization caused by domain rotation single domain which requires greater energy rather than the movement of walls (multi domain) [4.11]. Thus the increase in coercivity of nano magnesium ferrite compared with its bulk counterpart can be attributed to the impact of nano regime.

**Table: 4.2** Saturation magnetization  $M_s$ , Coercivity  $H_c$ , measured by VSM technique at room temperature for  $MgFe_2O_4$  nanoparticles produced at different annealing temperatures.

<b>Annealing Temperature (°C)</b>	<b>Coercivity <math>H_c</math> (Oe)</b>	<b>Saturation magnetization (emu/g)</b>
200	24.8	5.32
400	38.0	7.78
600	33.9	9.98
800	79.1	18.92
1000	88.9	24.3
1200	63.0	26.56
1400	48.14	27.96

### 4.3 Mössbauer Study

The continuous improvement of computation capabilities for spectral analyses and the introduction of sophisticated software for the treatment of Mössbauer data has enabled researchers to obtain rich and valuable information from the Mössbauer experiments as well as to study the structure of with higher accuracy and from complementary points of view. The superparamagnetic behavior in magnetic nanoparticles is indicated by the presence of a blocking behavior, characterized by a blocking temperature which marks the transition of the system to a superparamagnetic state. In the case of Mössbauer measurements we investigate the change in the spectrum as a function of temperature, where the onset of superparamagnetism is marked by a change in the Mössbauer pattern from a sextet to a doublet.

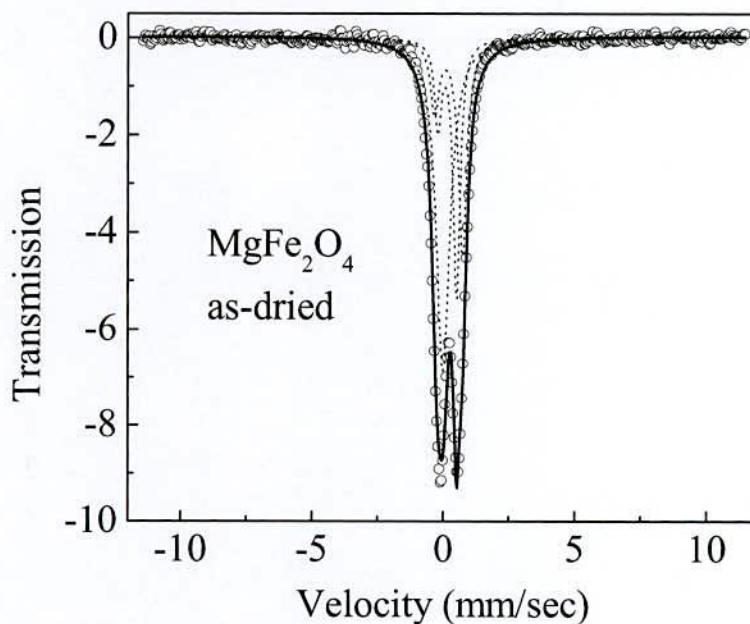
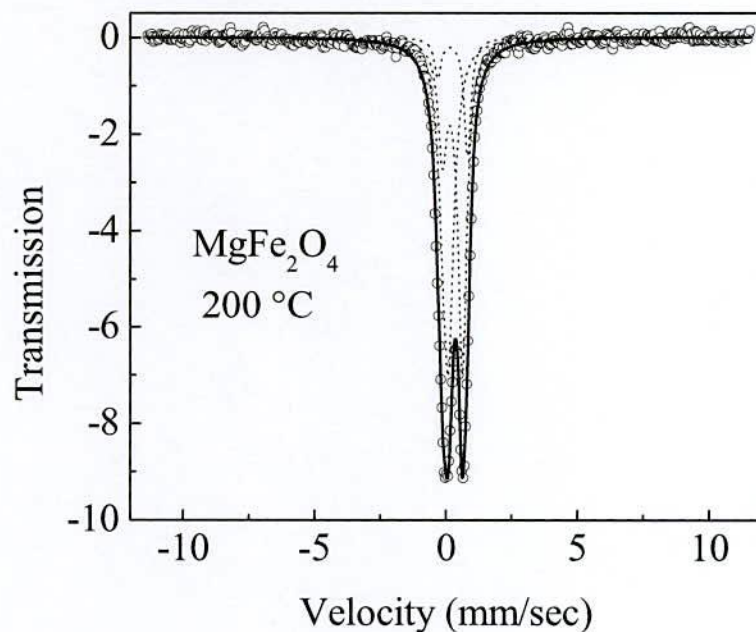


Fig. 4.11(a) Mössbauer spectra of as-dried MgFe<sub>2</sub>O<sub>4</sub> nanoparticles



Mössbauer measurements were performed at room temperature for all the samples. The Fig.4.11(a) have shown the Mössbauer spectra of  $\text{MgFe}_2\text{O}_4$  in as-dried condition and after annealing at 200,400,600,800,1000,1200 and 1400°C, the spectra have shown in Fig.4.11(b, c, d, e, f, g and h), respectively. The fitting of spectral lines were performed assuming Lorentzian absorption line shapes using the Mössbauer spectral fitting software WMOSS by web research. In which allows for fitting to a continuous distribution. In the figures shown below, the outer sextets corresponds to  $\text{Fe}^{3+}$  ions in octahedral position and the inner sextets correspond to  $\text{Fe}^{3+}$  ions in tetrahedral position. From these figures it was observed that with increasing particle size, the peaks become sharper. This is because with increasing particle size, the surface area decreases, grain boundaries become smaller and the energy distribution decreases. And as a result the peaks become sharper.



**Fig. 4.11(b)** Mössbauer spectra of  $\text{MgFe}_2\text{O}_4$  nanoparticles annealed at 200°C

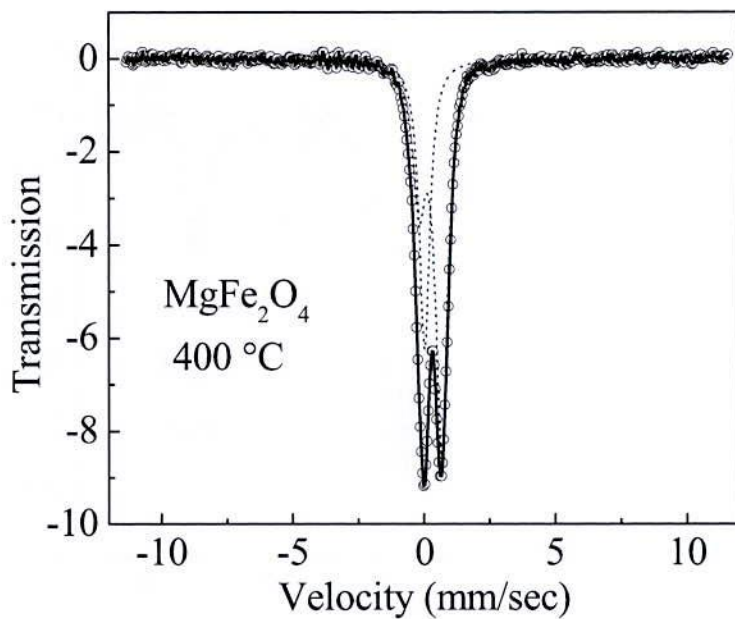


Fig. 4.11(c) Mössbauer spectra of  $\text{MgFe}_2\text{O}_4$  nanoparticles annealed at  $400^\circ\text{C}$

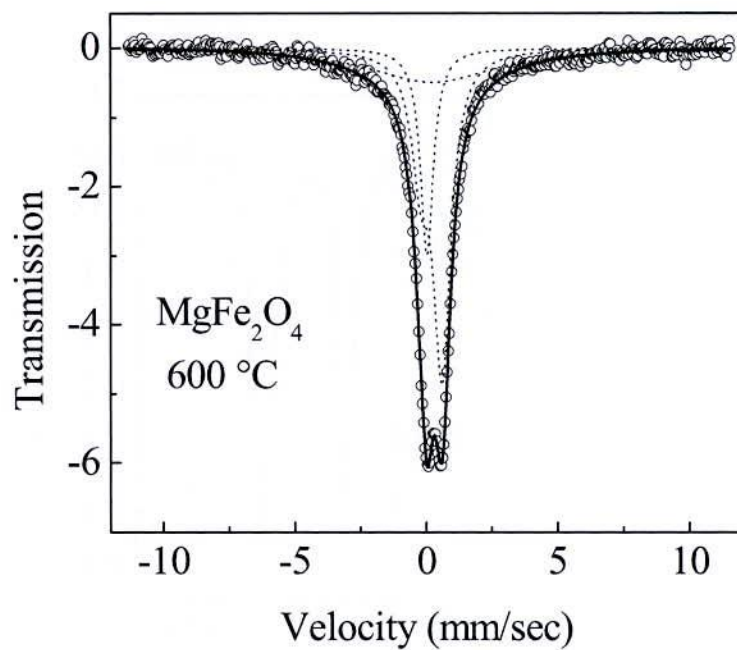


Fig. 4.12(d) Mössbauer spectra of  $\text{MgFe}_2\text{O}_4$  nanoparticles annealed at  $600^\circ\text{C}$

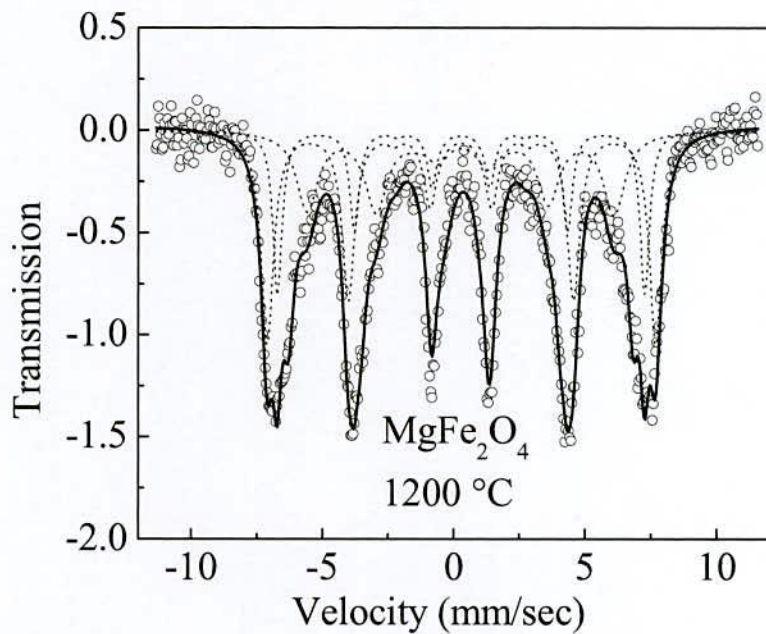


Fig. 4.11(g) Mössbauer spectra of  $\text{MgFe}_2\text{O}_4$  nanoparticles annealed at  $1200^\circ\text{C}$

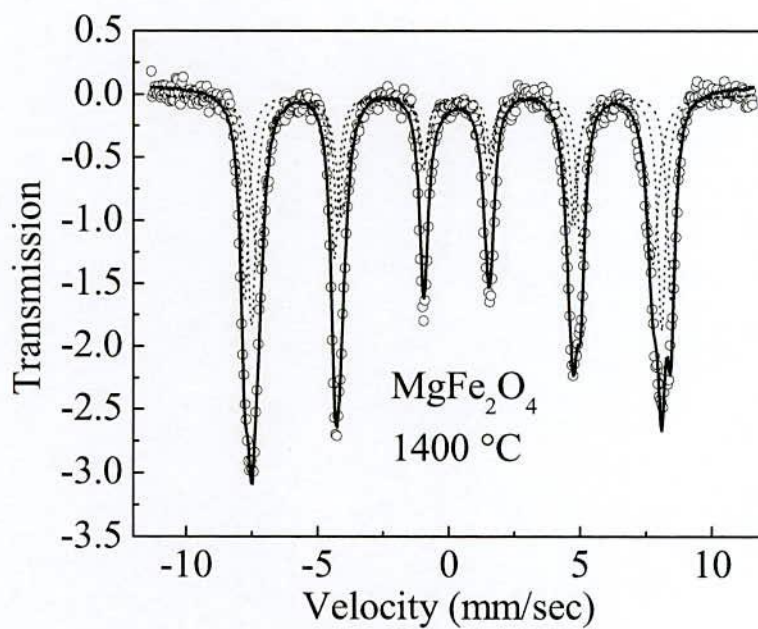


Fig. 4.11(h) Mössbauer spectra of  $\text{MgFe}_2\text{O}_4$  nanoparticles annealed at  $1400^\circ\text{C}$



It has been observed that doublet pattern gradually changes to sextet pattern as the annealing temperature increase, i.e. the nano-ensembles undergo a transition from superparamagnetic state ferromagnetic state. In Fig. 4.11(b), 4.11(c) and 4.11(d) which correspond to the as-dried sample and the sample annealed at 200, 400 and 600°C, respectively, a prominent doublet was observed at the center of spectra. The doublet pattern arises from the relaxation of the Fe in magnesium ferrite, which has a relaxation time  $\tau$  less than  $\tau_L$ , which is the Larmor precession time of the nuclear magnetic moment. The doublet pattern indicates superparamagnetic behavior of the smaller sized particles. The sextet pattern in the background is attributed to the larger sized particles. Fig.4.11 (e) for the sample annealed at 800°C shows a very weak doublet along with sextet pattern or medium relaxation. The doublet pattern occurs due to the interaction of gamma ray with the electric field of the electrons of the sample. The sextet pattern arises due to the interaction of gamma ray with the magnetic field of the sample. Thus appearance of sextet indicates presence of internal magnetic fields which is one significant characteristic of ferromagnetic materials.

It can be observed that the transition from superparamagnetic to ferromagnetic took place at 800°C. At 1000°C magnesium ferrite becomes ferromagnetic. For the application in magnetic particle hyperthermia the nanoparticles should be in superparamagnetic state. Thus from the above Mössbauer spectra it can be concluded that magnesium ferrite nanoparticles annealed up to 800°C would be most suitable for applications in magnetic particle hyperthermia.

The spectral parameters such as isomer shift (IS), quadrupole splitting ( $\Delta E_q$ ) and hyperfine field ( $H_{hf}$ ) are computed and summarized in Table 4.3. The isomer shifts in this table is quoted relative to metallic iron at room temperature. The quadruple splitting in the superparamagnetic component indicates distorted coordination away from the perfect tetrahedral or octahedral symmetry. From the table we can observe that up to 600°C there is no hyperfine field, i.e. the sample is in super paramagnetic state. At 800°C two of the sub site positions have no hyperfine field and three of them have very little hyperfine field. Thus it has slight ferromagnetic character but the superparamagnetism is dominating.

**Table: 4.3** Numerical values of Isomer shift (IS), Quadrupole Splitting ( $\Delta E_q$ ), Position of  $Fe^{3+}$ , Hyperfine field ( $H_{hf}$ ) of  $MgFe_2O_4$  nano particles annealed at different temperatures

$MgFe_2O_4$	Sub site	Position of $Fe^{3+}$	Isomer Shift (IS) mm/sec	Quadrupole splitting ( $\Delta E_q$ ) mm/sec	Hyperfine field ( $H_{hf}$ ) KG	Area
As-dried	1	A	0.207	1.071	0	0.284
	2	B	0.155	0.719	0	0.266
	3	B	0	0	0	0.510
200 °C	1	B	0.255	0.760	0	0.447
	2	A	0.261	1.136	0	0.123
	3	B	0.013	0.221	0	0.452
400 °C	1	B	0.244	0.857	0	0.724
	2	A	0	0.108	0	0.358
600 °C	1	A	0.203	0.814	0	0.573
	2	B	0.238	0.031	0	0.293
	3	B	0.040	0	0	0.209
800 °C	1	B	0.342	0.073	-504.247	0.130
	2	B	0.287	0.548	-477.329	0.309
	3	A	0.431	1.486	-364.324	0.023
	4	A	0.500	1.080	-439.608	0.230
	5	B	0.323	0.604	0	0.306
1000 °C	1	B	0.343	0.372	-503.996	0.123
	2	A	0.500	1.123	-439.348	0.022
	3	B	0.339	0.496	-374.391	0.193
	4	B	0.288	0.476	-477.749	0.319
	5	A	0.322	0.605	0	0.395
1200 °C	1	A	0.277	0	-435.220	0.184
	2	B	0.283	0.019	-460.228	0.358
	3	A	0.290	1.166	-356.881	0.244
	4	B	0.275	0	-408.867	0.234
	5	A	0.480	1.500	0	0.043
1400 °C	1	B	0.317	0.033	-497.265	0.270
	2	B	0.351	0.278	-510.588	0.157
	3	B	0.263	0.482	-463.505	0.326
	4	A	0.275	0.642	-480.000	0.367
	5	A	0.500	1.500	0	0.028



At 1000°C (Fig.4.11 (f)), the material has significant hyperfine field, indicating that it has now become ferromagnetic. From the above Table we also find the Fe distribution at tetrahedral (A) and octahedral (B) sites. The determined Fe site population of MgFe<sub>2</sub>O<sub>4</sub> in as-dried condition for tetrahedral (A) and octahedral (B) site is 28.4% and 77.6% respectively.

#### **4.4 NMR Study of Coated Magnesium Ferrite**

In the recent years, ferrite nanoparticles have emerged as an MRI contrast agents among the several areas in the field of biomedical applications [4.12 - 4.13]. Contrast agents within a physiological system function through a mechanism called relaxation. Hydrogen protons of water molecules undergo relaxation after the excitation of protons with an external magnetic field. Under the application of high DC magnetic field, spins of the proton magnetic moments precess about the direction of the magnetic field at Larmor frequency. When an AC exciting field of Larmor frequency is applied on the precessing moment of the proton, the moments are perturbed. The moments return to their thermodynamic equilibrium through couple of relaxation processes. These are spin-lattice, T<sub>1</sub> relaxation in which energy is transferred from the spin to its surrounding environment, i.e., lattice and spin-spin, T<sub>2</sub> relaxation in which relaxation is achieved through de-phasing of magnetic moment. In this process, contrast agents themselves do not generate any signals, yet they contribute to create local field inhomogeneity, which arise from the susceptibility difference of different elements in the proximity of the particles within a voxel because of the difference in the uptake of different elements in the body. This shortens T<sub>2</sub> relaxation time because of the creation of greater local field inhomogeneity in the presence of the contrast agent and thus provides an opportunity to acquire T<sub>2</sub> weighted image [4.14].



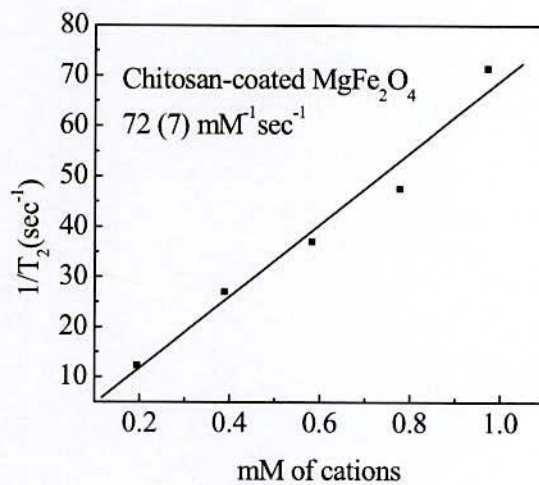


**Fig. 4.12(a)**  $T_2$ relaxivity by NMR spectroscopy  $\text{MgFe}_2\text{O}_4$  coated with Chitosan

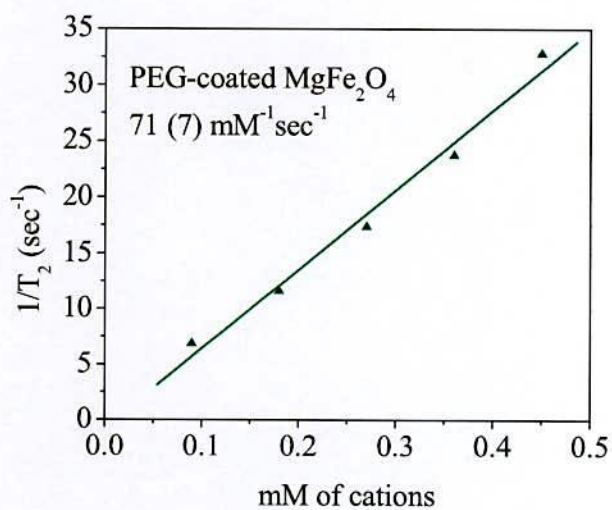


**Fig. 4.12(b)**  $T_2$ relaxivity by NMR spectroscopy  $\text{MgFe}_2\text{O}_4$  coated with PEG

In our present work the  $T_2$  relaxivity values of Chitosan (CS) and Polyethylene-glycole (PEG) coated magnesium ferrite have been measured with nuclear magnetic resonance and are presented in Fig.4.12 as a function of concentration.

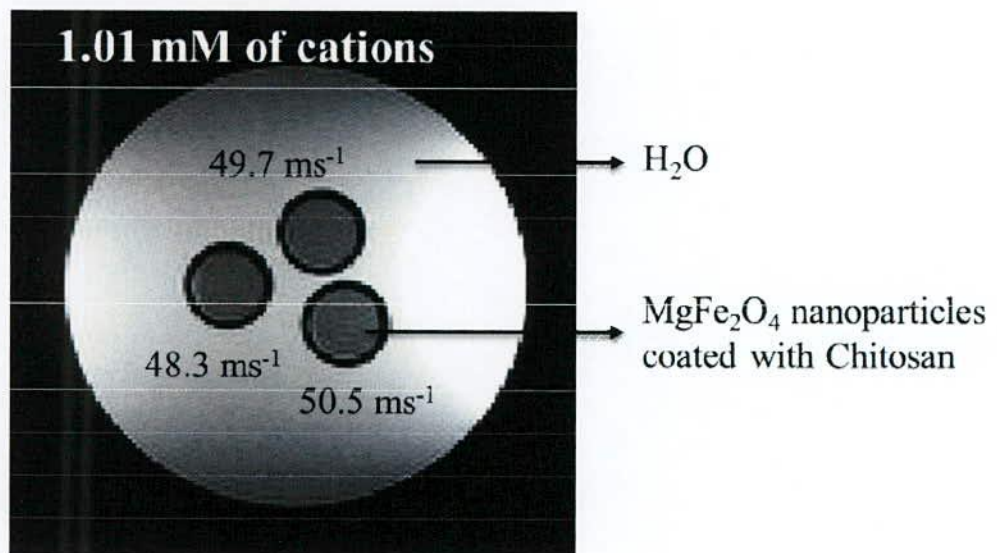
Chitosan is known as an ideal bio-polymetric material, because it has high biocompatibility, disintegration, non-toxicity, and antibacterial and hydrophilic properties [4.15]. Chitosan is a linear polysaccharide composed of randomly distributed  $\beta$ -(1-4)-linked D-glucosamine (deacetylated unit) and N-acetyl-D-glucosamine (acetylated unit). Chitosan's properties also allow it to be used in transdermal drug delivery; it is muco - adhesive in nature, reactive (so it can be produced in many different forms), and most importantly, has a positive charge under acidic conditions. This positive charge comes from proton anion of its free amino groups. The positively charged chitosan coated nanoparticles had a high accessibility to the negatively charged cell membrane. Also, the amino group in the chitosan enhanced the coupling time of particles with issue [4.16]. This means chitosan can be used to transport a drug to an acidic environment.

Polyethylene glycol (PEG) is a polyether compound with many applications from industrial manufacturing to medicine. The structure of PEG is:  $H-(O-CH_2-CH_2)_n-OH$ . PEG is also known as polyethylene oxide or polyoxyethylene, depending on its molecular weight.

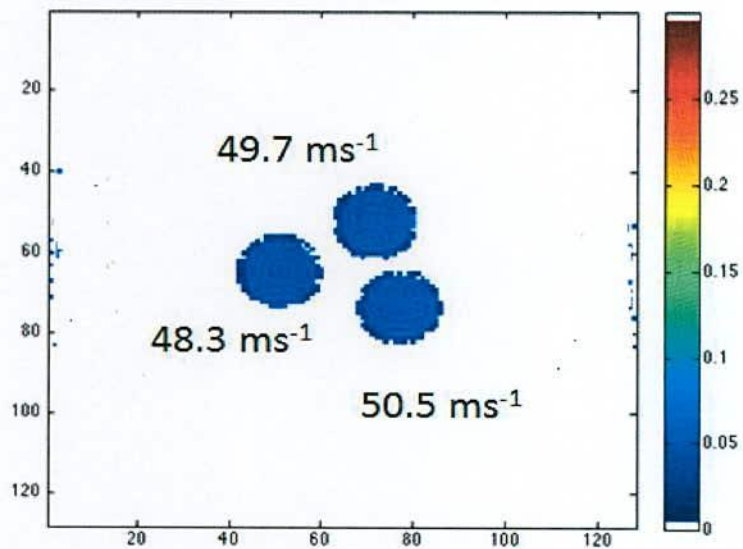
The contrast enhancing efficacy of the synthesized ferrites as contrast agents may be expressed by the following equation [4.16]:

$$\frac{1}{T_2} = \frac{1}{T_{2,0}} + r_2 C$$

Where  $i=2$ ,  $C$  is the concentration of the contrast agent,  $T_2$  is the observed relaxation time in the presence of contrast agent, and  $T_{2,0}$  is the relaxation time in the absence of contrast agent. In the above equation, the co-efficient of contrast agent called relaxivity is a concentration-independent term, and this indicates the strength of the contrast agent. A contrast agent with a large relaxivity value  $r_2$  shortens relaxation time  $T_2$  drastically with a smaller concentration increment. It can be found in the literature that the value of  $r_2$  does not only depend on saturation magnetization but also depends on coating element and particle size and shape [4.17].



(a)



(b)

**Fig.4.13** MRI contrast agent MgFe<sub>2</sub>O<sub>4</sub> (a) coated with chitosan with respect to water (b) respective relaxation measured from these images are quoted



Here we have found a slight difference between the  $r_2$  values of  $\text{MgFe}_2\text{O}_4$  synthesized by the chemical co-precipitation method and coated with Chitosan (CS) and PEG. Different values of  $r_2$  is presented in the following Table.4.4. It indicated that relaxivity varies with coating element.

**Table 4.4** Relaxivity by NMR spectroscopy  $\text{MgFe}_2\text{O}_4$  with the coating of Chitosan (CS), and PEG

$T_2$ relaxivity ( $\text{mM}^{-1}\text{S}^{-1}$ )	Chitosan Coated	Coated with PEG
$r_2$	72( $\pm 6$ )	71( $\pm 3$ )

Hence, magnesium ferrite is suitable for  $T_2$ - weighted image in MRI. The MRI images are presented in the following figure 4.14. The image was obtained in-vitro using phantom which was designed by filling  $\text{MgFe}_2\text{O}_4$  nanoparticle solution of 1.01 mM inside the small tubes which inserted inside the large tube containing water. In Fig.4.13 (a) the light background is water and the dark circles represent nanoparticle solution. The degree of darkening demonstrated that the chitosan coated  $\text{MgFe}_2\text{O}_4$  nanoparticle solution is suitable at  $T_2$  contrast agent. In Fig.4.14 (b) the value of relaxation time  $T_2$  or the relaxation  $r_2 = \frac{1}{T_2}$  has been determined and presented in the figure with scale bar. The average value of  $r_2$  has been obtained as  $\sim 50 \text{ ms}^{-1}$ .

**CHAPTER V**

**CONCLUSIONS**

## CONCLUSIONS

### 5.1 Conclusions

We have verified the tuning on the magnetic properties of the magnesium ferrite nanocrystals by a suitable control of both, composition and crystal size at the nanoscale. Nano-sized ferrite nanoparticles with spinel structure have been synthesized by co-precipitation method. We found that all investigated samples are polycrystalline with single phase in cubic system and the unit cell symmetries can be described by the space groups  $Fd-3m$ , confirming the reported yielding of the synthesis route used. The smallest crystallite size about 3 nm was obtained for as-dried sample while the largest value 71.86 nm was obtained from the highest studied temperature 1400°C. The crystallite size of the nano particles abruptly increased with the annealing temperature. The width of the peaks gave the average crystallite size of nanoparticles using Scherrer formula. From this result it can be mention that magnesium ferrite nano particles are sensitive to the temperature of formation.

Magnetic measurement showed that as dried sample have superparamagnetic properties at room temperature and it have shown ferromagnetic nature at 5K. The maximum magnetization of  $MgFe_2O_4$  nanoparticles was strongly size dependent and varied from 5emu/gm to 27emu/gm when crystallite size was increased from 3 nm to 71 nm, respectively. This value is lower than bulk  $MgFe_2O_4$ . This high surface to volume ratio of nanoparticles causes the saturation magnetization to be lower than that of bulk material. The coercive field of 24Oe to 48Oe was also measured in this crystallite size range. The coercivity of the nanoparticles was also studied as a function of particle size. Coercivity of the samples in nano level is almost zero, which is suggestive of superparamagnetic behavior at room temperature. For small size nano particles the coercivity increase rapidly and attains a maximum value of 88.9Oe at 52.57 nm (1000°C) and then decreases with further increase of particle size. The magnetic properties were also studied by Mössbauer spectroscopy. From the Mössbauer spectra the transition of magnesium ferrite from superparamagnetic state to ferromagnetic state was observed. The central doublet patterns were observed up to annealing temperature 800°C (16.93) confirming the superparamagnetic nature of nanoparticles. At 1000°C (52.57 nm), the formation of dominated sextets indicated the



nano particles material become ferromagnetic and is no longer appropriate for the application in magnetic particle hyperthermia. Mössbauer parameters such as isomer shift, quadruple splitting, hyperfine field and cation distributions at tetrahedral (A) and octahedral (B) sites were also determined. It was observed that Fe site population is not uniform at both sites.  $T_2$ relaxivity was determined from NMR spectroscopy. We have used coated Chitosan and PEG Magnesium ferrites to investigate the evolution of its values. It showed relaxivity values are different for different coating material and also depend on saturation magnetization, particle size and shape. The possibility of obtaining good MR image was also explored by using water phantoms. This image demonstrates that it is suitable material for MRI contrast agent.

## **5.2 Suggestions for future work**

Nanoscale magnetic materials are of interest for applications in ferrofluids, high-density magnetic storage, high-frequency electronics, high performance permanent magnets, and magnetic refrigerants. Magnetic single-domain nanoparticles ("super spins) are very interesting not only for potential applications, e.g. high density storage devices, but also for fundamental research in magnetism. In biotechnology, magnetic nanoparticles have been proposed for thermal treatment of tumor using nano shells and alternating magnetic fields to generate heat in localized points. Synthesized magnesium ferrite nanoparticles coated with Chitosan and PEG, their magnetic induction properties should be studied at varying concentration. For complete evaluation of whether magnesium ferrite nanoparticles can be used in magnetic particle hyperthermia for cancer treatment both in vivo and in vitro studies should be carried out using cancer cells and rats. Despite the advantages of hyperthermia as a cancer therapy much research is still needed to overcome the technical problems associated with this therapy. Furthermore, combination of hyperthermia with available chemotherapeutic agents or with novel candidates from natural source might open new dimensions in targeting resistant cancer. Magnetic properties including zero field measurement, temperature variable hall effect, dielectric measurement should be developed in order to obtain a more reliable result of its performance in materials science and electronic application. Moreover, different compositions, sample forming techniques and sintering conditions should be further investigated in order to optimize all properties.

## REFERENCE

## REFERENCE

### CHPATER-I

- [1.1] Safarik I., Safarikova M.; "Magnetic Nanoparticles and Biosciences", Monotshefte Fur Chemie, Frankfurt, 133, 737-759, 2002
- [1.2] Buzea C., Pacheco I., Robbie K.; Biointerphases, 2, MR17- MR71, 2007
- [1.3] Allhoff F., Lin p., Moore D.; What is Nanotechnology and why does it Matter? John Wiley and Sons, New York, pp. 3, 2010
- [1.4] Sohn B.H., Cohen R. E.; Chem. Mater. 9, 264-269, 1997
- [1.5] Klabunde K. J.; Nanoscale Materials in Chemistry, Wiley, pp.1, 2001
- [1.6] De M., Chosh P. S., Rotello V. M.; Adv. Mater. 20, 1, 2008
- [1.7] McCarthy J. R., Weissleder R.; Adv. Drug Del. Rev. 60 (11), 124, 2008
- [1.8] Y. Xia; Nat. Mater. 7, 758, 2008
- [1.9] Lee J. H, Huh Y. M., Jun J., Seo J., Jang J., Song H. T., Kim S., Cho E.J., Yoon H. G., Suh J. S., Cheon J.; Nat. Med. 13, 95, 2007
- [1.10] Anker J. N., Hall W. P., Lyandres O., Shah N. C., Zhao J., Van Duyne R. P.; Nat. Mater. 7, 442, 2008
- [1.11] Minchin R; Nat. Nanotech. 3, 12, 2008
- [1.12] Sanhai W. R., Sakamoto J. H., Canady R., Ferrari M.; Nat. Nanotech. 3, 242, 2008
- [1.13] Jiang W., Kim B. Y. S., Rutka J. T., Chan W. C. W.; Nat. Nanotech. 3, 145, 2008
- [1.14] A. Sandhu; Nat. Nanotech. 2, 758, 2007
- [1.15] Yager P., Edwards T., Fu E., Helton K., Nelson K., Tam R. M., Weigl H. B.; Nature 442, 412, 2006
- [1.16] Nam J. M., Stoeva S. I. & Mirkin C. A.; J. Am. Chem. Soc. 126, 5932, 2004
- [1.17] Klostranec J. M., Xiang Q., Farcas G. A., Lee J. A., Rhee A., Lafferty E. I., Perrault S. D., Kain K. C., Chan W. C.; Nano Lett. 9 (7), 28122007



- [1.18] Perez J. M., O'Loughlin L. J. T., Högemann D., Weissleder R.; *Nat Biotech.* 20, 816, 2008
- [1.19] Nielsen K., Smith P., Yu W.L., Elmgren C., Nicoletti P., Perez B., Bermudez R., Renteria T.; *Veterinary Microbiology* 124, 173, 2007
- [1.20] Rosi N. L., Mirkin C. A.; *Chem. Rev.* 105 (4), 1547, 2005
- [1.21] Perez J. M., Simeone F. J., Saeki Y., Josephson L., Weissleder R.; *J. Am. Chem. Soc.* 125 (34), 10192, 2003
- [1.22] Kaittanis C., Naser S. A., Perez J. M.; *Nano Letters* 7 (2), 380, 2007
- [1.23] Minchole A., Astalan A. P., Johansson C., Larsson K., Krozer A.; *Method and arrangement for analyzing substances*, PCT WO 03/019188 A1, 2003
- [1.24] Strömberg M., Göransson J., Gunnarsson K., Nilsson M., Svedlindh P., Strømme, M.; *Nano Lett.* 8 (3), 816, 2008
- [1.25] Pojarova M., Ananchenko G. S., Udachin K. A., Daroszewska M., Perret F., Coleman, A. W.; Ripmeester; J. A., *Chem. Mater.* 18, 5817, 2006
- [1.26] Chen J.-F., Ding H.-M., Wang J.-X., Shao L.; *Biomaterials* 25, 723, 2004
- [1.27] Cavallaro G., Maniscalco L., Licciardi M., Giammona G., *Macromol.; Biosci.* 4, 1028, 2004
- [1.28] Uhrich K. E., Cannizzaro S. M., Langer R. S., Shakesheff K. M.; *Chem. Rev.* 99, 3181, 1999
- [1.29] Allen T. M., Cullis P. R.; *Science* 303, 1818, 2004
- [1.30] Fahmy T. M., Fong P. M., Goyal A., Saltzman W. M.; *Nanotoday* 8, 18, 2005
- [1.31] Jo Y. S., Kim M.-C., Kim D. K., Kim C.-J., Jeong Y.-K., Kim K.-J., Muhammed M.; *Nanotechnology* 15, 1186, 2005
- [1.32] Hong R., Han G., Fernandez J. M., Kim B. J., Forbes N. S., Rotello V.M.; *J. Am. Chem. Soc.* 128, 1078, 2006
- [1.33] Giri S., Trewyn B. G., Stellmaker M. P., Lin V. S. Y., *Angew.; Chem. Int. Ed.* 44, 5038, 2005

- [1.34] Sawant R. M., Hurley J. P., Salmaso S., Kale A., Tolcheva E., Levchenko T. S., Torchilin V. P.; *Bioconjugate Chem.* 17, 943, 2006
- [1.35] Polizzi M. A., Stasko N. A., Schoenfisch M. H.; *Langmuir* 23, 4938, 2007
- [1.36] Vihola H., Laukkanen A., Valtola L., Tenhu H., Hirvonen J.; *Biomaterials* 26, 3055, 2005
- [1.37] Schmidt M. A.; *Colloid; Polym. Sci.* 285, 953, 2007
- [1.38] Zhang Y., Guan Y., Zhou S.; *Biomacromolecules* 7, 3196, 2006
- [1.39] Zhao Y., Kang J., Tan T.; *Polymer* 47, 7702, 2006
- [1.40] Erhardt A., Sillaber I., Welt T., Müller M. B., Singewald N., Keck M. E.; *Neuro-psychopharmacology* 29, 2074, 2004
- [1.41] Liu T.-Y., Hu S.-H., Liu T.-Y., Liu D.-M., Chen S.-Y.; *Langmuir* 22, 5974, 2006
- [1.42] Frimpong R. A., Fraser S., Hilt J. Z.; *J. Biomed. Mater. Res.* 80A, 1, 2007
- [1.43] Gao D., Xu H., Philbert M. A., Kopelman R.; *Nano Lett. ASAP Article*; DOI:10.1021/nl8017274, 2008
- [1.44] Lee A. H., Huh Y. M., Jun Y. W., Seo J. W., Jang J. T., Song H. T., Kim S., Cho E. J., Yoon H. G., Suh J. S., Cheon; "Artificially engineered magnetic nanoparticles for ultra-sensitive molecular imaging", *J. Nat. Med.*, 13, 95-99, 2007
- [1.45] R. Weissleder; *Nat. Rev. Cancer* 2, 11, 2002
- [1.46] D. J. A. Margolis, J. M. Hoffman, R. J. Herfkens, R. B. Jeffrey, A. Quon, S. S. Gambhir; *Radiology* 245, 333, 2007
- [1.47] Sun C., Lee J. S. H., Zhang M.; *Adv. Drug Del. Rev.* 60, 1252, 2008
- [1.48] Jun Y., Lee J. H., Cheon J. *Angew.; Chem., Int. Ed.* 47, 5122, 2008
- [1.49] Z. P. Xu, N. D. Kurniawan, P. F. Bartlett, G. Q. Lu; *Chem. Eur. J.* 13, 2824, 2007
- [1.50] Corot C., Robert P., Idee J. M., Port M.; *Adv. Drug Del. Rev.* 58, 1471, 2006

- [1.51] Kim D. K., Mikhaylova M., Wang F. H., Kehr J., Bjelke B., Zhang Y. T., sakalacos T., Muhammed M.; *Chem. Mater.* 15, 4343, 2003
- [1.52] Koo Y. E., Reddy G. R., Bhojani M., Schneider R., Philbert M. A., Rehemtulla A., Ross B. D., Kopelman R.; *Adv. Drug Del. Rev.* 58, 1556, 2006
- [1.53] Sun C., Veiseh O., Gunn J., Fang C., Hansen S., Lee D., Sze R., Ellenborge R. G., Olson J., Zhang M.; *Small* 4, 372, 2008
- [1.54] Weissleder R.; *Science* 312, 1168, 2006
- [1.55] Boutry S., Laurent S., Vander Elst L., Muller R. N.; *Contrast Med. Mol. Imaging* 1 (1), 15, 2006
- [1.56] Arbab A. S., Yocum, G. T., Kalish H., Jordan E. K., Anderson S. A., Khakoo A., Read E. J., Frank J. A.; *Blood* 104 (4), 1217, 2004
- [1.57] Sosnovik D. E., Weissleder R.; *Current Opinion in Biotechnology*, 18, 4, 2007
- [1.58] Byrappa K., Ohara S., Adschiri T.; *Adv. Drug Del. Rev.* 60, 299, 2008
- [1.59] Mornet S., Vasseur S., Grasset F., Duguet E.; *J. Mater. Chem.* 14, 2161, 2004
- [1.60] Rosensweig R. E.; *J. Magn. Magn. Mater.* 252, 370, 2002
- [1.61] Wust P., Gneveckow U., Johannsen M., Bohmer D., Henkel T., Kahmann F., Sehoulis J., Felix R., Ricke J. Jordan A.; *Int. J. Hyperthermia* 22, 673, 2006
- [1.62] Dobson J.; *Nat. Nanotech.* 3, 139, 2008
- [1.63] Herdt A. R., Kim B., Taton T. A.; *Bioconjugate Chem.* 18 (1), 183, 2007
- [1.64] Bornscheuer U. T., *Angew. Chem., Int. Ed.* 42, 3336, 2003
- [1.65] You C.-C., Verma A., and Rotello V. M., *Soft Matter* 2, 190, 2006
- [1.66] Safarik I., Safarikova M.; *Biomagn. Res. Technol.* 2 (1), 7, 2004
- [1.67] Xu C., Xu K., Gu H., Zheng R., Liu H., Zhang X., Guo Z., Xu B.; *J. Am. Chem. Soc.* 126, 9938, 2004
- [1.68] Pankhurst Q. A., Connolly J., Jones S. K., Dobson J.; *J. Phys. D* 36, R167, 2003



- [1.69] Hughes S., Mc Bain S., Dobson J., El Haj A. J. J. R.; Soc. Interface 5, 855, 2008
- [1.70] Sura H. S., Magnay J., Dobson J. & El Haj A. J.; Tissue Eng. 13, 1699, 2007
- [1.71] N. W. Turner, C. W. Jeans, K. R. Brain, C. J. Allender, V. Hlady, D. W. Britt; Biotechnol. Prog. 22, 1474, 2006
- [1.72] Liang Y. Y., Zhang L. M., Jian W., Li W.; Chem. Phys. Chem. 8, 2367, 2007
- [1.73] Dobson J.; Gene Therapy 13, 283, 2006
- [1.74] Lin Y.-S., Wu S.-H., Hung Y., Chou Y.-H., Chang C., Lin M.-L., Tsai C.-P., Ou C.-Y.; Chem. Mater. 18, 5170, 2006
- [1.75] Choi J. H., Nguyen F. T., Barone P. W., Heller D. A., Moll A. E., Patel D., Strano M. S.; Nano Lett. 7, 861, 2007
- [1.76] Gratton S. E. A., Ropp A. P., Pohlhaus P. D., Luft J. C., Madden V. J., Napier M. E., De Simone J.; M. PNAS 105 (33), 11613, 2008
- [1.77] Seshan K., Shashimohan A.L., Chakrabarty D. K., Biswas A. B.; Phys. Status Solidi A, 68, 97-101, 1981
- [1.78] Bahout M. M., Bertrand S., Pena O.; J. Solid State Chem. 178, 1080-1086, 2005
- [1.79] Shimizu Y., Arai H., Seiyama T., Sens; Actuators, 7, 11-22, 1985
- [1.80] Chen N.S., Yang X.J., Liu E.S., Huang J. L., Sens; Actuators B, 66, 178-180, 2000
- [1.81] Konishi K., Maehara T., Kamimori T., Aono H., Naohara T., Kikkawa H., Watanabe Y., Kawachi K.; J. Magn. Mater. 272-276, 2428-2429, 2004
- [1.82] Huang, Y., Tang, Y., Wang, J., Chen, Q.; Mater. Chem. Phys. 97, 394-397, 2006
- [1.83] Haart L.G.J., Blasse G.; Solid State Ionics, 16, 137-139, 1985

- [1.84] Astorino E., Busca G., Ramis G., Willey R.J.; *Catal. Lett.* 23, 353-360, 1994
- [1.85] Coquay P., Peigney A., De Grave E., Vandenberghe R. E., Laurent C.; *J. Phys. Chem. B*, 106, 13199-13210, 2006
- [1.86] Busca G., Finocchio E., Lorenzelli V., Trombetta M., Rossini S.A.; *J. Chem. Soc. Faraday Trans.* 92, 4687-4693, 1996
- [1.87] Sheongi S.W., Mostovoy M.; *Nat. Mater.* 6, 13-20, 2007
- [1.88] Singh A., Pandey V., Kotnala R. K., Pandey D.; *Phys. Rev. Lett.* 101, 24, 7602, 2008
- [1.89] Bahadur D.; *Bull. Mater. Sci.* 15, 431-439, 1992
- [1.90] Chen C.; *Magnetism and Metallurgy of Soft Magnetic Materials*, Dover Publications, New York, pp. 26, 1986
- [1.91] Kong L. B., Li Z. W., Lin G.Q., Gan Y. B.; *J. Am. Ceram. Soc.* 90, 2104-2112, 2007
- [1.92] Oliver S. A., Willey R. J., Hamdeh H. H., Oliveri G., Busca G.; *Scr. Metall. Mater.* 33, 1695-170, 1995
- [1.93] Zimmol M., Graff A., Sieber H., Senz S., Schmidt S., Mattheis R., Hesse D. *Solid State Ionics*, 101-103, 667-672, 1997
- [1.94] Chen Q., Rondinone A. J., Chakoumakos B. C., Zhang Z. J.; *J. Magn. Magn. Mater.* 194, 1-7, 1997
- [1.95] Liu C., Zou B., Rondinone A. J., Zhang Z. J.; *J. Am. Chem. Soc.* 122, 6263-6267, 2007
- [1.96] Sepelak V., Schultze D., Krumeich F., Steinike U., Becker K. D.; *Solid State Ionics*, 141, 677-682, 2001
- [1.97] Sepelak V., Baabe D., Mienert D., Litterst F. J., Becke K. D.; *Scr. Mater.* 48, 961-966, 2003
- [1.98] Rabanal M. E., Várez A., Levenfeld B., Torralba J. M.; *J. Mater. Process. Technol.* 143-144, 470-474, 2003

- [1.99] Chhaya S. D., Pandya M.P., Chhantbar M. C., Modi K. B., Baldha G. J., Jo H. H.; *J. Alloys Compd.* 377, 155-161, 2004
- [1.100] Turkin A. I., Drebuschak V. A.; *J. Cryst. Growth*, 265, 165-167, 2004
- [1.101] Verma S., Joy P. A., Kholam Y. B., Potdar H. S., Deshpande S. B.; *Mater. Lett.* 58, 1092-1095, 2005
- [1.102] Liu Y., Liu Z., Yang Y., Yang H., Shen G., Yu R.; *Sens. Actuators, B* 107, 600-604, 2005
- [1.103] Bergmann I., Šepelák V., Becker K. D.; *Solid State Ionics*, 177, 1865-1868, 2006
- [1.104] Šepelák V., Bergmann I., Menzel D., Feldhoff A., Heitjan P., Litterst F.J., Becker K. D.; *J. Magn. Magn. Mater.* 316, e764-e767, 2007
- [1.105] Ichiyangi Y., Kubota M., Moritake S., Kanazawa Y., Yamada T., Uehashi T.; *J. Magn. Magn. Mater.* 310, 2378-2380, 2007
- [1.106] Deng H., Chen H., Li H.; *Mater. Chem. Phys.* 101, 509-513, 2007
- [1.107] Shah J., Kotnala R.K., Singh B., Kishan H.; *Sens. Actuators, B* 128, 306-311, 2007
- [1.108] Pradeep A., Priyadharsini P., Chandrasekaran G.; *J. Magn. Magn. Mater.* 320, 2774-2779, 2008
- [1.109] Sasaki T., Ohara S., Naka T., Vejpravova J., Sechovsky V., Umetsu M., Takami S., Jeyadevan B., Adschiri T. J.; *Supercrit. Fluids*, 53, 92-94, 2010
- [1.110] Ahmed Y. M. Z., Ewais E. M. M., Zaki Z. I.; *J. Alloys Compod.* 489, 269-274, 2010
- [1.111] Burianova S., Poltiero-vejpravova J., Holec P., Plocek J.; *J. Phys. Conf. Ser.* 200, 072015, 2010
- [1.112] Bharti D.C., Mukherjee K., Majumder S. B.; *Mater. Chem. Phys.* 120, 509-517, 2010
- [1.113] Dalt S. D., Takimi A. S., Volkmer T. M., Sousa V. C., Bergmann C. P. *Powder Technol.* 210, 103-108, 2011



- [1.114] Patil J. Y., Khandekar M.S., Mulla I. S., Suryavanshi S. S., *Curr. Appl. Phys.* 12, 319-324, 2012
- [1.115] Vestal C. R., Zhang J. Z.; *Int. J. Nanotechnol.* 1, 240-263, 2004
- [1.116] Seip C. T., Carpenter E. E., O'Connor C. J., John V. T., Li, S.; *IEEE Trans. Magn.* 34, 1111-1113, 1998

## CHAPTER-II

- [2.1] Lewis and Clark College; Scientists prove how geckos stick, unlock secrets to making artificial gecko glue, 2002
- [2.2] Lu A.-H., Salabas E. L., Schüth F. *Angew. Chem. Int. Ed.* 46 (8), 1222, 2007
- [2.3] Laurent S., Forge D., Port M., Roch A. Robic C., Elst L. V., Muller R. N.; *Chem. Rev.* 108, 2064, 2008
- [2.4] Bean C. P., Livingston J. D.; *J. Appl. Phys.* 30, 120S, 1959
- [2.5] Prieto-Astalan, A. *Brownian; Relaxation Measurements of Magnetic Nanoparticles: Towards the Development of a Novel Biosensor System – Licentiate thesis, Chalmers University of Technology, Göteborg, 2007*
- [2.6] Johansson, C.; *Magnetic studies of magnetic liquids – Doctoral thesis, Chalmers University of Technology and University of Göteborg, 1993*
- [2.7] Fannin P. C., Scaife B. K. P., Charles S. W. *J. Magn. Mater.* 1987, 65, 279
- [2.8] Rosensweig R. E.; *J. Magn. Mater.* 252, 370, 2002
- [2.9] B. M. Moskowitz; *Hitchhiker's guide to magnetism, University of Minnesota, Institute of Rock Magnetism, 1991*
- [2.10] Pankhurst Q. A.; Connolly J., Jones S. K.; Dobson J.; 'Applications of magnetic nano particles in biomedicine'. *J. Phys. D: Appl. Phys.* 36, (13), R167, 2003
- [2.11] Madras G.; McCoy B. J.; *J. Chem. Phys.* 117(17), 8042, 2002
- [2.12] Sugimoto T.; *Adv. Colloid Interface Sci.* 28, 65, 1987

- [2.13] Beattie J. K.; *Pure & Appl. Chem.* 61(5), 937, 1989
- [2.14] Boistelle R., Astier J. P.; *J. Cryst. Growth* 90, 14, 1988
- [2.15] Dirksen J. A., Ring T. A.; *Chem. Eng. Science* 46 (10), 2389, 1991
- [2.16] Privman V., Goia D. V., Park J., Matijević E.; *J. Colloid Interface Sci.* 213, 36, 1999
- [2.17] Penn R. L., Oskam G., Strathmann T. J., Searson P. C., Stone A. T., Veblen D. R.; *J. Phys. Chem. B*, 105(11), 2177, 2001
- [2.18] Ocaña M., Morales M. P., Serna C.J.; *J. Colloid Interface Sci.* 17, 1995
- [2.19] Zheng Y., Cheng Y., Wang Y., Bao F.; *J. Cryst. Growth*, 284, 221, 2005
- [2.20] Banfield J. F., Welch S. A., Zhang H., Thompsen Ebert T., Penn R. L.; *Science* 289, 751, 2000
- [2.21] Niederberger M., Krumeich F., Hegetschweiler K., Nesper R.; *Chem. Mater.* 14 (1), 78, 2002
- [2.22] Penn R. L.; *J. Phys. Chem. B* 108(34), 12707, 2004
- [2.23] Penn R. L., Banfield, J. F.; *Science* 281, 969, 1998
- [2.24] Gilbert B., Zhang H., Huang F., Finnegan M. P., Waychunas G. A., Banfield J. F. *Goechem; Trans.* 4(4), 20, 2003
- [2.25] Barker A. J., Cage B., Russek S., Stoldt C. R., *J. Appl. Phys.*, 98, 063528, 2005
- [2.26] Chinnasamy C. N., Narayanasamy A., Ponpandian N., Chattopadhyay K., Shinoda K., Jeyadevan B., Nakatsuka K., Furubayashi T., Nakatani I.; *Phys. Rev. B* 63, 184108, 2001
- [2.27] Mahmoud M. H., Hamdeh H. H., Ho J. C., O'Shea M.J., Walker J. C.; *J. Magn. Magn. Mater.* 220, 139, 2000
- [2.28] Li F. S., Wang L., Wang J. B., Zhou Q. G., Zhou X. Z., Kunkel H. P., Williamsb G.; *J. Magn. Magn. Mater.* 268, 332, 2004
- [2.29] Mandrus D., Keppens V., Chakoumakos B. C.; *Mater. Res. Bull.* 34(7), 1013, 1999
- [2.30] Goya G. F., Rechenberg H. R., Jiang J. Z.; *J. Appl. Phys.* 84(2), 1101, 1998

- [2.31] Shi Y., Ding J., Liu X., Wang J.; *J. Magn. Magn. Mater.* 205, 249, 1999
- [2.32] Shinde S. R., Kulkarni S. D., Banpurkar A. G., Nawathey-Dixit R., Date S. K., Ogale, S. B.; *J. Appl. Phys.* 88(3), 1566, 2000
- [2.33] Son S., Taheri M., Carpenter E., Harris V. G. McHenry M. E.; *J. Appl. Phys.* 91(10), 7589, 2002
- [2.34] Veintemillas-Verdaguer S., Morales M. P. Serna C. J.; *Mater. Lett.* 35, 227, 1998
- [2.35] Wang S., Xin H., Qian Y.; *Mater. Lett.* 33, 113, 1997
- [2.36] Yamaguchi K., Matsumoto K., Fujii T.; *J. Appl. Phys.* 67, 4493, 1990
- [2.37] Lawaezeck R., Menzel M., Pietsch H., *Appl. Organomet.; Chem.* 18, 506, 2004
- [2.38] Mc Michael R. D., Shull R. D., Swartzendruber L. J., Bennett L. H., Walson R. E.; *J. Magn. Magn. Mater.* 111, 29, 1992
- [2.39] Kang Y. S., Risbud S., Rabolt J. F., Stroeve, P.; *Chem. Mater.* 8(9), 2209, 1996
- [2.40] Raj K., Moskovitz B., Casciari R.; *J. Magn. Magn. Mater.* 149, 174, 1995
- [2.41] Robinson D. B., Persson H. H. J., Zeng H., Li G., Pourmand N., Sun S., Wang S. X.; *Langmuir* 21, 3096, 2005
- [2.42] Grancharov S. G, Zeng H., Sun S., Wang S. X., O'Brien S., Murray C. B., Kirtley J. R.; *J. Phys. Chem. B* 109, 13030, 2005
- [2.43] Gee S. H., Hong Y. K., Erickson D.W., Park M. H., Sur J. C.; *J. Appl. Phys.* 93(10), 7560, 2003
- [2.44] Grasset F., Labhsetwar N., Li D., Park D. C., Saito, N., Haneda H., Cador, O., Roisnel, T., Mornet, S., Duguet, E., Portier, J., Etourneau; *J. Langmuir* 18(21), 8209, 2002
- [2.45] Sousa, M. H., Tourinho, F. A., Depeyrot, J., José da Silva, G., Lara, M. C. F. L.; *J. Phys. Chem. B*, 105(6), 1168, 2001



- [2.46] Ryu B.-H., Chang H.-J., Choi Y.-M., Kong K.-J., Lee J.-O., Kim C.-G., Jung H.-K., Byun J.-H.; *Phys. Stat. Sol.* 201(8), 1855, 2004
- [2.47] Hsu W.-C., Chen S. C., Kuo P. C., Lie C. T., Tsai W. S.; *Mat. Sci. Eng. B*, 111, 142, 2004
- [2.48] Tada M., Hatanaka S., Sanbonsugi H., Matsushita N., Abe M.; *J. Appl. Phys.* 93(10), 7566, 2003
- [2.49] Bruce I. J., Taylor J., Todd M., Davies M. J., Borioni E., Sangregorio C., Sen T.; *J. Magn. Magn. Mater.* 284, 145, 2004
- [2.50] Khoudiakov M., Gupta M. C., Deevi S.; *Nanotechnology* 15, 987, 2004
- [2.51] Chen J. P., Sorensen C. M., Klabunde K. J., Hadjipanayis G. C., Devlin, E. Kostikas A.; *Phys. Rev. B* 54(13), 9288, 1996
- [2.52] Kim W. C., Park S. I., Kim S. J., Lee S. W., Kim C. S.; *J. Appl. Phys.* 87(9), 6241, 2000
- [2.53] Kim W. C., Kim S. J., Sur J. C., Kim C. S.; *J. Magn. Magn. Mater.* 242-245, 197, 2002
- [2.54] Lee S. W., Ryu Y. G., Yang, K. J., Jung K.-D., An S. Y., Kim C. S.; *J. Appl. Phys.* 91(10), 7610, 2002
- [2.55] Del Castillo J., Rodríguez V. D., Yanes A. C., Méndez-Ramos J., Torres M. E.; *Nanotechnology* 16, S300, 2005
- [2.56] Hu Q., Zhao J., Wang Zhao J., Wang Y., Zhu L., Li M., Li G., Wang Y., Ge F.; *J. Molec. Catalysis A: Chem.* 200, 271, 2003
- [2.57] Hench L. L., West J. K.; *Chem. Rev.* 90(1), 33, 1990
- [2.58] Brinker C. J., Scherer G. W.; *Sol-Gel Science: The Physics and Chemistry of Sol-Gel Processing*; Academic Press, Inc.: San Diego, p. 112, 1990
- [2.59] Cansell F., Chevalier B., Demourgues A., Etourneau J., Even C., Garrabos Y., Pessey V., Petit S., Tressaud A., Well F.; *J. Mater. Chem.* 9, 67, 1999
- [2.60] Li J., Chen Z., Wang R.-J., Proserpio, D. M. *Coord.; Chem. Rev.* 190-192, 707, 1999

- [2.61] Sun Y.-P; Supercritical Fluid Technology in Materials Science and Engineering; Marcel Dekker, Inc.: New York, p. 335, 2002
- [2.62] Carpenter E. E., O' Connor C.J., Harris V.G.; J. Appl. Phys. 85(8), 5175, 1999
- [2.63] Liu C., Zou B., Rondinone A. J., Zhang Z. J.; J. Phys. Chem. B, 104(6), 1141, 2000
- [2.64] Feltin N., Pileni M. P.; Langmuir 13(15), 3927, 1997
- [2.65] Poddar P., Srikanth H., Morrison S. A., Carpenter E. E.; J. Magn. Magn. Mater. 288, 443, 2005
- [2.66] Košak A., Makovec D., Žnidaršič A., Drofenik M.; J. Eur. Ceram. Soc. 24, 959, 2004
- [2.67] Capek I.; Adv. Colloid Interface Sci. 110, 49, 2004
- [2.68] Lange R. F.; Surfactants: A Practical Handbook; Hanser-Gardner Publications: Cincinnati, p.1-5, 1999
- [2.69] Uskoković V., Drofenik M., Ban I.; J. Magn. Magn. Mater. 284, 294, 2004.
- [2.70] Vestal C. R., Zhang Z.; J. Chem. Mater. 14(9), 3817, 2002.
- [2.71] Lee Y., Lee J., Bae C. J., Park J.-G., Noh H.-J., Park J.-H., Hyeon T.; Adv. Funct. Mater. 15(3), 503, 2005
- [2.72] Chkoundali S., Ammar S., Jouini N., Fiévet F., Molinié P., Danot M., Villain F., Grenèche J.-M.; J. Phys.: Condens. Matter. 16, 4357, 2004
- [2.73] Ammar S., Helfen A., Jouini N., Fiévet F., Rosenman I., Villain F., Molinié P., Danot M.; J. Mater. Chem. 11, 186, 2001
- [2.74] Fiévet F., Lagier J. P., Blin B., Beaudoin B., Figlarz M.; Solid State Ionics 32/33, 198, 1989
- [2.75] Kurihara L. K., Chow G. M., Schoen P. E.; Nanostruct. Mater. 5(6), 607, 1995

- [2.76] Toneguzzo P., Viau G., Acher O., Fièvet-Vincent F., Fièvet F.; *Adv. Mater.* 10(13), 1032, 1998
- [2.77] Feldmann C., Jungk H.-O., *Angew; Chem. Int. Ed.* 40(2), 359, 2001
- [2.78] Park J., An K., Hwang Y., Park J.-G., Noh H.-J., Kim J.-Y., Park J.-H., Hwang N.-M., Hyeon T., *Nature Mater.* 3, 891, 2004
- [2.79] Yu W. W., Falkner J. C., Yavuz C. T., Colvin V. L.; *Chem. Com.* 2306, 2004
- [2.80] Sun S., Zeng H., Robinson D. B., Raoux S., Rice P. M., Wang S. X., Li G.; *J. Am. Chem. Soc.* 126(1), 273, 2004

### CHAPTER III

- [3.1] C. Kittel; "Introduction to Solid State Physics", 7<sup>th</sup> edition, John Wiley and Son, Inc., Singapur, 1996
- [3.2] J. B. Nelson, D. P. Riley; "An experimental investigation of extrapolation methods in the derivation of accurate unit-cell dimensions of crystals", *Proc. Phys. SOC. London* 57, 160, 1945
- [3.3] B. D. Cullity; "Elements of X-ray diffraction", reading, M. A; Addison Wesley, 1978
- [3.4] Simon Forner; "Versatile and sensitive Vibrating Sample Magnetometer", *Rev. Sci. Instr.* 30, p.548, 1959
- [3.5] Gunther K. Wertheim; "Mössbauer Effect: Principle and Application", Academic Press, New York, 1964
- [3.6] U. Gonser;; Ed., *Topics in Applied Physics*, Springer-Verlag, Berlin Heidelberg, New York, 1973
- [3.7] O. C. Kistner and A. W. Sunyar; *Phys. Rev. Letters* 4, 229, 1960
- [3.8] L. May; "An Introduction to Mössbauer Spectroscopy", Plenum Pres., New York, 1971
- [3.9] M. H. Cohen and F. Reift; *Solid State Physics*, 5. 321, 1957
- [3.10] R. M. Sternheimer; *Phys. Rev.*, 84, 244, 1951
- [3.11] G. K. Wertheim; "Mössbauer effect: Principles and Application", Academic Press, New York, 1964
- [3.12] Anjali Krishna Morthy; "Mössbauer Study of Electric field Gradients in Natural Mica and Synthetic Spinel System", Ph.D. Thesis, University of Rajsthan, Jaipur, 1980
- [3.13] E. Fermi; *Z. Physics*, 60, 320, 1930
- [3.14] R. A. Ferrel; *AJ.* 28, 484, 1960



#### CHAPETR-IV

- [4.1] J. Chandradass, Arvind H. Jadhav, Ki Hyeon Kim, Hern Kim; *J. Alloys Compd.* 512, 164-169, 2012
- [4.2] S. Da. Dalt, A. S. Takimi, T. M. Volkmer, V. C. Sousa, C. P. Bergmann; *Powder Technol.* 210, 103-108, 2011
- [4.3] S. K. Pradhan, S. Bid, M. Gateshki, V. Petkov; *Mater. Chem. Phys.* 93, 224-230, 2005
- [4.4] I. Bergmann, V. Sepelak, K. D. Becker; *Solid State Ionics*, 177, 1865-1968, 2006
- [4.5] L. D. Tung, V. Kolesnichenko, D. Caruntu, N. H. Chou, C. T. O Connor, L. Spinu; *J. Appl. Phys.* 93, 7486-7488, 2003
- [4.6] O. Iglesias, A. Labarta, X. Batlle; *J. Nanosci. Nanotechnol.* 8, 2761, 2008
- [4.7] V. Sepelak, D. Babbe, D. Mienert, F. J. Litterst, K. D. Becker; *Scr. Mater.* 48, 961-966, 2003
- [4.8] M. Zheng, X. C. Wu, B. S. Zou, Y. J. Wang; *J. Magn. Magn. Mater.* 183, 152, 1998
- [4.9] A. Pradeep, P. Priyadharsini, G. Chandrasekaran; *J. Magn. Magn. Mater.* 320, 2774-2779, 2008
- [4.10] Z. Mosleh, P. Kameli, M. Ranjbar, H. Salamati; *Ceramics International*, 40, 7279-7284, 2014
- [4.11] Kinnariparekh; *Indian J. of Pure Appl. Phys.* 48, 581-585, 2010
- [4.12] McC Arthy J. R, Weissleder R.; *Adv. Drug Deliv. Rev.* 60, 1241, 2008
- [4.13] Zhang Z, Mascheri N, Dharmakumar R, Fan Z, Paunesku T, Woloschak G, Li D.; *Cytotherapy* 11, 43, 2009
- [4.14] S. Manjura Hoque, C. Srivastava, N. Venkatesha and K. Chattopadhyay; *IEEE Trans. Nanobioscience*, 12, 4, 2013
- [4.15] S. Hong, Y. Chang and I. Rhee; *J. Korean Phys. Soc.*, 56, 868-873, 2010
- [4.16] S. A Agnihotri, N. N Mallikarjuna and T. M. Aminabhavi; *Journal of Controlled Release*, 100, 5-28, 2004

- [4.17] S. Manjura Hoque, C. Srivastava, N. Srivastava, N. Venkateshan and K. Chattopadhyay; J. of Mater. Sci. 48, 812-818, 2013

### CONFERENCE PUBLICATIONS

1. S. M. Hoque, N. Debnath, S. S. Sikder, H. N. Das, D. K. Saha, P. Norblad and S. Akhter; "Superparamagnetic /Ferromagnetic Transition of  $\text{NiFe}_2\text{O}_4$  Nanoensembles with the Increase of Grain Size", International Conference on Physics for Energy, Atomic Energy Centre, Dhaka, 06-08 March, 2014.
2. N. Debnath, S. M. Hoque, S. S. Sikder, D. K. Saha, and S. Akhter; "Synthesis and Characterization of  $\text{MgFe}_2\text{O}_4$  Ferrite Nanoensembles and their Potential Biomedical Applications", National Conference on Physics Research and Education in Bangladesh", Atomic Energy Centre, Dhaka, 24 – 25 April, 2015.